REPRESENTING DROPLET SIZE DISTRIBUTION AND CLOUD PROCESSES IN AEROSOL-CLOUD-CLIMATE INTERACTION STUDIES

A Thesis
Presented to
The Academic Faculty

by

Wei-Chun Hsieh

In Partial Fulfillment
of the Requirements for the Degree
Doctor of Philosophy in the
School of Earth and Atmospheric Sciences

Georgia Institute of Technology
August 2009

REPRESENTING DROPLET SIZE DISTRIBUTION AND CLOUD PROCESSES IN AEROSOL-CLOUD-CLIMATE INTERACTION STUDIES

Approved by:

Dr. Athanasios Nenes,
Committee Chair
School of Earth and Atmospheric Sciences
Georgia Institute of Technology

Dr. Athanasios Nenes, Advisor
School of Earth and Atmospheric Sciences
Georgia Institute of Technology

Dr. Michael Bergin
School of Civil and Environmental Engineering
Georgia Institute of Technology

Dr. Judith A. Curry
School of Earth and Atmospheric Sciences
Georgia Institute of Technology

Dr. Irina Sokolik
School of Earth and Atmospheric Sciences
Georgia Institute of Technology

Dr. Andrew Stack
School of Earth and Atmospheric Sciences
Georgia Institute of Technology

Dr. Rodney Weber
School of Earth and Atmospheric Sciences
Georgia Institute of Technology

Date Approved: April 29 2009

To my mother and sister

ACKNOWLEDGEMENTS

I would like to thank my advisor, Dr. Athanasios Nenes, for the guidance and freedom he has provided me in the research and the direction he has given me toward becoming a good scientists. I also would like to thank him for the opportunities he has given me to attend and present at conferences over the past years. I would like to thank my family for their support and love. To my mother and sister who are always there to share my life and let me believe in myself. To my brother who has been given company to my mother. To my friends, who have gone though all the lows and highs with me- life has become a joyful journey with you. I am indebted to my research group for providing a stimulating and fun environment in which to learn and grow. I have had the fortune to be in this department: it has been a new, different, and eye-broadening life experience. Finally, I would like to thank Miss Victoria L. K. Van Cappellen for her help in improving this thesis and also thank many teachers, former advisor and several great scientists I have met at conferences, thank you for your advice and help. I cannot say it enough. Thank you.

TABLE OF CONTENTS

LIST OF TABLES

LIST OF FIGURES

SUMMARY

The indirect effect of aerosols expresses how changes in aerosols would influence clouds and cause impacts on Earth's climate and hydrological cycle. The current assessment of the interactions between aerosols and clouds is uncertain and parameterizations used to represent cloud processes are not well constrained. This thesis first evaluates a cloud activation parameterization by investigating cloud droplet number concentration closure for stratocumulus clouds sampled during the 2005 MArine Stratus Experiment (MASE). Further analysis of the droplet size distribution characteristics using the extended parameterization is performed by comparing the predicted droplet spectra with the observed ones. The effect of dynamical variability on the droplet size distribution evolution is also investigated by considering a probability density function for updraft velocity. The cumulus and stratocumulus cloud datasets from in-situ field measurements of NASA's Cirrus Regional Study of Tropical Anvils and Cirrus Layers - Florida Area Cirrus Experiment (CRYSTAL-FACE) and Coastal STRatocumulus Imposed Perturbation Experiment (CSTRIPE) campaigns are used for this task. Using the same datesets, the autoconversion rate is calculated based on direct integration of kinematic collection equation (KCE). Six autoconversion parameterizations are evaluated and the effect of turbulence on magnifying collection process is also considered. Finally, a general circulation model (GCM) is used for studying the effect of different autoconversion parameterizations on indirect forcing estimates. The autoconversion rate given by direct KCE integration is also included by implementing a look-up table for collection kernels. Although these studies add more variability to the current estimate of aerosol indirect forcing, they also provide direction towards a more accurate assessment for climate prediction.

CHAPTER I

INTRODUCTION

The estimate of aerosol indirect effects is the most uncertain component of climate change prediction [108, 37, 134, 69, 75]. Anthropogenic activities increase the concentration of aerosols, which could serve as cloud condensation nuclei (CCN); thus changing the level of CCN concentration could change in cloud properties. Assuming clouds hold the same liquid water content, the enhanced aerosol number would decrease the mean droplet size and cause cloud albedo change. This is known as the "first indirect aerosol effect" or the "cloud albedo effect." A change in the droplet size would further affect the development of cloud precipitation and may modify the lifetime of a cloud. This is known as the "second indirect aerosol effect" or the "cloud lifetime effect".

The metric used for estimating aerosol effects on climate is the calculated radiative forcing, measured in Wm^{-2}. The calculated radiative forcing commonly refers to the top of atmosphere (TOA) or bottom of atmosphere (BOA), that is, the Earth's surface. The radiative forcing for the cloud albedo effect is estimated to be in the range of -0.5 to -1.9 Wm^{-2} and -0.3 to -1.4 Wm^{-2} for the cloud lifetime effect [108].

General circulation models (GCMs) are the primary tools for estimating indirect effects on a global scale. The large uncertainty for aerosol-cloud interactions assessments results from cloud processes that take place in a relatively small domain in a typical GCM grid cell. Cloud parameterizations are formulas used to represent these subgrid systems and are expressed as parameters of large-scale states. Therefore, the uncertainty of estimating climate change may be due to the simplified form of the parameterizations. For example, the differences in the indirect effect estimates

among GCM simulations may be caused by the approach used for predicting the cloud droplet number, that is, an empirical or mechanistic relationship. Moreover, using the large-scale vertical velocity for small-scale cloud activation would also introduce unrealistic results as the magnitude of updraft for activation is much higher than the mean vertical velocity predicted in GCMs.

1.1 Effects of aerosols on clouds

The effects of aerosols on clouds are commonly investigated by analyzing the induced changes in cloud microphysical properties (droplet number concentration and size distributions) and macrophysical properties (liquid water path, cloud fraction, and cloud thickness) properties. It has been shown the release of particles leads to cloud droplet number concentration increases. As a result, the sizes of cloud droplets would decrease, which may slow down the collision-coalescence process and suppress the formation of precipitation. The evidence of pollution effects on clouds is clearly manifest in the appearance of ship tracks observed in satellite imagery. Ship tracks are characterized as bright, narrow lines of the regions affected by ship exhaust in marine stratocumulus clouds. The effluent from ships contains a high concentration of CCN particles, which is thought to be the reason for generating the ship's trails. Radke et al. [133] and Ferek et al. [57] reported that, as compared to surrounding clouds, ship tracks exhibit higher CDNC, smaller droplet sizes, and higher liquid water content. Study by Kaufman et al. [82] also showed the increased aerosols may be responsible for 40-100% of observed increases in cloud coverage based on remote sensing observations. However, the decrease in the cloud fraction of small, warm cumulus clouds which are associated with an increase in aerosols is also shown in remote sensing studies. These studies illustrate the complexity of aerosol-cloud interactions and accompanying processes such as dynamical and radiative feedbacks must be taken into accounted when studying the effects of aerosols.

1.2 Effects of aerosols on precipitation

The impact of pollution on precipitation is much less clear as compared to its impact on clouds, especially for clouds where ice processes are involved in precipitation formation. The studies by Borys et al. [26] and Borys et al. [25] show that the smaller cloud drops due to aerosol enhancement lead to less efficient riming and produce smaller ice crystals, smaller fall velocities and less snowfall. Their analysis also demonstrates that pollution can delay the onset of precipitation in winter orographic clouds in the Rocky Mountains. Numerical model simulations also point out the effects of aerosols on precipitation. For example, Teller and Levin [162] used a 2-D slab symmetric model, which included detailed cloud microphysics. Their results show that a decrease in the amount of rain on the ground was due to increases in CCN in Mediterranean-type winter convective clouds. Moreover, the effects of aerosols on precipitation for deep convection clouds may not be monotonic and a wide range of precipitation change has been reported. Figure 1 shows the change in precipitation caused by increasing aerosols for deep convective clouds and is a summary chart based on Table 5 of Tao et al. [160]. As the plot shows, the change of precipitation amount can be either negative or positive and varies in the range from -88% to 700%. The difference in model settings such as the resolution of grid cells, the implemented cloud schemes and the numerical techniques may contribute to the large discrepancy among simulations. One of difficulties in assessing aerosol-precipitation interactions is the fact that precipitation is also influenced by other factors such as vertical profiles of moisture and stability. Because clouds and precipitation are very sensitive to meteorological conditions, different meteorological parameters corresponding to different aerosol types must be considered when studying the aerosol effects on precipitation.

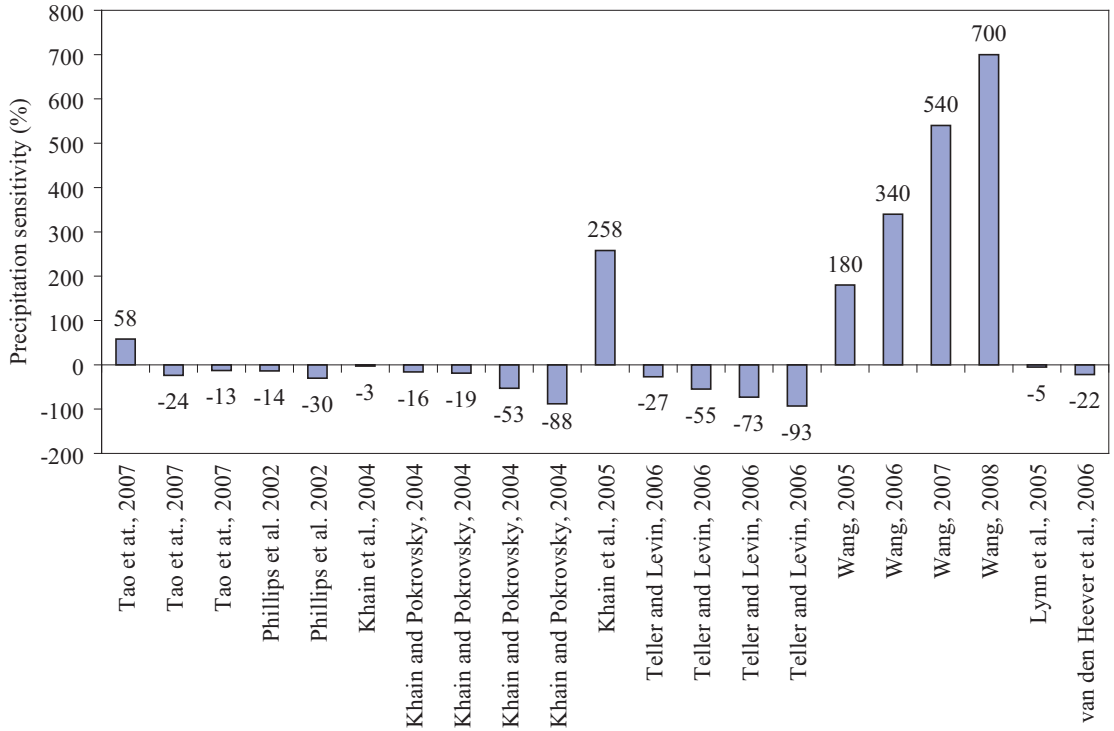

Figure 1: Sensitivity of precipitation to increases in CCN number for different studies, adapted from Table 5 of Tao et al. [160]. (and references contained therein)

1.3 Clouds and cloud types

About half of the Earth's surface is covered by clouds; clouds play a dominant role in the Earth's climate, The distributions of shortwave solar radiation and longwave radiation in the atmosphere are affected by clouds, which in turn affects the radiative balance. It is important to understand how clouds form, grow, and dissipate to provide accurate climate predictions. The heat generated in clouds energizes a wide range of motion ranging from global atmospheric circulation, tropical hurricanes, and mid-latitude cyclones, to individual meso-scale convection systems. Earth's hydrological cycle is also closely associated with clouds which transport moisture vertically and horizontally and change the spacial distributions of water.

The release of water in the atmosphere is achieved by precipitation, which develops in certain types of clouds with potential raining conditions. Based on the physical appearance of clouds, the three principal cloud types or shapes are cirrus, stratus, and cumulus. In this section, two main cloud types of cumulus and stratocumulus are introduced as those are analyzed in the following chapters.

There are two main processes which can generate stratocumulus clouds: 1) The mixing caused by turbulence transforms a fog or stratus layer into stratocumulus clouds. 2) In a warm ocean surface, heating of the lower atmosphere can initiate shallow convection. Because of turbulent motions, this would tend to generate a well-mixed atmospheric boundary layer where the potential temperature and water vapor mixing ratio are constant throughout the layer. The characteristic liquid water content for stratus and stratocumulus clouds ranges from 0.1 to 0.5 gm^{-3} [132]. The depth of stratocumulus clouds depends on 1) large-scale subsidence which tends to decrease the depth and 2) the entrainment at the top of cloud, which is usually associated with an increase in the mixed layer. Several factors may cause the decoupling of a stratocumulus-topped mixed layer such as the presence of drizzle, decreased surface buoyancy fluxes, heating from solar radiation, and entrainment of warm and dry air.

The stability of a stratocumulus cloud layer can be altered by the presence of drizzle which affects the vertical distribution of latent heating. The falling of drizzle starts from the top of cloud, which evaporation is not active in that layer. As a result, the net latent heat increases in the upper layer of cloud. In contrast to the regime below the cloud, where the evaporation of falling water is active, this would lead to a cooler subcloud layer. As a consequence of this process, two shallow unstable layers are formed that are decoupled by an intermediate stable layer.

The ascent of warm, buoyant air parcels is the main process generating cumuliform clouds. As compared to stratiform clouds, cumulus clouds are often associated with higher vertical velocities and intense precipitation. A large portion of the global ocean is covered by cumulus clouds, which are frequently observed in the tropics.

The structure and depth of cumuliform clouds are determined by heat and moisture fluxes from the surface, atmospheric stability, and the large-scale vertical velocity. A typical superadiabatic layer forms just above the surface with a depth of 30 - 100 m. This process generates thermal eddies caused by buoyancy. The thermodynamic profile within the atmospheric boundary layer is well mixed, which is characterized by a constant value of virtual potential temperature.

The development of cloud in general is determined by the vertical structure of the cloud and temperature above the cloud base. The surface instability induces buoyancy which raises the cloud parcel, if there is sufficient energy for the parcel to reach the level of free convection (LFC), then the cloud accelerates and grows vertically. After the cloud reaches the LFC, it continues to move upwards towards the level of neutral buoyancy (LNB), where the parcel acceleration is zero. Because of inertial from antecedent acceleration, the cloud parcel may penetrate above the LNB so that the top of cloud may appear at some distance above the level of neutral buoyancy.

Cirrus clouds appear in the form of fibrous shape and are characterized as thin,

wisplike strands. Homogeneous freezing of aqueous solution droplets is the dominant process in cirrus formation at temperatures below the supercooling limit of pure water droplets. Nucleation rate denotes the number of liquid-to-solid nucleation events per unit time per unit volume of liquid and is used to describe homogeneous ice nucleation. The values of nucleation rate vary by orders of magnitude, increasing from 10^{-8} $cm^{-3}s^{-1}$ at -30 ^oC to 10^{13} $cm^{-3}s^{-1}$ at -40 ^oC [131]. Heterogeneous ice nucleation refers to formation of ice with the presence of ice nuclei (IN). Ice formation process is largely more complicated than the formation of droplets. The water supersaturation is the primary factor to determine CCN activation property while the activity of IN depends on supersaturation and temperature. The main four processes for heterogeneous ice nucleation are (i) deposition nucleation, which water vapor directly deposit onto the surface of IN and transforms to ice. (ii) condensation-freezing nucleation, which a film of liquid is formed on the surface of IN, and then freezing of the condensate occurs. (iii) immersion-freezing nucleation, which the embedded IN within droplets would cause freezing of droplets. (iv) contact nucleation, which the drop freezing is induced by the contact of supercooled drops and IN.

Mixed-phase clouds are clouds consist of a mixture of ice particles and liquid droplets. Below 0 ^oC, cloud droplets may remain in a metastable liquid state down to about -40 ^oC. Because the water vapor saturation over ice and over land is different, the mixture of ice particles and liquid droplets is condensationally unstable. The study of [90] pointed out the high concentration of ice at lower levels in the stratiform clouds may be a result of the formation of ice particles through the freezing of liquid droplets. Several ice nucleation studies ([47, 71]) showed the freezing of liquid droplets is a dominant mechanism of ice generation, as compared to deposition nucleation and ice multiplication. There are two stages to form ice particles. First, activation of droplets occurs as a consequence of supersaturation of water vapor. Second, the freezing of liquid droplets occurs through mechanisms of immersion-freezing

nucleation or contact nucleation.

1.4 Basic physics of warm clouds

1.4.1 Equilibrium between two phases separated by a curved interface

Suppose the system is composed of a spherical bulk phase (denoted as superscript II in the corresponding symbol) of diameter D_p and another bulk phase I (superscript I). Each phase contains component k and a non-ideal mixture for the other components. The chemical potential, μ, for component k in either of the bulk phases can be expressed as [132]

$$\mu_k(p, T, a_k) = \mu_{k,0}(p, T) + RT \ln a_k \tag{1}$$

p is the system pressure, T is the common temperature and a_k is the activity for component k. Assuming thermal equilibrium, the chemical potential, $\mu_{k,0}(p, T)$ depends on p and T. Taking the total differential of Equation 1 and dividing this formula by T, the expression changes to

$$d\left(\frac{\mu_k}{T}\right) = -\frac{h_{k,0}}{T^2}dT + \frac{\upsilon_{k,0}}{T}dp + Rd\ln a_k \tag{2}$$

where

$$\left[\frac{\partial\left(\mu_k/T\right)}{\partial T}\right]_{p,n_{j\neq k}} = -\frac{h_k}{T^2} \tag{3}$$

$$\left[\frac{\partial\left(\mu_k/T\right)}{\partial p}\right]_{T,n_{j\neq k}} = \frac{\upsilon_k}{T} \tag{4}$$

The molar enthalpy is defined as $h = H/n$, where H is the enthalpy, n is the number of moles and h_k and υ_k are the partial molar enthalpy and volume of component k, respectively. Under equilibrium conditions, $\mu_k^I = \mu_k^{II}$, so that the differential form of equilibrium between phase I and II is written as

$$d\left(\frac{\mu_k^I}{T}\right) = d\left(\frac{\mu_k^{II}}{T}\right) \tag{5}$$

Thus combining Equation 5 with Equation 2, the following expression is obtained:

$$-\frac{(h_{k,0}^I - h_{k,0}^{II})}{T^2}dT + \frac{\upsilon_{k,0}^I}{T}dp^I - \frac{\upsilon_{k,0}^{II}}{T}dp^{II} + Rd\ln(a_k^I/a_k^{II}) = 0 \tag{6}$$

for the equilibrium of a curved interface, and known $h^I - h^{II} \equiv L^{II/I}$. Using the mechanism equilibrium; $p^{II} = p^I + 4\sigma/D_p$, the final form of Equation 6 is expressed as

$$-\frac{L_{k,0}^{II/I}}{T^2}dT + \frac{(\upsilon_{k,0}^I - \upsilon_{k,0}^{II})}{T}dp^I - \frac{4\upsilon_{k,0}^{II}}{T}d\left(\frac{\sigma}{D_p}\right) + Rd\ln(\frac{a_k^I}{a_k^{II}}) = 0 \tag{7}$$

where L is the latent heat of phase change per mole. Equation 7 describes the general equilibrium relationship between two phases with a curved interface and is the main equation for the following discussions.

1.4.2 Köhler equations

Köhler equations describe equilibrium between an aqueous solution drop and humid air. Considering a system composed of a drop of an aqueous salt solution (denoted as phase II) and an environment of humid air (phase I). It is assumed there is no vapor pressure from the dissolved substance and the mass of solutes remains constant during growth. The latter assumption generally holds for the early stages of cloud formation. In the later stages of growth, however, as a result of due to various scavenging processes, solutes may be added to the drop. The dependence of saturation vapor pressure, $p_w(D_p)$, on the diameter of the drop, D_p is determined from Equation 7, where only the last two terms are included. At constant T, n_s, and total air pressure p, with $a_k^I = a_v = p_w(D_p)/p$ and $a_k^{II} = a_w \neq 1$, the following equation based on Equation 7 is obtained:

$$-\frac{4\upsilon_{w,0}}{RT}d\left(\frac{\sigma_{s/a}}{D_p}\right) + d\ln p_w(D_p) - d\ln a_w = 0 \tag{8}$$

Integrating from D_p, $p_w(D_p)$, a_w to $D_p \to \infty$, $p_w(D_p) = p^o$, and $a_w = 1$, Equation 8 becomes

$$\ln\frac{p_w(D_p)}{p^o} = \ln a_w + \frac{4M_w\sigma_{s/a}}{RT\rho_w D_p} \tag{9}$$

which is equivalent to

$$\frac{p_w(D_p)}{p^o} = a_w \exp\left(\frac{4M_w\sigma_{s/a}}{RT\rho_w D_p}\right) \tag{10}$$

where a_w can be expressed by the following equation from Pruppacher and Klett [132]:

$$a_w = \exp\left(-\frac{\upsilon \Phi_s n_s M_w}{\left(\pi D_p^3/6\right)\rho_s - m_s}\right) \tag{11}$$

Therefore, combining Equation 11 with Equation 10 yields the Köhler equation:

$$\frac{p_w(D_p)}{p^o} = \exp\left(\frac{4M_w\sigma_{s/a}}{RT\rho_w D_p} - \frac{\upsilon \Phi_s n_s M_w}{\left(\pi D_p^3/6\right)\rho_s - m_s}\right) \tag{12}$$

For a sufficiently dilute solution where $m_s \ll m_w$, $\sigma_{s/a} \approx \sigma_w$, $\Phi_s \approx 1$ and $\rho_s \approx \rho_w$, Equation 12 can be simplified to the following form:

$$\frac{p_w(D_p)}{p^o} = \exp\left(\frac{A}{D_p} - \frac{B}{D_p^3}\right) \tag{13}$$

where $A = \frac{4M_w\sigma_w}{RT\rho_w}$, $B = \frac{6n_s M_w}{\pi\rho_w}$, σ_w is the surface tension of water, n_s is the solute moles, and D_p is the droplet diameter. The first term of equation 13 expresses the Kelvin effect which tends to increase the vapor pressure. The second term is the solute term, which tends to decrease vapor pressure. The summation of curvature term, A/D_p, and the term of solute effect, B/D_p^3, determines the vapor pressure of an aqueous solution drop. As the droplet size decreases, both effects increase; but rate of increase is faster for solute effect. The critical diameter of the droplet is derived by taking the differential of Equation 13:

$$D_{pc} = \left(\frac{3B}{A}\right)^{1/2} \tag{14}$$

with the corresponding critical saturation, S_c, being expressed as

$$S_c = \exp\left(\frac{4A^3}{27B}\right)^{1/2} \tag{15}$$

According to Köhler theory, droplet activation can occur when the critical supersaturation of a particle is less than the maximum supersaturation experienced by the particle during its pathway in the atmosphere. The critical supersaturation of a particle is the maximum point of Köhler curve (Figure 2). An example of Köhler curves shown in Figure 2, which displays the water vapor supersaturation of ammonia sulfate droplets for particles with dry diameter 0.03, 0.05, 0.1 μm, respectively.

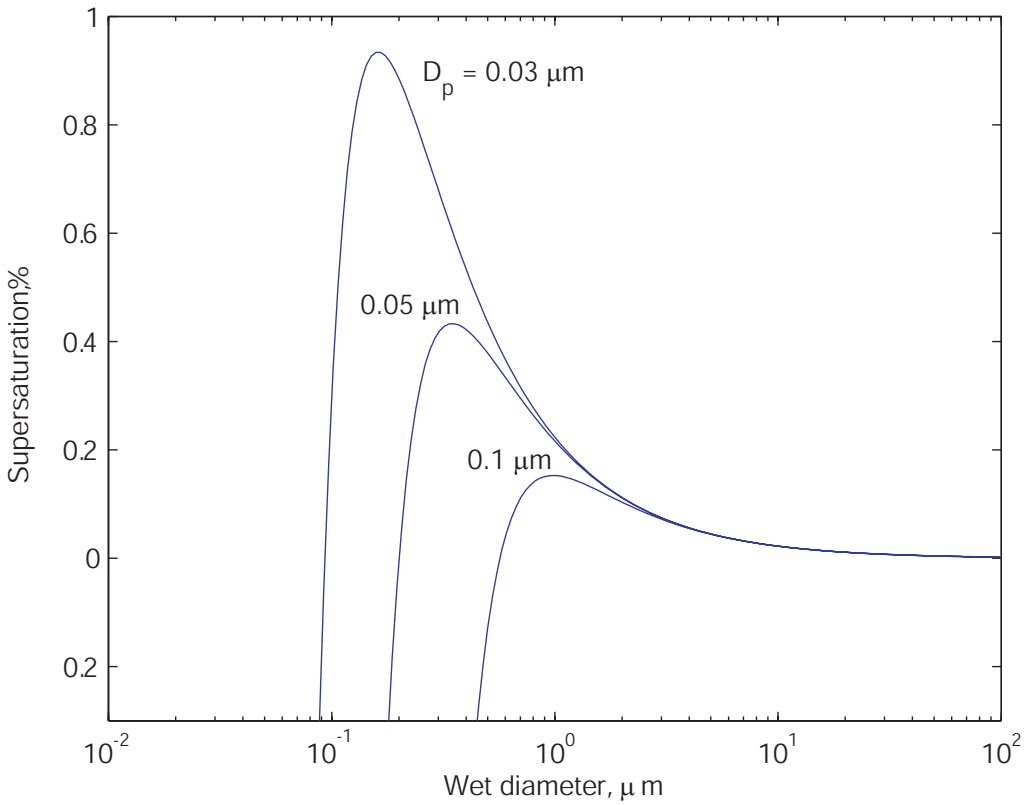

Figure 2: Köhler curves for ammonia sulfate particles with dry diameter 0.03, 0.05 and 0.5 μm at 293 K.

1.4.3 Cloud condensation nuclei

The ability of a particle to become activated depends on its size and chemical composition. Cloud condensation nuclei (CCN) are defined as aerosol particles that are capable of initializing cloud drop formation at low supersaturation. The number of CCN (N_{CCN}) depends on the type of air mass. Air masses over land have a higher N_{CCN} than maritime air masses. Also, the concentration of CCN increases with increasing supersaturation. The empirical relationship between N_{CCN} and supersaturation ($s_{v,w}^k$) can be expressed by the equation

$$N_{CCN} = Cs_{v,w}^k \tag{16}$$

where C and k are constants for a given air mass. By definition, C is the CCN concentration at a supersaturation of 1 %. The values of C and k vary to a large extent, depending on the type of airmass at a specific observation site. Seasonal changes in C and k are also reported by Hegg et al. [70], where larger C and k are generally observed in summer than in winter. The dependence of N_{CCN} on supersaturation is illustrated by a CCN spectrum, where CCN concentration is expressed as a function of supersaturation. It is expected that N_{CCN} increases with increasing supersaturation. Usually, the largest concentrations of CCN are found in air over cities and industrial complexes. The number of CCN can exceed 1000 cm^{-3} for air masses that have been over land for several days, but it is rarely larger than 100 cm^{-3} for marine air masses or modified maritime air that has been over land for less than two days.

1.4.4 κ-Köhler theory

Recently, Petters and Kreidenweis [128] proposed the κ-Köhler theory for describing the relationship between particle dry diameter and CCN activity using a single hygroscopicity parameter, κ. To contrast the traditional Köhler theory, a short summary of Petters and Kreidenweis' paper is provided in this section. The equation defining

κ-Köhler theory is expressed as

$$S(D_p) = \frac{D_p^3 - D_d^3}{D_p^3 - D_d^3(1-\kappa)} \exp\left(\frac{4\sigma_{s/a} M_w}{RT\rho_w D_p}\right) \tag{17}$$

where S is the saturation ratio, D_d is the dry diameter, and the other symbols follow the original Köhler equation (section 1.4.2). The overall hygroscopicity parameter, κ, is given by summation of the product of the volume fraction, $\varepsilon_i = V_{si}/V_s$, and κ for every individual (dry) component:

$$\kappa = \sum_i \varepsilon_i \kappa_i \tag{18}$$

where V_s is the volume of the dry particular matter and V_{si} the volume for each individual component. The relationship between critical supersaturation (%) and dry diameter is shown in Figure 3, which has been adapted from Figure 2 of Petters and Kreidenweis [128]. Data from several single- and multi-component particle types for critical supersaturations with respect to particle dry diameter are from laboratory experiments. The value of κ for these particles ranges from 0.001 to 1. For hygroscopic inorganic species such as ammonia nitrate and mixtures composed of a large amount of inorganics, κ is close to the line of $\kappa = 1$. For moderately hygroscopic organic species, CCN activities correspond to κ values between 0.05 and 0.5. For some insoluble particles with a very small amount of hygroscopic inorganic species, or certain chemically aged particles, CCN activities correspond to κ values between 0 and 0.01.

1.5 Growth of droplets by condensation

The fundamentals of cloud formation process is based on air parcel theory. Considering an air parcel with aerosols inside: as the parcel rises up, according to thermodynamics law, it would cool and expand. This would generate supersaturation and the change of supersaturation can be expressed as [148]

$$\frac{ds_v}{dt} = \left(\frac{\Delta H_v M_w g}{c_p R T^2} - \frac{g M_a}{RT}\right) W - \left(\frac{p_a M_a}{p^o M_w} + \frac{\Delta H_v^2 M_w}{c_p R T^2}\right) \frac{dw_L}{dt} \tag{19}$$

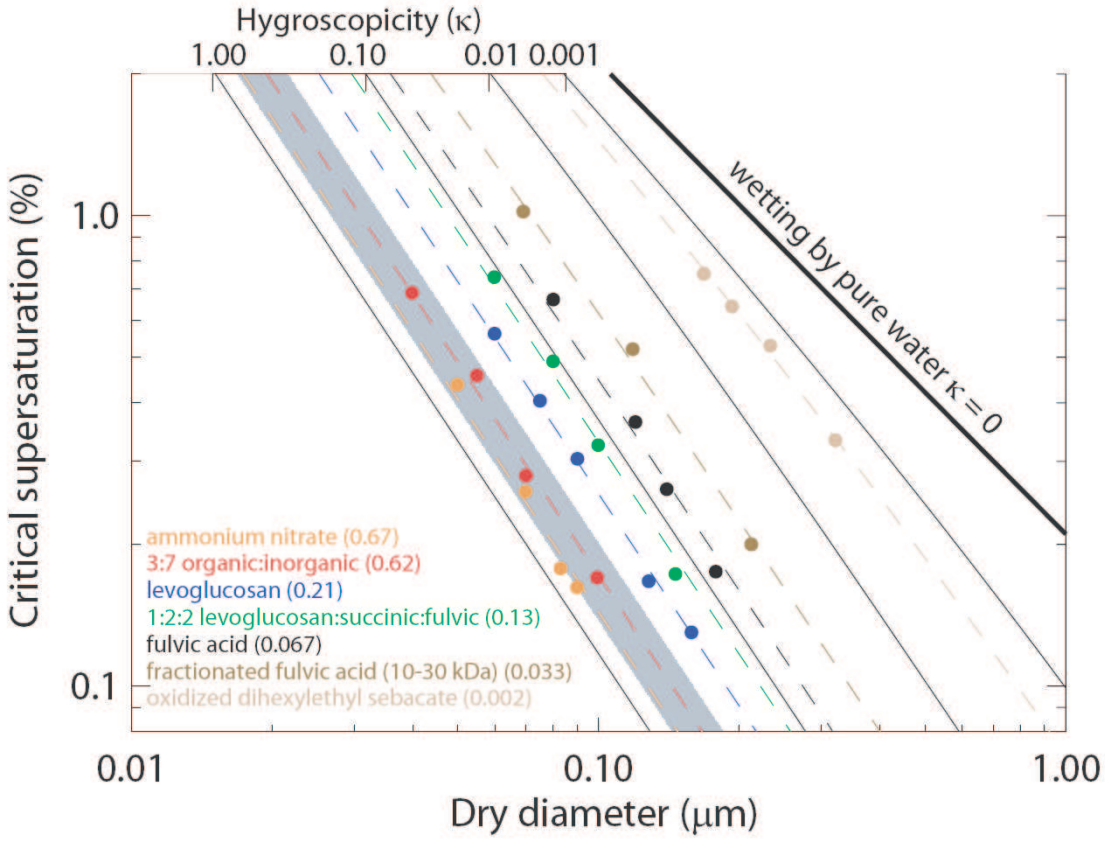

Figure 3: The data of critical supersaturation versus dry diameter for pure compounds, organic mixtures, organic-inorganic mixtures [128].

where s_v is the supersaturation, R is ideal gas constant, T is temperature, g is gravity, ΔH_v is the latent heat of condensation, c_p is the heat capacity of air, p_a is air pressure, p^o is the saturation vapor pressure, M_a, M_w is the molecular weight of air and water, respectively. W is the updraft velocity and dw_L/dt is the change rate of liquid water mixing ratio. The first term on the right hand side is the generation of supersaturation caused by upward motion and the second term represents the consumption of supersaturation due to the condensation of water vapor. The liquid water mixing ratio is obtained based on integration of the liquid water mixing ratio from all droplets

$$w_L = \frac{\rho_w}{\rho_a} \frac{\pi}{6} \sum_{i=1}^{n} N_i D_{pi}^3 \tag{20}$$

where n is the number of groups of droplets, D_{pi} is the diameter of droplet and ρ_a are ρ_w is the density of air and water, respectively. Once the supersaturation profile is known, the number of cloud droplets activated from particles can be determined.

The growth of an individual droplet governed by water vapor diffusion for a continuum regime (when diameters of cloud and fog droplets are larger than 1 μm) can be expressed as follows:

$$\frac{dm}{dt} = 2\pi D_p D_v (c_{w,\infty} - c_w^{eq}) \tag{21}$$

where m is the droplet mass, D_v is the water vapor diffusivity, $c_{w,\infty}$ is the water vapor concentration far from the droplet, and c_w^{eq} is the droplet equilibrium water vapor concentration. Considering that noncontinuum effects cannot be neglected for very small cloud droplets, a term for modified diffusivity, $D_v^{'}$, is introduced:

$$D_v^{'} = \frac{D_v}{1 + \frac{2D_v}{\alpha_c D_p} \left(\frac{2\pi M_w}{RT}\right)^{1/2}} \tag{22}$$

where α_c is the water accommodation coefficient (often called the effective water uptake coefficient) describing the probability of a water molecule sticking on the surface of a droplet when it hits the droplet. The value used for α_c determines the magnitude of the correction. A wide range of α_c, from $\sim$0.001 to 1, has been reported

from experiments [132]; however, the effect of the uncertainty of α_c on droplet growth prediction under natural conditions is small. The growth rate of an individual droplet in terms of diameter can be expressed as

$$D_p \frac{dD_p}{dt} = \frac{S_{v,\infty} - \exp\left(\frac{4M_w\sigma_w}{RT_\infty\rho_w D_p} - \frac{6n_s M_w}{\pi\rho_w\left(D_p^3 - d_u^3\right)}\right)}{\frac{\rho_w RT_\infty}{4p^o(T_\infty)D_v' M_w} + \frac{\Delta H_v\rho_w}{4k_a' T_\infty}\left(\frac{\Delta H_v M_w}{T_\infty R} - 1\right)} \tag{23}$$

where $S_{v,\infty}$ is the ambient saturation, T_∞ is the temperature of the environment, d_u is a sphere of diameter that is equivalent to the insoluble particle fraction, and $k_a^{'}$ is the modified form of thermal conductivity. Equation 23 describes the growth (or evaporation) of an atmospheric droplet. Growth (or evaporation) is driven by the the difference between the ambient saturation and equilibrium saturation for the droplet. The equilibrium water vapor saturation at the droplet surface is determined by the effects of the Kelvin term and the solute term (Equation 13). According to Equation 23, droplets should grow when the ambient saturation is greater than the equilibrium saturation of droplets. Similarly, evaporation of droplets occurs when the ambient saturation is less than the droplet equilibrium saturation. The corrected thermal conductivity ($k_a^{'}$) accounting for non-continuum effects can be expressed as

$$k_a^{'} = k_a \Bigg/ \left[1 + \frac{2k_a}{\alpha_T D_p \rho c_p}\left(\frac{2\pi M_a}{RT_a}\right)^{1/2}\right] \tag{24}$$

The detailed 1-D numerical parcel model developed by Nenes et al. [121] is used to simulate the evolution of droplet growth due to condensational growth. The parcel model solves the growth of each particle which is described by a system of ordinary differential equations. The simulated evolution of droplet spectrum is shown in Figure 4, which is the droplet size distribution evolution at in-cloud depth heights of 17, 100, and 300 m for C6 flight cloud 1 of CRYSTAL-FACE (see [118] or Chapter 4 for cloud information). It can be seen at an in-cloud height of 17 m, there is a gap between interstitial particles and activated drops. The sizes of droplets increase as a function of height and the cloud droplet spectrum narrows as growth continues.

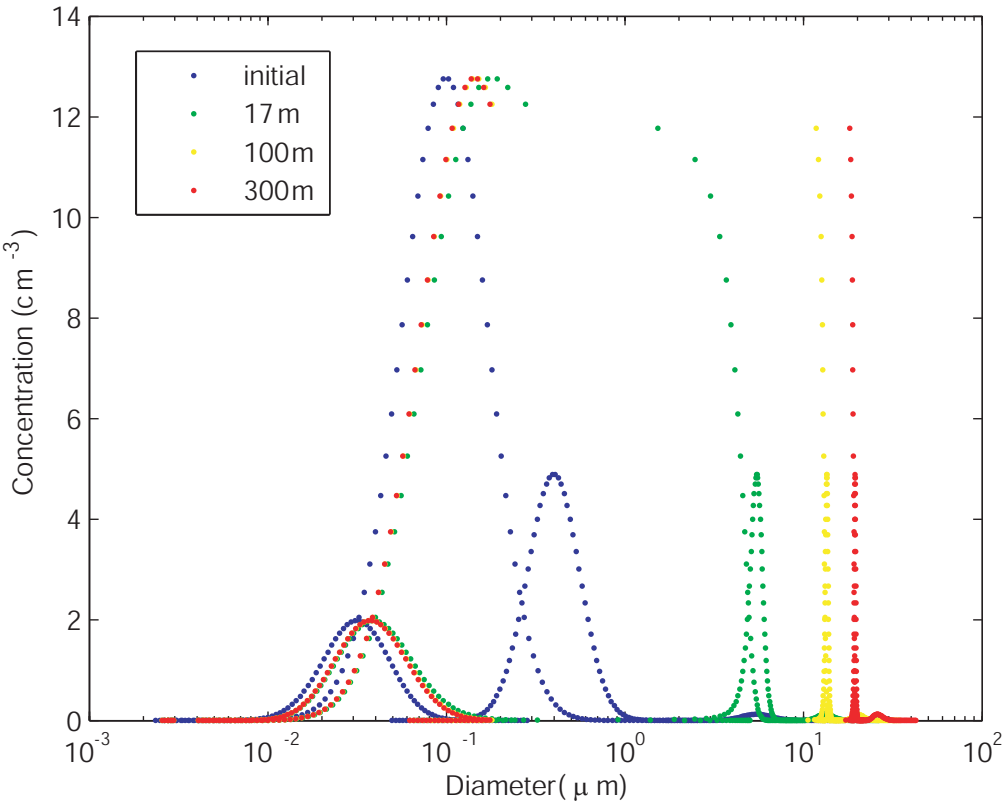

Figure 4: Droplet spectrum at initial condition, in-cloud depth height = 17, 100, and 300 m for C6 flight cloud 1 of CRYSTAL-FACE. (see [118] or Chapter 4 for cloud information)

1.6 Effect of entrainment

The previous section, considers an adiabatic rising air parcel which is treated as a closed system. In real clouds, however, a rising parcel often mixes with the surrounding air. The occurrence of entrainment lowers the content of liquid water compared with values expected on the basis of a closed saturated ascent. The temperature difference between the air parcel and the environment given by an adiabatic calculation is around 2 to 3 ^{o}C; however, the temperature excess is only 1 ^{o}C or less based on observations for regions of updrafts. For a system composed of a rising parcel of air with a water vapor mixing ratio w_ν, a temperature T, a surrounding environmental water vapor mixing ratio $w_\nu^{'}$ and temperature $T^{'}$, the cloud lapse rate Γ_c can be derived as [132, 148]

$$\Gamma_c = -\frac{dT}{dz} = \frac{g + e\left[\Delta H_\nu \left(w_\nu - w_\nu^{'}\right) + \hat{c}_p \left(T - T^{'}\right)\right]}{\hat{c}_p + \Delta H_\nu \left(dw_{\nu s}/dT\right)} \tag{25}$$

or equivalently

$$\Gamma_c = \frac{g}{\hat{c}_p} + \frac{\Delta H_\nu}{\hat{c}_p}\frac{dw_{\nu s}}{dz} + \frac{e}{\hat{c}_p}\left[\Delta H_\nu \left(w_\nu - w_\nu^{'}\right) + \hat{c}_p \left(T - T^{'}\right)\right] \tag{26}$$

where the entrainment rate, e, is given by

$$e = \frac{1}{m}\frac{dm}{dz} \tag{27}$$

The entrainment rate is also often expressed as $e = 1/l$, where l is the length scale characterizing the mixing process. If $e > 0$, then $\Gamma_c > \Gamma_s$. For cloud formation including the effects of entrainment, the change of temperature is expressed as [148]:

$$-\frac{dT}{dt} = \frac{gW}{c_p} + \frac{\Delta H_v}{c_p}\frac{dw_v}{dt} + e\left[\frac{\Delta H_v}{c_p}\left(w_v - w_v^{'}\right) + \left(T - T^{'}\right)\right]W \tag{28}$$

and the rate of change of the water vapor mixing ratio, w_v, is a function of the rate of change of the liquid water mixing ratio, w_l, :

$$\frac{dw_v}{dt} = -\frac{dw_L}{dt} - eW\left(w_v + w_L - w_v^{'}\right) \tag{29}$$

Note that the description of cloud formation which includes the effects of entrainment is more close to reality.

1.7 Growth of droplets by collision coalescence

Diffusional growth of droplets tends to produce a uniform size distribution with droplets ranging in size from 1 to 10 μm. Note the dominance from diffusional growth to collection growth generally occurs for a drop radius between 10 to 20 μm. A generation of big droplets could initialize collision-coalescence and cause fast growth of droplets; this is also the main mechanism for broadening of droplet spectra. The collision process considered here applies only to the interactions between pairs of droplets, where the collision efficiency, E, is the ratio of the actual collision cross-section to the geometric cross-section [132]

$$E \equiv \frac{y_c^2}{(a_1 + a_2)^2} \tag{30}$$

where y_c is the initial offset of the center of the smaller sphere (lower) of radius a_2, from the vertical line through the center of the larger sphere (upper) of radius a_1. The theoretical collision efficiencies (Figure 14-5 (p. 583 [132])) as presented as function of p-ratio(the ratio of the collected droplet radius, a_2, to the collector drop radius, a_1) and collector drop radius reveal that the differences of E derived from superposition approach are larger for $a_1 \geq 30\mu$m as compared to efficiencies computed from the approximate boundary value analysis. Generally, the collision efficiencies increase as increase of collector size and p-ratio. The discrepancy among these approaches is especially large when p-ratio is close to 1. This is mostly related to the inherent deficiency of superposition approach that the individual flow fields do not interact. Therefore, the strength of wake formation behind the leading two drops falling in close proximity will be overestimated and the underestimation of strength of the viscous interactions between the spheres would further enhance this effect.

1.7.1 Collection growth based on continuous model

If a drop with radius a_1, and mass m_1 falls through a cloud of uniform droplets of radius a_2 with liquid water content w_L, the growth rate of the drop, based on continuous growth model, is expressed as

$$\frac{dm_1}{dt} = E_c\pi(a_1 + a_2)^2(U_{\infty,1} - U_{\infty,2})w_L = K(a_1, a_2)w_L \tag{31}$$

where E_c is the collision efficiency, and $U_{\infty,1}$ and $U_{\infty,2}$ are the fall velocities of a_1, a_2, respectively. The collection kernel for the hydrodynamic capture, $K(a_1, a_2)$, is then defined as

$$K(a_1, a_2) = E_c\pi(a_1 + a_2)^2(U_{\infty,1} - U_{\infty,2}) \tag{32}$$

Equation (31) assumes that the drop falls in a cloud within a uniform and continuous distribution of small drops ($a_2 < a_1$). The growth rate of each a_1 drop would then be the same as specified by Equation (31).

Equation (31) can be modified to apply to the case when an a_1 drop falls through a polydisperse cloud droplet distribution, $n(a)$. Then, growth of the drop becomes

$$\frac{dm_1}{dt} = \frac{4\pi\rho_w}{3}\int K(a_1, a_2)n(a_2)a_2^3 da_2 \tag{33}$$

Assuming $E_c = E = \frac{y_c^2}{(a_1+a_2)^2}$ (Equation 30), Equation (33) in terms of the radius growth rate then becomes

$$a_1^2\frac{da_1}{dt} = \frac{\pi}{3}\int y_c^2(a_1, a_2)\left[U_{\infty,1} - U_{\infty,2}\right]a_2^3 n(a_2)da_2 \tag{34}$$

Several studies use Equation (34) to calculate the growth rate of drops, the results demonstrate that the growth rate is significantly larger for a cloud composed of a polydisperse droplets as compared to a cloud of monodisperse droplets, even though the monodisperse drops are larger than three-quarters of the drops in the polydisperse cloud. The study by Braham [30] shows that the development of precipitation-sized drops are faster for maritime clouds, which have broader droplet size distributions

and larger liquid water contents. Examples show that the growth rates of drops are very sensitive to the droplet spectra and the amount of liquid content in clouds.

1.7.2 Collection growth based on kinetic model

The continuous model for collection growth predicts much longer growth times (by a factor of two or more) for precipitation-sized drops than the necessary times from observations. This is because continuous model does not consider the stochastic feature of collection growth. There is a "favored" small fraction of drops which grow much faster than the average rate, this process happens by chance and is very important in the overall development of precipitation. The formula describes the stochastic growth of a population of droplets as a result of collision-coalescence are the form of kinematic collection equation (KCE) [132]

$$\frac{\partial n(m,t)}{\partial t} = \frac{1}{2}\int_{m_0}^{m} n(m_c,t)K(m_c,m')n(m',t)dm' - \int_{m_0}^{\infty} n(m,t)K(m,m')n(m',t)dm' \tag{35}$$

where $n(m,t)$ is the drop number distribution at time t, and $K(m_c,m')$ is the collection kernel that gives the rate at which a droplet of mass $m_c = m - m'$ is collected by a droplet of mass m' forming a drop of mass m. The first term on the right hand side represents the source of a drop of mass m due to coalescence of two droplets that results in mass m; the coefficient $\frac{1}{2}$ is corrected for double counting. The second term describes the sink of m due to the drop's collision with any other droplet. The study by Telford [161] was the first to use this method to investigate drop collection problem. He used the KCE to simulate an idealized cloud consisting initially of just two drop sizes, where the collision kernel is a constant. His results showed that, as compared to the growth rate predicted by continuous model, a factor of 50 times rate was obtained from the KCE simulation for a small fraction of large drops. Later, in the computations carried out in study of Twomey [165] showed that for the drop concentration of 100 m^{-3}, the stochastic model predicted almost ten times larger growth

rate than in the continuous model. An example of the evolution of a droplet spectrum is shown in Figure 5, which shows a numerical code released from Bott [27] is used for solving KCE. The parameters in numerical code of Bott [27] for simulating droplet spectrum evolutions are specified as follows: time step = 10 seconds, mode radius of initial distribution = 10 μm, total water content = 1 g m^{-3} and the scaling factor for setting mass grid of particles = 2. The gravitation kernel from Hall [67] is used for computing growth of droplets based on collision and coalescence. The initial droplet spectrum and spectrum at three simulation times (20 mins, 40 mins and 60 mins) are displayed in Figure 5, which shows that the second mode of the spectrum in radius around 500 μm is formed at 40 mins. To see the effect of turbulence on droplet spectrum evolution, Figure 6 shows two droplet spectra at a simulation time of 30 mins using gravitational and turbulent kernels, respectively. The turbulent kernel used is based on the work of Zhou et al. [180] and the total collection kernel is taken as the sum of gravitational and turbulent kernels. The dissipation rate, e = 300 cm^2s^{-3}, and fluctuational velocity, $u' = 3.5$ ms^{-1}, are used to calculate the turbulent kernel. A detailed description of the formulation of the turbulent kernel is provided in Chapter 4 and the effect of different kernels on the autoconversion rate is also discussed. Turbulence accelerates drop growth and the second mode of spectrum occurs after 20 mins of simulation, which cannot be seen when applying the gravitation collection kernel (Figure 5). The simulated droplet spectrum under the influence of turbulence is sensitive to the conditions specified for calculating the turbulent kernel. Figure 7 shows two droplet spectra for turbulent conditions of e = 277.7 cm^2s^{-3}, $u' = 1$ ms^{-1} and e = 34.7 cm^2s^{-3}, $u' = 0.5$ ms^{-1}, as specified in continental and oceanic grids for kernel computation (Chapter 5). Under stronger turbulent conditions (analogous to the continental grid setting for the turbulent kernel), a peak can be seen around 300 μm radius where a large drop has been formed at simulation time = 30 mins, but no peak is formed for the oceanic case.

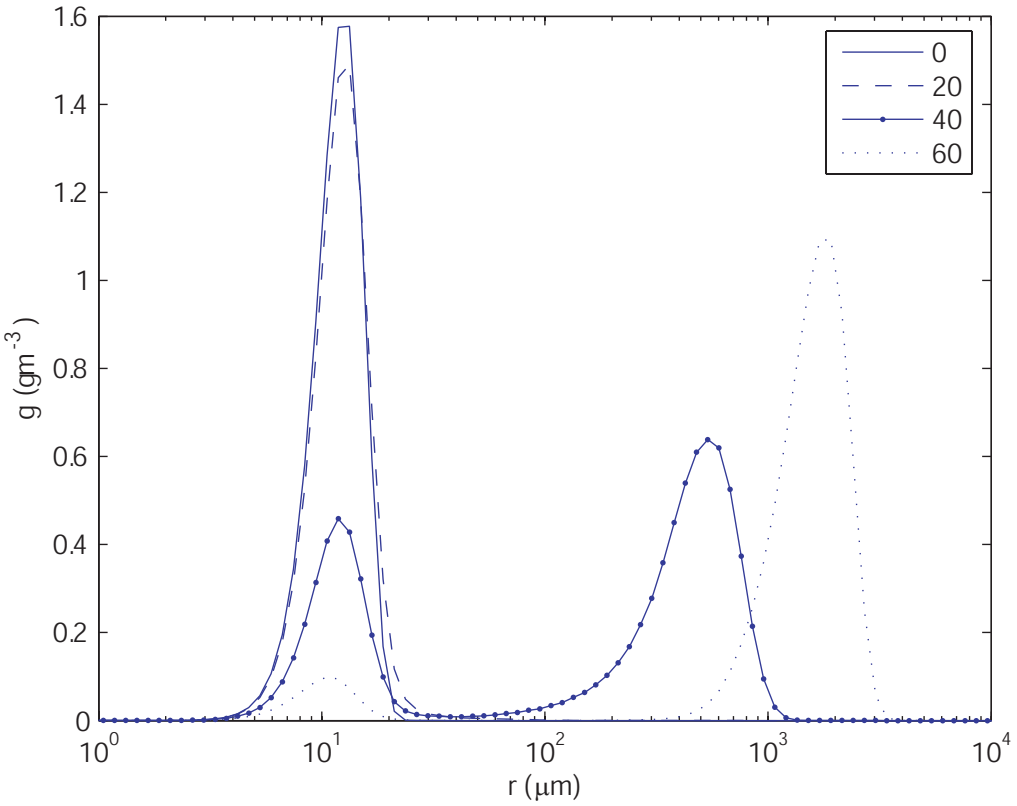

Figure 5: This plot shows a temporal evolution of droplet mass distribution for simulation times of 20, 40 and 60 mins. The turbulent kernel as presented in Zhou et al. [180] is used for KCE

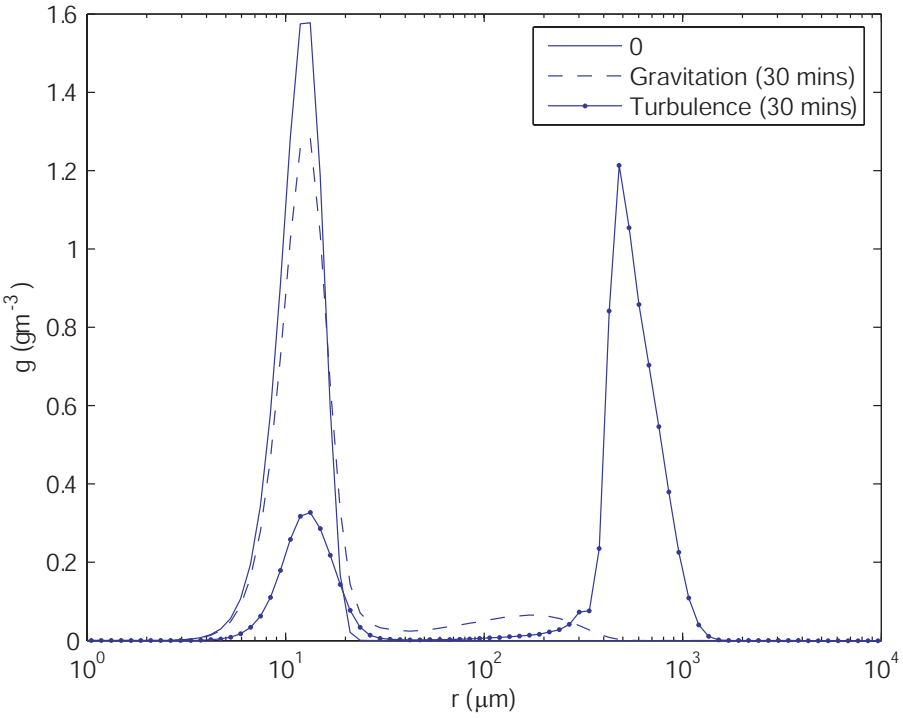

Figure 6: Comparison of droplet spectrum using gravitational kernel and turbulent kernel at simulation time = 30 mins.

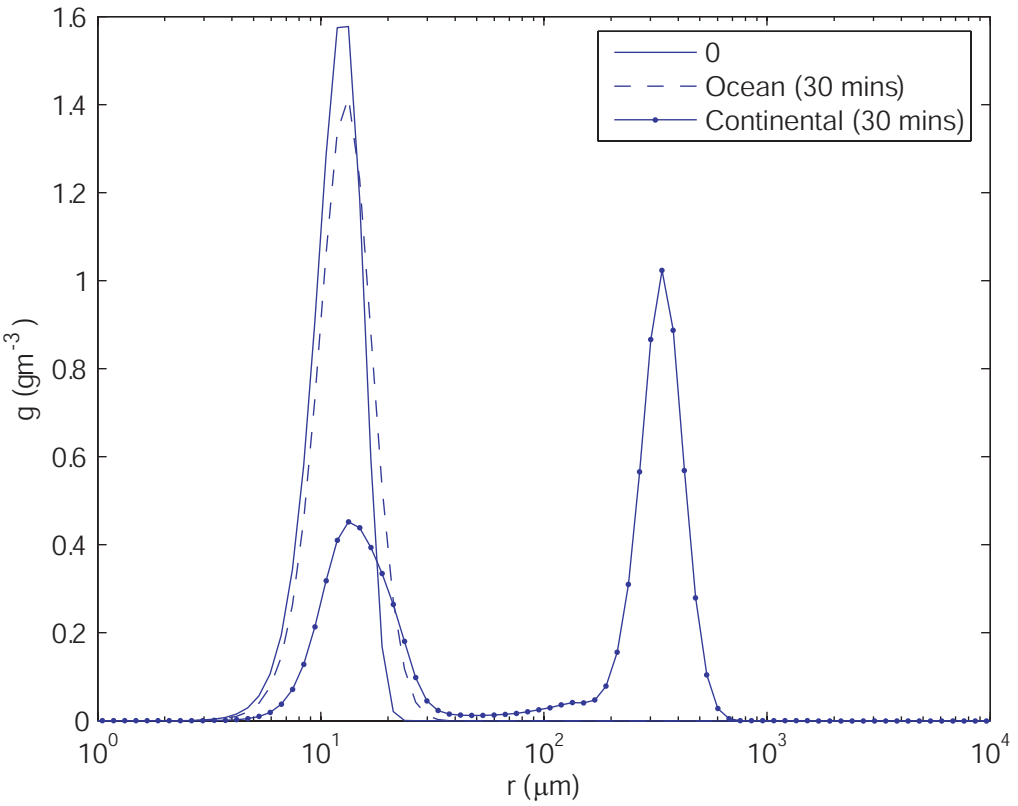

Figure 7: Sensitivity of turbulent conditions on the evolution of droplet spectra. The size distribution of drops is plotted at simulation time = 30 mins.

1.7.3 Effects of electrostatic on collision coalescence

The electrostatic forces for cloud drops can cause a significant effect on collision and coalescence. There are several theoretical and experimental studies investigating the possible influence of electrostatic forces. Latham [98] conducted a field experiment, in which they found that when the strength of an external electric field exceeds 150 V cm^{-1}, an enhancement in the growth rate of 130 μm radius drops which collide with 15 μm diameter drops (all with a negligible charge) was obtained. The growth rate was about 20% higher than the case of no field when the external field strength is at 500 V cm^{-1}. A further increase in the field strength up to 1200 V cm^{-1} does not enhance the growth rate. When the electric field reaches 1600 V cm^{-1}, a 100% increase in growth was obtained compared to the growth rate with a zero field. Not only does the electric field affect collision efficiency, the amount of charges in drops also can change the collision efficiency.

For a given pair of drop, the effect of charges on the collision efficiency generally increases with increasing drop charge in the absence of an external field. Similarly, the collision efficiency increases with increasing field strength in the absence of drop charge. If the case of a drop with radius a_1, the effect of an external field and drop charge on the collision efficiency depends on the drop size ratio $p = a_2/a_1$, where a_2 is the collected drop. The largest effect is associated with $p \ll 1$ and the least effect for intermediate p, while the effect increases again for $p \approx 1$. The charge of colliding drops a_1, a_2 also have a significant effect on the collision efficiency. The study of Schlamp et al. [145] calculated collision efficiencies for the case of a negatively charged a_1 drop colliding with a positively charged a_2 drop in a negative electric field. It was found that the computed collision efficiencies are largely different from the values for a positively charged a_1 drop calculated by Schlamp [144].

1.8 Precipitation

To generate precipitation, cloud drops need to grow into rain drop sizes of around 1 mm. This is achieved by cloud drops colliding as described in Section 1.7. Two main theoretical bases for describing growth of cloud droplets by the collection process are the continuous model (Section 1.7.1) and the kinetic model (Section 1.7.2). In the continuous model, drops grow by collecting small droplets underneath their falling pathways and calculations are based on the assumption of uniformly distributed cloud droplets in space. Therefore with the same growth time, drops with initial equivalent diameters would grow to the same sizes in the final state. However, the collection growth of drops in the atmosphere is a discrete process. A large drop, which collides with smaller droplets earlier and experiences a higher collection frequency, may exhibit a greater extent of growth. The larger drops can trigger precipitation formation as a result of faster growth and thus their existence in the atmosphere is very important. The typical concentration of large drops required to initialize rainfall is one per liter of air. So only one big drop out of a million cloud droplets can trigger an efficient growth of drops and produce precipitation. The presence of large drops is identified from atmospheric droplet spectrum measurements, and the observed droplet size distributions are often broader than theoretical predictions. A wider droplet spectrum may have a higher chance to develop into a precipitating state within the period of the cloud lifetime. Thus to predict precipitation, it is of particular importance to understand the evolution of droplet spectra and correspondent influential factors. These are discussed in the following sections.

1.9 Droplet spectra

As discussed in previous sections, both condensation and collision-coalescence could affect the shape of the droplet size distribution. The droplet spectra formed, based on the condensation mechanism, tend to narrow the distribution and cannot provide

a realistic explanation of the timescale for rain development. A 20-min time interval is often observed and reported as an average time for the initiation of warm rainfall [139] at 900 mb, 273 K and 0.05 % supersaturation of NaCl nuclei with 10^{-12} g mass. The initial particle with radius 0.75 μm needs $\sim$1.64 hours to grow to radius of 20 μm based on the calculation of diffusional growth [112]. Even though collision-coalescence process in this case is governed by gravitation, theoretical prediction of droplets that grow to 20 to 100 μm in radius need about an hour [132]. In general, the question for the rapid growth of droplets with a radius of 10 to 50 μm remains unsolved. Meanwhile, why the observed droplet spectra are generally broader than the predicted distributions is not fully understood [32, 38, 86]. This section provides a brief review of factors that affect droplet spectra.

1.9.1 Dynamical variability

The updraft velocity observed in clouds exhibits a lot of variability, Figure 8 shows the distribution of updraft velocity measured for research flight 9 of cloud 1 (RF9C1) during the MASE campaign. This flight is adapted from Chapter 2 of this thesis and is used for the closure study. It can be seen for this cloud deck, the observed frequency of low updraft is higher than high updraft and this may be a result of small-scale turbulence. The variations in updrafts are postulated as a mechanism for droplet spectrum broadening. Using an adiabatic parcel model, Erlick et al. [52] found that for the low initial updraft velocity, even though the temperature profile is weakly buoyant, the acceleration of updraft would cause new drop formation above the cloud base. This would generate new modes in the drop spectrum and broaden the size distribution towards smaller drops. Erlick et al.'s study also pointed out this new drop nucleation can also occur via parcel recirculation that downdraft droplets may not fully evaporate, and this could reduce the maximum supersaturation when subsequently arises.

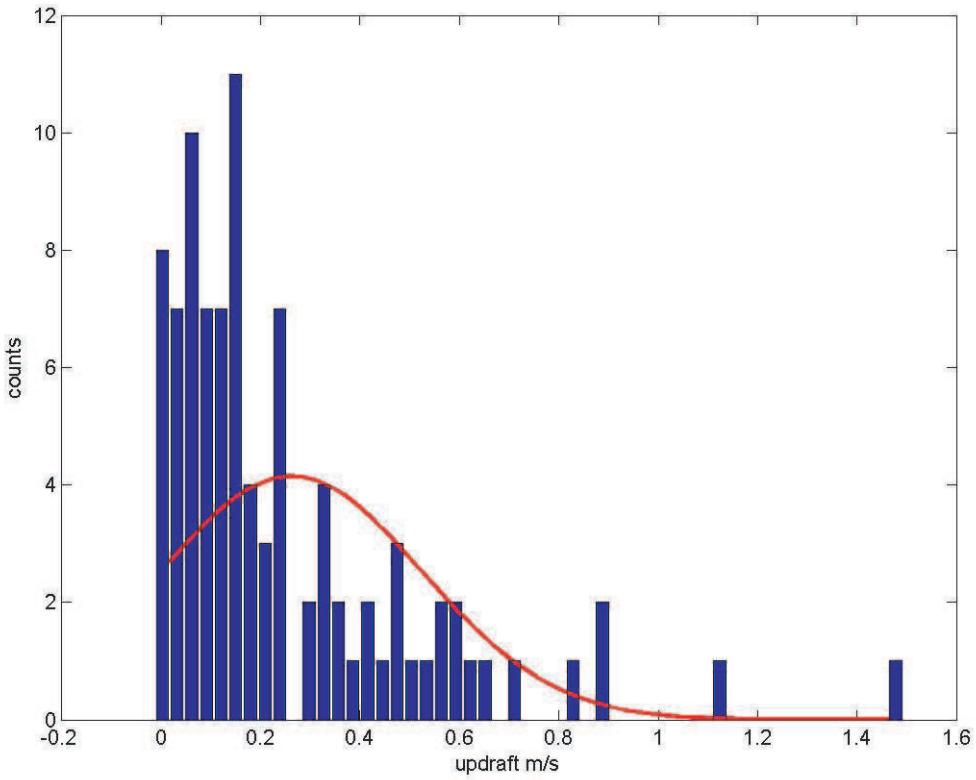

Figure 8: Distribution of updraft velocity for research flight 9, cloud 1 (RF9C1) of MASE. The red line is the fitted normal distribution. This data was adapted from Chapter 2 of this thesis.

1.9.2 Ripening process

The "ripening process" is a result of the thermodynamical instability in droplet spectra. Unstable droplets originate from particle populations with different salinity and sizes. Because there is competition of water among droplets, some droplets will grow while other will evaporate. This may lead to a broader droplet size distribution to larger drops as a result of evaporation of smaller droplets. This "ripening process" has been suggested as a mechanism for droplet spectrum broadening in stratiform clouds [36, 174].

1.9.3 Giant cloud condensation nuclei

Giant cloud condensation nuclei (GCCN) commonly refers to large droplets with radii ranging from 2 - 5 μm. GCCN is composed of dust particles coming from natural dust events and sea-salt particles generated by wind breaking of bubbles over the ocean surface; the latter mechanism depends on wind speed, relative humidity, and atmosphere stability. The effect of GCCN on warm rain initiation was investigated in many studies [18, 97, 178] that tried to identity whether the presence of large particles can facilitate the growth of drops by collection of small droplets to form raindrops. However, as concluded by , GCCN is unlikely to be the universal dominant mechanism of droplet spectrum broadening and raindrop formation. In the case of a narrow spectra with high cloud water content, as in such simulation, there is no interaction between small droplets of similar size.

Khain et al. [86] also conducted two simulations with and without considering giant and ultra-giant nuclei. Their results show the evolution of droplet spectrum is very similar in these two cases, which indicates that the process of spectrum self-broadening is dominating. Therefore the additional giant and ultra-giant nuclei do not contribute significantly to the width of the spectrum. In another pair of simulation by Khain et al. [86], an initial droplet spectrum with a mean center of 7 μm radius,

a cloud water amount of 1 g m^{-3} and droplet concentration of 1100 cm^{-3} is specified. The difference in the simulations is that the second experiment adds droplets of radii above 20 μm with a concentration of 400 m^{-3} in the initial droplet spectrum. Khain et al. [86] results show that even assuming such unrealistically large droplets, the rate conversion of rain water is still comparably slow.

1.9.4 The effect of turbulence on droplet collisions

The process of collisions between cloud droplets can be a potentially important mechanism for large drop formation. Theoretical calculations and laboratory experiments cannot produce droplet spectrum broadening in a reasonable time for the condition where collisions of droplets are governed by gravitation only. Vohl et al. [168] and Vohl et al. [169] conducted wind tunnel experiments and their results show that the presence of turbulence accelerates droplet growth by the collision process. Compared to the collision efficiency calculated under calm air conditions, a significantly higher efficiency is obtained for a turbulent air flow [129]. The effects of turbulence on particle interactions and their motions has been extensively studied; the simulation from Khain et al. [86] showed that large drops ($\sim$40 μm in radii) form earlier in a turbulent flow, but no spectrum broadening was observed in a pure gravity case. In the time it takes to form raindrops in the turbulent droplet spectrum, there are still no raindrops forming in the calm air simulation.

1.9.5 Preferential concentration and fine cloud structure

Preferential concentration occurs due to the nature of turbulence. Instead of randomly dispersing in a cloud, droplets tend to concentrate in regions of low vorticity in a turbulent flow. The formation of concentration inhomogeneity leads to the development of high supersaturations in regions of high vorticity (low droplet concentration) and low supersaturations in regions of low vorticity (high droplet concentration). Therefore, enhanced droplet growth occurs in a strongly fluctuating supersaturation field

where droplet concentration is low. This mechanism helps to explain the existence of large drops in he tail of droplet spectrum and the presence of bimodal spectrum caused by an in-cloud nucleation above the cloud base [150]. It is known as the collision process and it is more effective in an inhomogeneous droplet distribution field where local droplet concentration is much higher than the average concentration. This increased concentration of large droplets enhances collision process and further accelerates formation of even larger drops. This would cause a droplet spectrum broadening to occur earlier, as simulated by Pinsky et al. [130].

1.9.6 Entrainment mixing

Entrainment and mixing has been proposedo as one of the main mechanisms for droplet spectrum broadening. The two major mechanisms include a) homogeneous mixing and b) inhomogeneous mixing. Homogeneous mixing refers to the process where entrained air is assumed to spread instantaneously throughout the entire lateral cross-section of the level of entrainment. Mixing is assumed to be uniform and to maintain saturation, all drops evaporate and drop sizes decrease. In contrast to homogeneous mixing, inhomogeneous mixing assumes that the evaporation of drops occur only in neighboring regions where entrainment is introduced. Evaporation proceeds until saturation is reached and then the lateral spread of entrained air continues throughout the level.

The model of homogeneous mixing developed by Warner was attempted to explain the observed droplet size distribution [76]. He found that the simulated droplet spectra depends on the properties of entrained air; for example, if the entrained air was nuclei free, the spectral broadening would not be significant. When the entrained blob contained nuclei, a significant droplet spectrum broadening was obtained, but the simulated spectrum was often associated with a single broad peak which is different from those from observations. Many assumptions and simplifications were made

in numerical models to study the complicated process of entrainment and mixing; this leads to a large degree of uncertainty. The uncertain factors in simulated spectra include the size of the entrained blob, the entrainment rate, the way to select the region of the parcel which is replaced with, the speed at which entrained blobs propagate in a cloud, the property of entrained air (e.g., nuclei free or nuclei contained), and so forth.

1.10 Large Eddy Simulation

A large eddy simulation (LES) model explicitly simulates the large eddy fields and parameterizes the small eddies. It can be used to study the planetary boundary layer, and it provides three-dimensional time-evolving velocity and temperature scales at a resolution constrained by computational availability. The application of LES is broad, including investigating entrainment across the inversion [157], studying transition from one type of cloud to another [175], and generation of databases of different atmospheric flow regimes for evaluation, and refinement and development of parameterizations used in large-scale models [96].

The LES model has been used as a tool for developing and testing cloud theories and models, the evaluation of the fidelity of simulations is needed to be executed. For simple cases such as simulations of a clear, convective boundary layer, LES has been shown to be relatively robust [123]. For more complex cases, however, model intercomparisons have shown considerate uncertainty in predicting important statistics and bulk parameters. For example, the study of Bretherton et al. [33] conducted simulations of a smoke cloud beneath a temperature inversion in the 1995 Global Energy and Water Cycle Experiment (GEWEX) Cloud System Studies (GCSS) model intercomparison. Their results show that the difference in the entrainment rates and other statistics predicted by various LES models can be up to a factor of two. The cloud-scale convection driven by radiative cooling at the top of cloud introduces the

entrainment across the inversion and results in growth of the boundary layer. The study of Stevens et al. [156] compared simulations of trade-wind cumuli and they found the parameters of stratiform cloud fraction and the variance of total-water mixing ratio are highly sensitive to the choice of numerical method, spatial resolution and subgrid-scale turbulence model. It is important to evaluate the robustness of LES because it predicts parameters of the boundary-layer height, entrainment rate, and cloud fraction, which are important variables in the parameterizations used in global circulation models.

1.11 Representation of clouds and aerosol-cloud interactions in GCMs

1.11.1 Bulk microphysics

The bulk approach uses the one or several moments of a size distribution of hydrometeors to addresses cloud microphysics. The comment moments used include a number mixing ratio, mass mixing ratio, surface area, radar reflectivity, and so forth. For example, the first formula for describing the process of autoconversion of cloud water to rain was proposed by Kessler [84]. The proposed equation is highly intuitive (the higher the liquid water content, the larger the autoconversion rate) and does not include any microphysical considerations. Later on, Manton and Cotton [113] improves Kessler's type of autoconversion where autoconversion rate is not only a function of liquid water content but also depends cloud droplet number concentration.In the analytical formulation derived by Liu and Daum [103], the autoconversion parameterization is expressed in terms of the spectral width of the size distribution, in addition to the amount of liquid water and cloud droplet number concentration. This bulk microphysical scheme can also be derived from parcel or box detailed bin-microphysics simulations (e.g., [19, 87, 147]). Using the basis functions such as gamma or log-normal distributions, multi-moment bulk schemes can explicitly predict the evolution of droplet spectra for the processes involving vapor deposition and evaporation,

stochastic collection, and sedimentation.

1.11.2 Spectral bin microphysics

Cloud growth processes depend largely on the size of the drop, which can be described using size-resolved or explicit bin microphysical methods. For the Lagrangian approach, particles are represented at discrete sizes and the growth of each particle due to condensation is calculated on a moving mass grid. This approach provides a numerically correct solution to calculate particle growth naturally without assuming artificial distinction for different particle classes. The concept of the Lagrangian method is used in i) cloud parcel models (e.g., [121]) which simulates an adiabatically rising air parcel and ii) trajectory ensemble models (e.g., [158]) in which air parcels are moved according to some known trajectories through a cloud.

As mentioned earlier, the Lagrangian approach is suitable for simulating condensational droplet growth but is not easily adapted to study the growth of drops by the collision and coalescence. On the other hand, the Eulerian, or the fixed bin, microphysical models can be used for this process. It has been pointed out in several studies that when using the Eulerian approach for simulating collision and coalescence, some issues need to be carefully dealt with to avoid numerical diffusion in mass-transfer equations and rapid production of precipitation-sized drops caused by spurious acceleration in drop growth [161, 22, 23, 91, 24]. The multi-moment representation approach of cloud microphysics within each individual drop bin [28, 39, 83, 99] has the advantages of conserving the mass and number of the size distribution while also reducing the numerical diffusion significantly. Recent studies develop the numerical methods that include a bin representation of aerosols in each individual hydrometeor grid. These approaches are very accurate since the information about aerosol particles within drops and ice particles are carried during the simulation. But this approach suffers computational constraint when it is included in 3-D models. The

commonly used methods use simpler approaches that track dissolved aerosols within each hydrometeor bin.

1.11.3 Determination of cloud droplet number concentration

To study the aerosol-cloud interactions in GCMs, the first question to address is the representation of cloud droplet number concentration (CDNC) in each single GCM grid cell. The early study of Boucher and Lohmann [29] proposed an empirical relationship of CDNC and the mass of sulfate to link aerosols to clouds:

$$CDNC = 10^{2.21+0.41\log(m_{SO_4})} \tag{36}$$

where CDNC in units of cm^{-3} and m_{SO_4} is the mass of sulfate in units of $\mu g m^{-3}$. The problem here is how to connect the cloud water sulfate concentration to the mass of atmospheric sulfate, which depends on the sulfate scavenging efficiency and the in-cloud oxidation of SO_2. The CDNC uncertainty is estimated to br $\pm 10\%$. Applying this empirical approach for predicting CDNC can avoid the need to resolve updraft velocity in relation to cloud formation. A more accurate treatment of cloud drop formation requires a resolution of the aerosol number concentration, its chemical composition and the cloud scale vertical velocity. A more physically based approach for predicting CDNC is derived by Ghan et al. [63], Abdul-Razzak et al. [4], where the number of nucleated particles is expressed as a function of updraft velocity and aerosol concentration. Subsequently, Abdul-Razzak and Ghan [2] extends the activation scheme and uses the sectional representation of the aerosol size distribution to develop a cloud droplet formation module. The number concentration and chemical composition are uniform functions of particle size for each section. Using Köhler theory, the number of activated cloud drops is determined by the maximum supersaturation (s_{max}) of a rising air parcel and is functions of aerosol size distribution and composition. For most cases of idealized and measured aerosol size distributions, the parameterization predicts CDNC within 10% of those obtained by detailed numerical

computations. Similarly, Nenes and Seinfeld [119] and Fountoukis and Nenes [58] developed the cloud activation parameterization, which uses the concept of "population splitting" to simplify droplet growth. The parameterization and has been evaluated by several in-situ campaigns [118, 60]. These mechanistic parameterizations for CDNC predictions have the advantage of being physically based approaches that can be applied to a wide variety of conditions. The updraft velocity relevant to the cloud activation process is either represented by a Gaussian distribution for some GCMs [41] or specified based on turbulent kinetic energy predicted from GCMs [109].

1.11.4 The Cloud scheme in GISS GCM

In this section, a brief summary of the representation of clouds in GISS GCM is provided. The cloud schemes are based on the work by Del Genio et al. [48] and are used in the GISS GCM II prime. For each grid cell, the mean relative humidity, U, is a summation of a cloudy part (with fractional cloudiness b and relative humidity $U_s = 1$) and a clear part (with relative humidity U_0):

$$U = bU_s + (1 - b)\, U_0 \tag{37}$$

The equation for the unitless cloud water content m is expressed as

$$\begin{aligned} \tfrac{\partial m}{\partial t} &= A\,(m) + b\tfrac{Q_c}{L} - (1 - b)\,\tfrac{E_c}{L} - P + S_s \\ &= A\,(m) + \tfrac{Q}{L} + (1 - b)\,\tfrac{E_r}{L} - P + S_s \end{aligned} \tag{38}$$

where t is time, $A(m)$ is the large-scale advection of cloud water, and L is the latent heat of condensation or deposition. Q is the net latent heating of the gridbox due to phase changes from stratiform clouds and is equivalent to the condensation heating in the cloudy part (Q_c) minus the evaporation of cloud water (E_c) and rainwater (E_r) in the clear part (1 - b):

$$Q = bQ_c - (1 - b)\,(E_c + E_r) \tag{39}$$

The conversion rate of cloud water to precipitation, P, is parameterized as

$$P = C_0 m \left\{ 1 - \exp\left[- \left(\frac{\mu}{\mu_r} \right)^4 \right] \right\} + C_1 m P_r \tag{40}$$

where autoconversion of cloud water to rain is formulated as an increasing function of the cloud water density inside the cloud. The water condensate within the cloud is given by $\mu = m\rho/b$ and μ_r is the critical cloud water content, which initializes the rapid conversion process. And C_0 is the limiting autoconversion rate for large cloud water density. The coefficient C_1 is an efficiency factor for accretion of cloud water by precipitation and P_r is the precipitation flux from above. The subgrid-scale dynamical source/sink of cloud water is given by $S_s = S_d + S_e$, where S_d is the convective condensate detrainment and S_e is the cloud-top entrainment instability. The rate of release of latent heating, Q, can be expressed in the form of the gridbox mean relative humidity tendency [159]:

$$Q = \frac{M - L q_s \frac{\partial U}{\partial t}}{1 + \frac{U \varepsilon L^2 q_s}{R c_p T^2}} \tag{41}$$

where M is the convergence of available latent heat (in units of s^{-1}), which includes the effects of temperature and pressure changes; q_s is the saturation specific humidity; ε is the ratio of water vapor molecular weight to dry air molecular weight; R is the dry air gas constant; c_p is the specific heat of dry air; and T is temperature. The total water vapor from dynamic convergence and evaporation can be assumed to be partitioned into the cloudy term bM, which increases the cloud cover of a gridbox, and another term $(1-b)(M+E_c+E_r)$, which increases the cloudiness and the relative humidity of the clear portion. On the Basis of this assumption, the rate change of relative humidity is derived as

$$\frac{\partial U}{\partial t} = \frac{2\left(1-b\right)^2 \left(U_s - U_{00}\right)\left(M + E_c + E_r\right)}{L\left[2q_s\left(1-b\right)\left(U_s - U_{00}\right) + m/b\right]} \tag{42}$$

where U_{00} is the specified threshold relative humidity below which there is no stratiform cloud formation.

1.12 Thesis outline

This thesis presents results from a series of numerical simulations of studying cloud microphysical processes and evaluates cloud parameterizations with in-situ field measurements of cloud droplet size distribution. Chapter 2 analyzes cloud droplet number concentration closure for stratocumulus clouds sampled during the the 2005 MASE campaign and further evaluation of droplet size distribution parameterization is investigated in Chapter 3 which uses CRYSTAL-FACE (cumulus clouds) and CSTRIPE (stratocumulus clouds) droplet spectrum data. Chapter 4 performs the direct integration of KCE to compute autoconversion rates, which are then compared to the predicted values by applying autoconversion parameterizations. The uncertainty of turbulence effect on autoconversion rates is also included by considering two turbulent collection kernels for KCE integration. Lastly, Chapter 5 quantifies the effect of different approaches for calculating autoconversion rate (i.e., by applying parameterized autoconversion scheme or direct KCE integration) on estimating indirect forcing and studies the associated changes in spatial-temporal distributions of cloud and meteorological fields. Chapter 6 summarizes the conclusions and some implications and future directions are provided in Chapter 7. This combination of numerical modeling, simulations, and analysis is designed to help researchers in the field move towards a better understanding of cloud processes and aerosol-cloud-climate interactions.

CHAPTER II

AEROSOL – CLOUD DROP CONCENTRATION CLOSURE FOR CLOUDS SAMPLED DURING MASE

Note: This chapter will be submitted to J. Geophys. Res.

2.1 Abstract

This study analyzes stratocumulus clouds sampled aboard the CIRPAS Twin Otter during the 2005 MArine Stratus Experiment to access cloud droplet closure using a detailed adiabatic cloud parcel model, and, a state-of-the art cloud droplet activation parameterization. A unique feature of the dataset was sampling marine stratocumulus clouds under the influence of ship emissions. A much higher level of correlation between observed N_d and total (and accumulation mode) aerosol number concentration was found as compared to N_d correlation with updraft velocity. Good closure was achieved for both parcel model and parameterization. The error in predicted cloud droplet number concentration, N_d, was mostly sensitive to water vapor uptake coefficient. Optimum closure is obtained if the water vapor uptake is equal to 0.1, in which N_d error is the minimum as 0.14 % (parcel model) and 5.01 % (parameterization).

2.2 Introduction

The most uncertain part of anthropogenic change originates from the aerosol indirect effect (AIE) [75]. AIE is typically classified into the "first" AIE, in which aerosol changes impact cloud drop size and cloud albedo [166]; the second indirect effect refers to impacts of aerosols on cloud lifetime and precipitation efficiency [8]. Both effects are magnified in the presence of enhanced aerosol which act as cloud condensation nuclei (CCN). The activation of CCN into cloud droplets is controlled by the dynamics

(i.e., temperature, pressure, updraft velocity at cloud base) and aerosol characteristics (i.e., size distribution and chemical composition). Detailed numerical cloud models can explicitly resolve the cloud formation processes but the associated computation burden prevents its implement in global circulation model (GCM). Therefore, developing parameterizations to represent these sub-grid aerosol-cloud interaction processes is needed and remain a challenge in GCM development [75].

First-principles (or mechanistic) parameterizations predict CDNC based on updraft velocity, aerosol chemical composition and size distribution [63, 62, 64, 4, 55, 40, 109, 1, 2, 122, 58, 3]. These parameterizations are physically-based (i.e., solve the equations for cloud drop formation but in a simplified way) but still could be subject to large uncertainty associated with sub-grid unresolved updraft velocity [117], aerosol size distribution and chemical composition [138].

Droplet number prediction error can be a result of theoretical limitation, or limitations in the available in formation or simplifications used to describe aerosol properties. The tool for this assessment is the "cloud droplet closure", in which cloud droplet formation theory and parameterizations has been done by comparison of CDNC between parameterization and in-situ measurement. Closure with the parcel model justify the aptness of simulating cloud formation process under polluted conditions, while using the parameterization assess its performance and constrain the uncertainty arising from its simplified physics. [152] found an over-prediction in CDNC compared to measured value for marine stratocumulus clouds during ACE-2; the discrepancy in part was associated with the properties of continental pollution. Excellent closure was achieved by [46] for cumulus clouds of marine and continental origin sampled during the NASA Cirrus Regional Study of Tropical Anvils and Cirrus Layers - Florida Area Cirrus Experiment (CRYSTAL-FACE) and stratiform clouds measured during the Coastal Stratocumulus Imposed Perturbation Experiment (CSTRIPE) [118]. [60] also found very good agreement between predicted and measured CDNC (to within

20 %), for cumuliform and stratiform clouds gathered during ICARTT (International Consortium for Atmospheric Research on Transport and Transformation) experiment. In this study, we assess aerosol-cloud droplet number closure using *i*) a detailed adiabatic numerical cloud parcel model [121], and, *ii*) the modified NS cloud droplet activation parameterization [58]. The observations used in this study were collected on board the CIRPAS (Center for Interdisciplinary Remotely-Piloted Aircraft Studies) Twin Otter aircraft; 5 flights were considered and during which 13 clouds are profiled. Unique feature of MASE was sampling marine stratocumulus clouds under the influence of ship emissions. The evidence of perturbation of ship exhaust on low-level clouds is often referred to ship tracks, which are clouds lines commonly seen in visible and near-infrared satellite images [44, 49, 50]. Changes in cloud drop distributions, cloud drop size and reflectivity have been observed in ship track regions, as well as decrease in drizzle efficiency within [56, 146]. We focus on closure analysis of clouds under influence of ship effluents and sensitivity of closure to water uptake coefficient, chemical mixing state and the size-dependent of aerosol component is studied to justify the robustness of the simplified cloud formation parameterization.

2.3 General Description of MASE

During MASE, a total of 13 research flights were conducted in July 2-17, 2005 off coast of Monterey, California. Aerosols and cloud properties were measured on-board the CIRPAS Twin Otter aircraft in the regime of eastern Pacific marine stratocumulus clouds. Five flights were considered in this study. Aerosol size distribution and chemical composition were taken in under-cloud passes then cloud microphysics, chemistry and turbulence were characterized within in-cloud legs.

2.3.1 Airborne platform and measurements

The measured parameters and instruments onboard the CIRPAS Twin Otter aircraft is summarized in Table 1. Condensation Particle Counter (CPC) and Ultrafine

Condensation Particle Counter use principle of varying butanol supersaturations to measure particle number concentration in diameters above 0.01 and 0.003 μm, respectively. Aerosol size distributions at dry and humid conditions were measured with a Dual Automated Classified Aerosol Detector (DACAD) in aerosol sizes between 0.01 and 0.7 μm. The DACAD consists of two scanning Differential Mobility Analyzers (DMAs) operating in parallel, one measures dry size distribution in relative humidity (RH) less than 20 %, and the other measures wet size distribution at humidified conditions. The size-resolved hygroscopicity (growth factor) is obtained from the dry-wet size distributions. Passive Cavity Aerosol Spectrometer Probe (PCASP) was also flown, which is an optical probe that measures aerosol size distribution in sizes between 0.1 and 3 μm. Aerodyne Aerosol Mass Spectrometer (AMS) measure mass concentration of sulfate, nitrite, ammonium and organics in particles less than 1 μm [13, 78]. Concurrently, aerosol bulk ionic composition and soluble organic composition were measured with a modified Particle-into-Liquid Sampler PILS [153], in which samples are obtained every 2-3 min to vials held on a rotating carousel and analyzed post-flight. An added advantage of using this approach (US and online detection) is the sampling rate is not limited by the duty cycle time of on-line detectors [153].

Cloud droplet size distributions were measured at 1-Hz ($\sim$50m) resolution using the Cloud and Aerosol Spectrometer (CAS) optical probe onboard the Cloud, Aerosol, and Precipitation Spectrometer (CAPS) integrated spectrometer system [16]. The CAS measures droplet diameters from 0.5 to 50 μm in 20 size bins using a forward scattering principle similar to that of the Forward Scattering Spectrometer Probe (FSSP). Coincidence errors involved in CAPS was reduced in frequency by reducing the viewing volume which is estimated to be accurate within 15% [51]. Droplet concentrations were also measured by using FSSP [31, 77]. Uncertainty of spectra measurements with FSSPs is subject to the nonuniformity of light intensity in the laser beam, variations of the size calibration, the sampling section of the instrument, and

the coincidence effects in the sampling volume [35]. Cloud droplet concentrations are underestimated by 1% at 800 cm^{-3} and 10% at 7000 cm^{-3} due to coincidence errors. Cloud liquid water content was measured with a particle volume monitor (PVM-100) which sums up optically scatted light by droplets passing through its active volume. The variability of measured LWC is associated with natural LWC variability in clouds and also sampling errors due to limited sampling volume of PVM [61]. Updraft velocity was obtained by combined instruments including a five-hole gust probe on the nose of the aircraft, a Pitot-static pressure tube, a Coarse/Acquistion Code-Micro-Electro-Mechanical Systems (MEMS) Integrated GPS/INS Tactical System (C-MIGITS), GPS/inertial navigation system (INS), and the Novatel GPS system.

Table 1: Measured aerosol and cloud properties and instruments.

Measurement	Instrument	Measured properties	Measurement principle
Particle number concentration	Condensation Particle Counter (TSI CPC 3010)	$D_p > 0.01$ μm	varying supersaturations of butanol
Particle number concentration (including ultrafine)	Ultrafine Condensation Particle Counter (TSI CPC 3025)	$D_p > 3$ nm	varying supersaturations of butanol
Aerosol size distribution at dry and humid conditions	Scanning differential mobility analyzer (Dual Automated Classified Aerosol Detector - DACAD)	0.01 – 0.7 μm	electrostatic classification; dry and ambient humidity

Continued on next page

Table 1 – continued from previous page

Measurement	Instrument	Measured properties	Measurement principle
Aerosol size distribution	Passive Cavity Aerosol Spectrometer Probe (PCASP)	0.1 – 3.0 μm	optical scattering
Cloud and drizzle drop size distribution	Cloud, Aerosol, and Precipitation Spectrometer (CAPS)	0.5 – 50 μm (scatter), 25 – 1600 μm (2-D)	optical forward scattering and two-dimensional imaging
Cloud droplet size distribution	Forward Scattering Spectrometer Probe (FSSP)	0.5 – 47.0 μm	optical forward scattering
Cloud droplet liquid water content	Light diffraction (Gerber PVM-100 probe)	$\sim 3 - 50\mu$m	optical scattering
Aerosol bulk ionic composition & soluble organic composition	Particle-into-Liquid Sampler (PILS)	$< 1\mu$m Mass concentration: SO_4^{2-}, NH_4^+, NO_3^-, oxalate	Ion chromatography
Aerosol bulk composition (non-refractory species)	Aerodyne Time-of-Flight Aerosol Mass Spectrometer (TOF-AMS)	0.04 – 1 μm Mass concentration: SO_4^{2-}, NH_4^+, NO_3^-, OC	Flash ionization; quadrapole mass spectrometer

Continued on next page

Table 1 – continued from previous page

Measurement	Instrument	Measured properties	Measurement principle
Updraft velocity and wind speed	five-hole turbulence probe, C-MIGITS inertial navigation system, and Novatel GPS	wind velocity; aircraft position and altitude	wind velocity = aircraft ground velocity (C-MIGITS INS/GPS) - aircraft air velocity (turbulence and Pitot-static probes)

2.3.2 Cloud parcel model

[121, 119, 120, 14] numerical parcel model simulates cloud formation process with a comprehensive treatment of aerosol characteristics, a prescribed updraft velocity and ambient thermodynamic properties and entrainment. The model explicitly computes growth of droplet population by condensation of water vapor within a rising Lagrangian air parcel. The predicted CDNC by the model was successfully evaluated for closure studies during CRYSTAL-FACE [46], CSTRIPE [118], and ICARTT [60]. Determination of CDNC is affected by kinetic limitation effect [79, 43, 121], the chemical effects such as the presence of surfactant [151, 53], partial solubility or film-forming compounds [54, 119, 138, 95], and size-resolved composition effect [115], all of which can be easily considered in the model. The sensitivity analysis of the latter on droplet closure will be addressed.

2.3.3 Cloud activation parameterization

The [58] cloud activation parameterization evaluated in this study is based on the population splitting concept of [122] applied to a lognormal representation of the aerosol size distribution. The parameterization computes droplet population growth

without substantial computational requirements and can comprehensively account for chemical effects on cloud droplet formation such as surface tension depression, partial solubility, water uptake decrease within externally-mixed aerosol populations. Its robustness has been evaluated with numerical parcel model for a wide range of cloud formations conditions [122, 58] and with in-situ observation data for cumuliform and stratiform clouds [46, 118] and highly polluted cloudy air masses [60].

2.4 Observation datasets

The data used in this study was collected onboard the CIRPAS Twin Otter which sampled stratocumulus clouds off the coast of Monterey, California during the summer of 2005. Contrasting the microphysical differences between polluted and clean air masses within the same cloud is a unique feature of stratocumulus clouds with embedded shiptracks. The MASE dataset is largely composed of such cases.

2.4.1 Description of research flights

A total of 13 research flights were conducted during July 2-17, 2005, in which five flights focused on ship tracks are analyzed in this study. Aerosol emissions from ships are incorporated overlying clouds and cause modification in cloud properties seen as striped clouds in satellite images are known as ship tracks. Research flight 3 (RF3) sampled aerosol and cloud properties approximately 50 miles away from the coast. Background and peak aerosol number concentration is 180 and 840 cm^{-3}, respectively. Figure 9 shows a wide uniform stratocumulus clouds seen in satellite images from the Geostationary Operational Environmental Satellite (GOES) visible channel; the cloud deck is very uniform and well-developed. Backward Lagrangian trajectories analyses computed from the NOAA-HYSPLIT model (http://www.arl.noaa.gov/ready/hysplit4.html) suggest that air masses came from the north (Figure 10). The source of air masses in RF6 was from the west north (Figure 10) and its measured maximum aerosol concentration is 1280 cm^{-3}, observed in 39 miles off the coast. During RF10, background

Table 2: General flight information.

Flight number	Flight date	Background N_a (cm^{-3})	Peak N_a (cm^{-3})	Distance off the coast (miles)	Wind direction
RF3	5, Jul	180	840	50	NW-N
RF6	9, Jul	280	1280	39	NW
RF9	13, Jul	220	1280	28	NW-N
RF10	14, Jul	600	2270	28	N
RF13	17, Jul	600	2770	39	NW-N

(peak) aerosol concentration was 600 (2270) cm^{-3}. Measurements were taken 39 miles off the coast and aerosol concentration is 600 cm^{-3} in clean condition and 2770 cm^{-3} as region was perturbed by ship emissions. In analyzed flights, 13 clouds are selected and summary of their characteristics is in Table 2.

2.4.2 Cloud droplet number and updraft velocity

Data for cloud droplet number closure study are carefully screened to eliminate CDNC bias influenced by entrainment mixing and precipitation scavenging. Integrated CDNC from FSSP and cloud liquid water content (LWC) measured by Gerber PVM-100 probe are first used to identity time stamps of flight legs which passed through clouds (characterized by a simultaneous increase in CDNC and LWC). An average value of droplet concentrations is then obtained for each in-cloud leg. Temporal length taken in average is determined by time series of measured Gerber PVM-100 LWC. A substantial variability in CDNC reveals inherent bumpiness and randomness in cloud nature. Low CDNC observed during in-cloud flights were possibly associated with "holes" existed among these wide spread stratocumulus clouds measured during MASE. Summary of the averaged observed cloud drop concentrations for each cloud is presented in Table 3. For all analyzed transects, 63 % of cases that cloud droplet number concentration is greater than 200 cm^{-3} and 76 % for 150 cm^{-3}. Compared

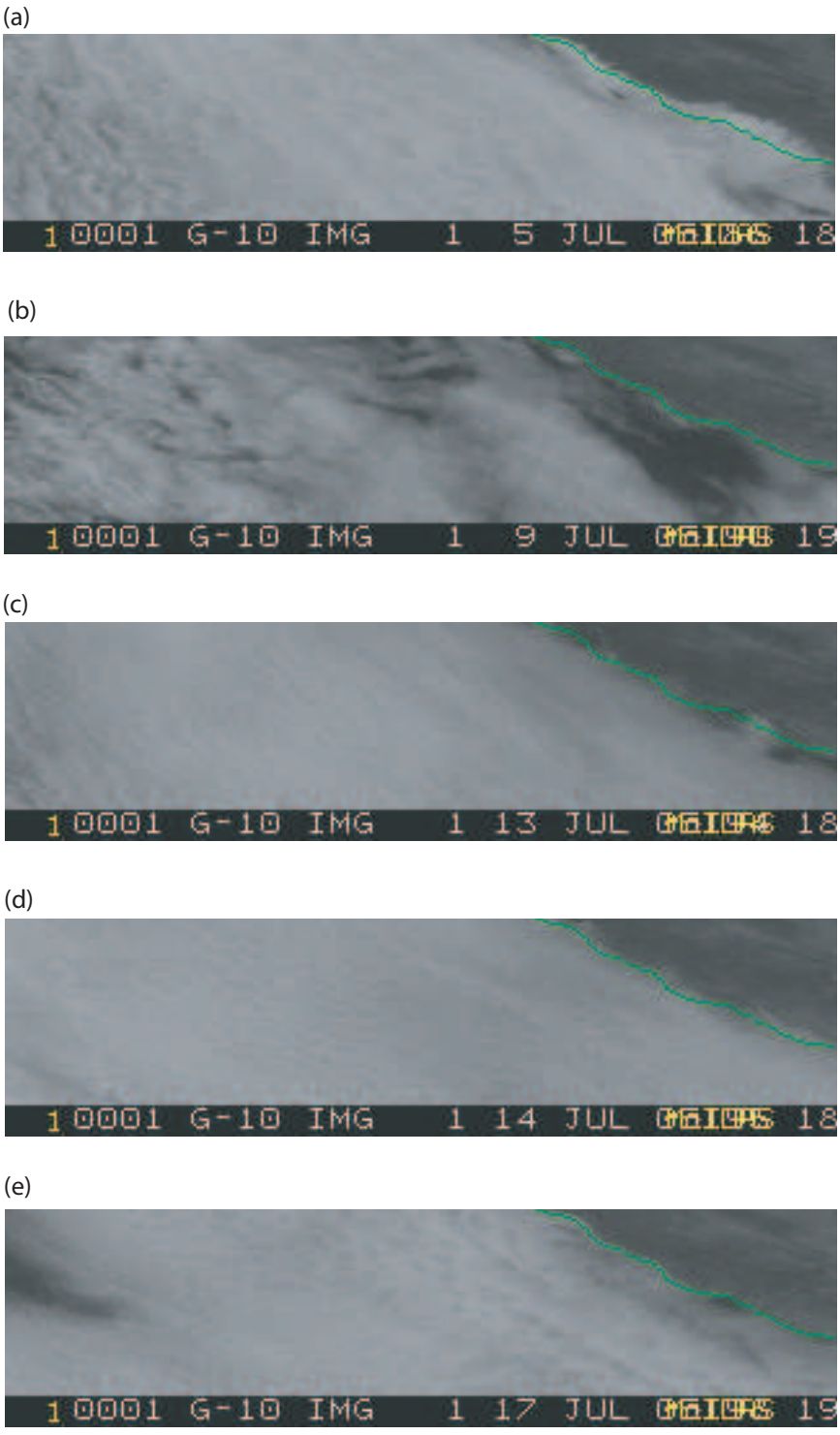

Figure 9: GOES-10 band 1 (centered at 0.65 m) satellite images on (a) 18:00 UTC Jul,5 (b) 19:30 UTC Jul,9 (c) 18:00 UTC Jul,13 (d) 18:30 UTC Jul,14 (e) 19:00 UTC Jul,17, 2005. GOES images are obtained from NOAA Satellite and Information Service (http://www.class.noaa.gov/saa/products/welcome).

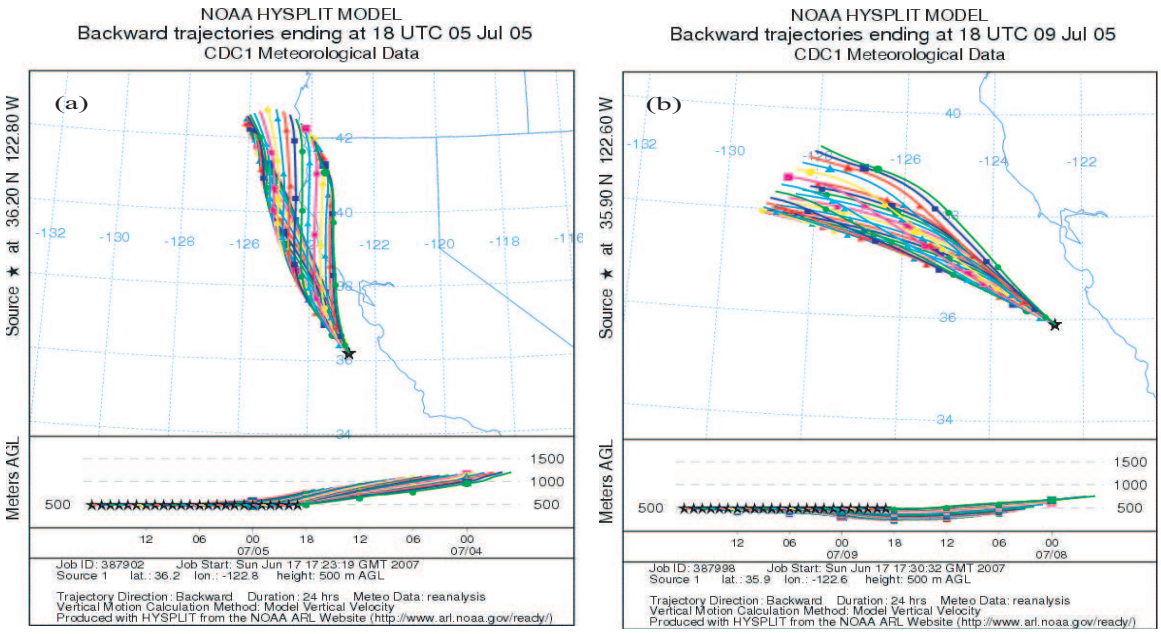

Figure 10: HYSPLIT backward trajectory analysis for (a) research flight RF3 and (b) research flight RF6.

to cumulus clouds in CRYSTAL-FACE campaign [118], updraft velocities sampled during MASE are relatively smaller varying from 0.10 to 0.47 ms^{-1}, (standard deviation ranges from 0.08 to 0.34 ms^{-1}). Most of clouds, observed CDNC was positively correlated with average updraft velocity. However, relative high CDNC (> 210 cm^{-3}) was observed in some of the transects for RF9 (1), and transect 3 of RF13 (4) in which relative weak updraft velocities were detected (<0.15 ms^{-1}). The relative importance of dynamical factors, chemical effects, kinetic limitation and aerosol size distribution on droplet number is studied in the following sections. The correlation analysis of CDNC with key influential factors contributing activation events are examined in section 2.4.7.

2.4.3 Aerosol size distribution and chemical composition

After the time stamps for clouds are determined, aerosol size distributions measured by DMA are taken within under-cloud passes prior or immediately after to cloud penetrations [60]. Aerosol size distributions used as inputs to the parcel model are

Table 3: Cloud characteristics in analyzed clouds during MASE. N_d is in cm^{-3}

Flight number (Cloud)	Transect	w (ms^{-1})	s (ms^{-1})	Observed N_d	Predicted N_d	
					Parcel model	Parameterization
RF3 (1)	1	0.466	0.336	125.31	246.91	269.76
RF3 (1)	2	0.266	0.252	101.31	218.67	230.07
RF3 (1)	3	0.336	0.296	219.85	227.29	248.92
RF3 (1)	4	0.267	0.245	230.74	218.67	236.07
RF3 (1)	5	0.275	0.254	231.20	218.67	238.35
RF3 (2)	1	0.163	0.126	112.17	209.57	224.82
RF3 (2)	2	0.150	0.125	131.11	207.25	222.56
RF3 (2)	3	0.163	0.116	224.69	209.57	224.89
RF3 (2)	4	0.238	0.155	214.47	236.78	252.56
RF3 (2)	5	0.185	0.135	136.37	220.21	243.70
RF6 (1)	1	0.152	0.122	91.00	63.78	42.34
RF6 (2)	1	0.128	0.092	92.74	70.67	65.86
RF6 (3)	1	0.203	0.189	106.30	87.38	73.08
RF9 (1)	1	0.220	0.168	262.52	351.85	344.91
RF9 (1)	2	0.161	0.139	200.90	301.15	297.13
RF9 (1)	3	0.138	0.092	220.99	279.12	276.72
RF9 (1)	4	0.125	0.087	228.49	262.11	262.49
RF9 (1)	5	0.101	0.077	242.94	222.57	235.51
RF9 (1)	6	0.149	0.109	195.94	281.74	288.95
RF9 (1)	7	0.155	0.109	208.19	297.85	295.31
RF9 (1)	8	0.169	0.134	214.95	301.15	304.86
RF9 (1)	9	0.153	0.092	234.52	281.74	294.04
RF9 (2)	1	0.159	0.121	210.33	148.62	145.44
RF9 (2)	2	0.216	0.140	180.13	185.96	179.49
RF10 (1)	1	0.157	0.136	192.37	293.07	314.11
RF10 (1)	2	0.155	0.122	228.57	293.07	309.54
RF10 (1)	3	0.184	0.116	253.65	319.61	341.13
RF10 (1)	4	0.151	0.110	238.82	281.33	306.37
RF10 (2)	1	0.154	0.121	148.58	241.87	247.83
RF10 (2)	2	0.206	0.153	262.52	267.06	274.73
RF10 (2)	3	0.162	0.108	215.52	251.11	252.39
RF13 (1)	1	0.207	0.167	208.29	323.64	296.66
RF13 (2)	1	0.219	0.170	271.97	192.36	232.79
RF13 (3)	1	0.195	0.151	194.09	171.27	180.49
RF13 (3)	2	0.177	0.131	274.69	158.95	172.27
RF13 (4)	1	0.212	0.164	156.54	257.20	284.13
RF13 (4)	2	0.216	0.164	301.23	257.20	285.43
RF13 (4)	3	0.124	0.110	211.76	188.98	219.49

averaged in at least four DMA scans, corresponding to the time requirement for one chemical composition measurement with the PILS; lognormal aerosol distributions are fitted to the DMA by least-square minimization. In this study, three lognormal modes are used to describe the aerosol size distributions; detailed characteristics for all aerosol and clouds analyzed is summarized in Table 4. Chemical characteristics of aerosol populations are analyzed using PILS data based on mass balance among solutes and are summarized in Table 5. The ammonium-sulfate molar ratio obtained by the PILS was less than 2 for most of the clouds except RF6 (1) where the ratio is 7.58, indicated aerosols was neutralized in this case. Any gas-phase ammonia would quickly condense and neutralize acidic particles such as sulfate and nitrite formed from in-cloud aqueous processes. The presence of nitrate in this case confirms the conclusion of neutralization condition in aerosol composition. Heterogenesity in aerosol acidity was also seen in PILS measurement, the fluctuations can be large even in the same flight (RF6). Among 13 clouds profiled, 8 of them are identified as "sulfate rich" conditions (i.e., the ammonia to sulfate ratio was less than unity). Detection of acidity changes over the aerosol distribution was inhibited due to lack of size-resolved composition. A small amount of oxalate was seen from the PILS analysis which was generated by in-cloud oxidation of organic precursors. In this study, oxalate was assumed to behave like sulfate thus its contribution of solutes was included into total sulfate. The aerosol soluble fraction is then determined by subtracting the dry volume of aerosol (from the PILS loadings) from the integrated DMA size distributions [60]; using this approach, the soluble fraction was unity for all aerosol.

Table 4: Aerosol characteristics during MASE clouds analyzed in this study.

Flight Number	Mode	D_p (μm)	σ (μm)	N (cm^{-3})

Continued on next page

Table 4 – continued from previous page

Flight Number	Mode	D_p (μm)	σ (μm)	N (cm^{-3})
RF3	Nucleation	0.019	1.081	14
Cloud 1	Accumulation	0.052	1.591	232
	Coarse	0.162	1.487	204
RF3	Nucleation	0.016	1.199	6
Cloud 2	Accumulation	0.061	1.625	143
	Coarse	0.172	1.541	250
RF6	Nucleation	0.019	1.201	20
Cloud 1	Accumulation	0.042	1.350	228
	Coarse	0.124	1.270	8
RF6	Nucleation	0.020	1.022	5
Cloud 2	Accumulation	0.041	1.430	227
	Coarse	0.158	1.439	53
RF6	Nucleation	0.020	1.089	13
Cloud 3	Accumulation	0.039	1.434	305
	Coarse	0.134	1.407	34
RF9	Nucleation	0.014	1.014	10
Cloud 1	Accumulation	0.059	1.458	444
	Coarse	0.146	1.414	399
RF9	Nucleation	0.019	1.050	12
Cloud 2	Accumulation	0.059	1.439	655
	Coarse	0.154	1.493	374
RF10	Nucleation	0.019	1.130	13
Cloud 1	Accumulation	0.054	1.515	637
	Coarse	0.143	1.395	337

Continued on next page

Table 4 – continued from previous page

Flight Number	Mode	D_p (μm)	σ (μm)	N (cm^{-3})
RF10	Nucleation	0.018	1.014	8
Cloud 2	Accumulation	0.053	1.463	460
	Coarse	0.151	1.422	291
RF13	Nucleation	0.013	1.014	14
Cloud 1	Accumulation	0.060	1.400	529
	Coarse	0.139	1.438	198
RF13	Nucleation	0.012	1.013	14
Cloud 2	Accumulation	0.059	1.448	665
	Coarse	0.149	1.514	304
RF13	Nucleation	0.015	1.025	13
Cloud 3	Accumulation	0.069	1.406	689
	Coarse	0.123	1.328	335
RF13	Nucleation	0.016	1.258	342
Cloud 4	Accumulation	0.051	1.662	581
	Coarse	0.142	1.497	156

2.4.4 Growth factor

In this study, we also compute growth factor of a particle, f(RH), defined as the ratio of the equilibrium wet diameter at specified relative humidity (RH) to its dry diameter. The mass of a wet aerosol is defined as

$$m_{wet} = \frac{\pi}{6} D_{pwet}^3 \rho_{wet} \tag{43}$$

and the dry aerosol mass

$$m_{dry} = \frac{\pi}{6} D_{pdry}^3 \rho_{dry} \tag{44}$$

Thus combining Equation (43) and Equation (44) gives the growth factor which can expressed as

$$f(RH) = (\frac{m_{wet}}{m_{dry}} \times \frac{\rho_{dry}}{\rho_{wet}})^{1/3} \tag{45}$$

where ρ_{wet}, ρ_{dry} is the density of wet, dry aerosol. The wet aerosol density is the average density of aerosol which is computed as

$$\rho_{wet} = \epsilon_{H2O} \times \rho_{H2O} + \epsilon_s \times \rho_s \tag{46}$$

ϵ_{H2O} and ϵ_s is the volume fraction of water and solute, respectively. We also compare the measured growth factor based on dry and wet DMA instrument with predicted values from thermodynamical equilibrium model ISORROPIA [59]. Implicit in the growth factor calculation is the assumption that the aerosol particles are internally mixed with regard to its hygroscopic properties and dried particles are compact spheres.

Chemical composition was obtained from PILS measurement and summary of average characteristics analyses of each flight are presented in Table 6, which also include calculated measured and predicted growth factor.

The measured growth factor is computed by ratio of the modal diameter of wet DMA to dry DMA data. The modal diameter is where the highest number concentration observed. Figure 11 shows the predicted and measured growth factor for cases considered in this study. Most uncertainty of predicted growth factor is associated with the RH fluctuations in DMA instrument and other errors such as a simplified Köhler equation applied to diluted solution in equilibrium vapor pressure calculation. Thus we did simulations of varying RH with 2 standard deviation to see its caused errors which is also shown in Figure 11. Overall, the errors in growth factor due to RH fluctuations is with 0.1 except one case. For the growth factor calculation, we use bulk chemistry properties of particles to compute their wet equilibrium sizes; however, size-varying chemical composition may cause varying growth characteristic

Table 5: Thermophysical properties and chemical composition for analyzed clouds.

Flight number (Cloud)	Soluble mass fraction	Stoichiometry Na	NH_4	NO_3	Cl	SO_4	HSO_4
RF3 (1)	0.52	0.17	0.53	0.00	0.17	0.00	0.83
RF3 (2)	0.45	0.13	0.72	0.00	0.13	0.05	0.82
RF6 (1)	1.00	0.08	1.58	0.26	0.08	0.66	0.00
RF6 (2)	1.00	0.21	1.35	0.00	0.21	0.56	0.23
RF6 (3)	1.00	0.10	1.38	0.02	0.10	0.49	0.40
RF9 (1)	0.47	0.00	1.36	0.00	0.00	0.41	0.59
RF9 (2)	0.51	0.00	1.62	0.00	0.00	0.62	0.38
RF10 (1)	0.62	0.30	0.45	0.00	0.30	0.06	0.64
RF10 (2)	0.45	0.47	0.44	0.00	0.47	0.00	0.53
RF13 (1)	0.30	0.05	0.74	0.00	0.05	0.09	0.85
RF13 (2)	0.43	0.00	0.39	0.00	0.00	0.00	1.00
RF13 (3)	0.32	0.17	0.83	0.00	0.17	0.00	0.83
RF13 (4)	0.79	0.00	1.00	0.00	0.00	0.00	1.00

and result in different growth factor. Growth factor was obtained from 1.12 to 1.69 based on DMA data and growth factor range is reduced to 1.20 to 1.59 obtained from ISORROPIA.

2.4.5 Cloud droplet closure

The prediction of cloud droplet number was given by detailed numerical parcel model [121] and activation parameterization [122, 58] with inputs of the dynamics, aerosol microphysics and ambient thermodynamic properties of aerosol for each flight and cloud presented in Table 4, 5. Updraft velocity variability is quantified by the standard deviation and their dependence with updraft velocity is shown in Figure 12. Overall, for clouds analyzed in this study, the fluctuations of vertical velocity is comparable to measured updrafts and similar results were obtained for stratocumulus clouds sampled during the CSTRIPE campaign [118]. The observed updraft perturbations may add uncertainty of CDNC prediction through the mechanism called in-cloud nucleation, predominantly for the low updrafts resides in the lower and intermediate levels of clouds [52]. To avoid this, we principally focus on in-cloud legs

Table 6: Thermodynamical properties and growth factor for clouds analyzed in this study

Flight number (Cloud)	Ave. M_s (kg)	Ave. ρ (kg m^{-3})	Temp. (K)	Van't Hoff factor	Measured GF_{modal}	Measured GF_{Dpavg}	Predicted GF
RF3 (1)	0.100	1829.66	293.25	2.83	1.49	1.20	1.35
RF3 (2)	0.105	1812.65	291.91	2.87	1.69	1.15	1.34
RF6 (1)	0.111	1692.29	293.53	2.66	1.28	1.25	1.08
RF6 (2)	0.113	1800.48	292.73	2.79	1.26	1.25	1.23
RF6 (3)	0.117	1784.51	286.09	2.88	1.49	1.36	1.32
RF9 (1)	0.121	1773.22	292.06	3.00	1.35	1.18	1.25
RF9 (2)	0.125	1738.95	291.93	3.00	1.23	1.21	1.25
RF10 (1)	0.094	1859.41	293.42	2.70	1.68	1.21	1.25
RF10 (2)	0.087	1890.32	291.01	2.53	1.28	1.26	1.34
RF13 (1)	0.108	1803.10	295.92	2.95	1.23	1.24	1.34
RF13 (2)	0.105	1814.02	294.29	3.00	1.45	1.37	1.30
RF13 (3)	0.106	1809.37	285.74	2.83	1.12	1.22	1.36
RF13 (4)	0.115	1780.00	286.01	3.00	1.34	1.28	1.48

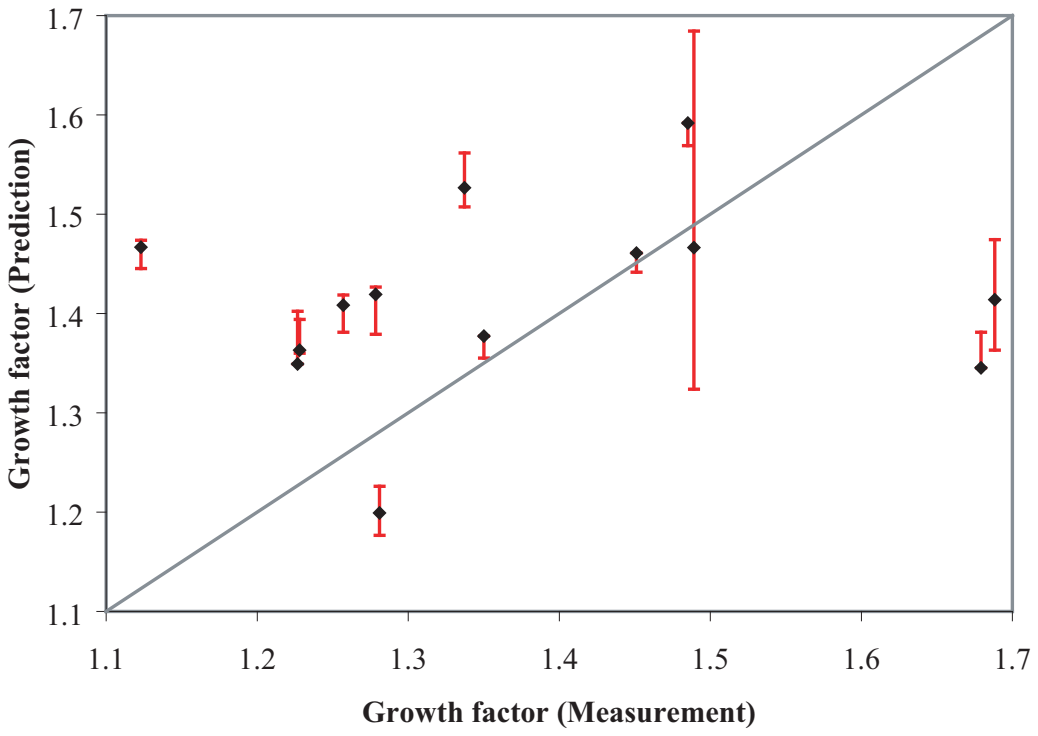

Figure 11: Predicted and measured growth factor.

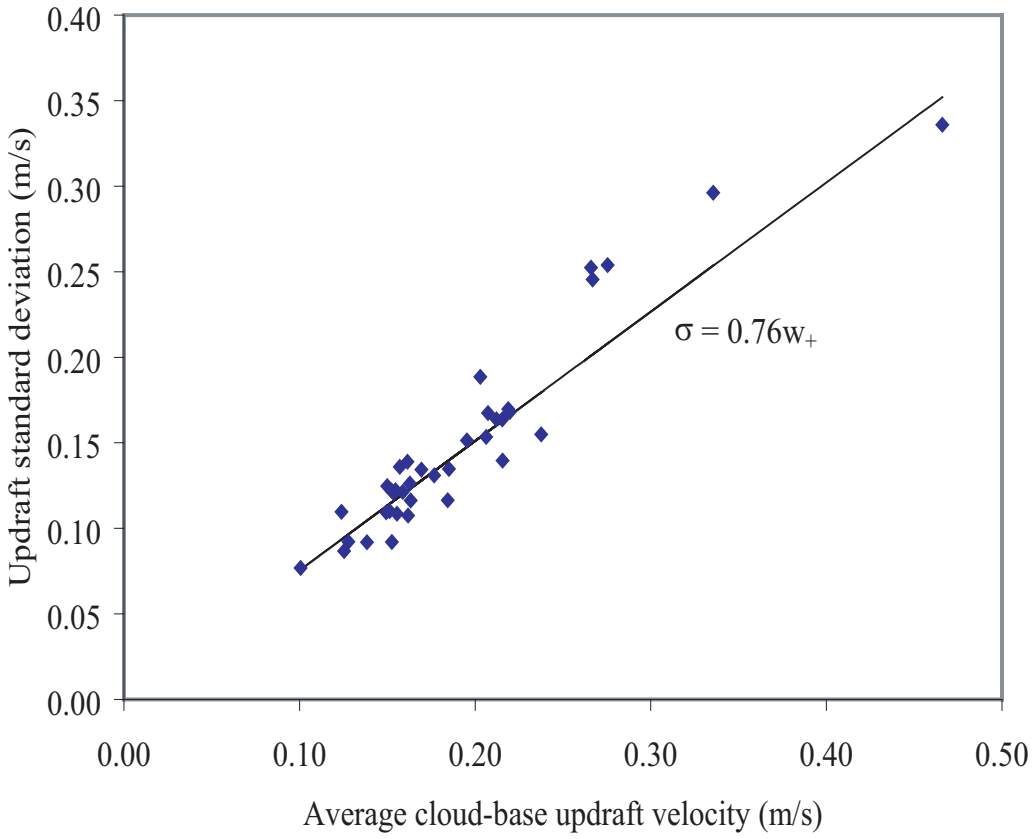

Figure 12: Dependence between average cloud-base updraft velocity and updraft standard deviation.

close to cloud base. Uncertainty of cloud drop number prediction also comes from inhomogeneities in spatial distribution of updraft velocity and the value of updraft velocity taken in the simulation is unlikely to be the same as the updraft velocity at which N was defined. The average updraft velocity, w_+, is used to compute N as taken by [118] and which gives best closure for cumulus and stratocumulus clouds.

A Gaussian probability density function (pdf), $f(w)$, of vertical velocity with zero average and standard deviation σ_w, is commonly used to represent vertical velocity distributions in developed stratocumulus clouds. The average updraft $\bar{w}$, $\int_0^\infty wf(w)dw / \int_0^\infty f(w)dw$, and its relationship to σ_w can be expressed as $\bar{w} = \left(\frac{2}{\pi}\right)^{1/2} \sigma_w \cong 0.8\sigma_w$ [60]. This theoretically-derived factor 0.8 between $\bar{w}$ and σ_w is also consistent

with finding of [125], in which a "characteristic" velocity (0.8 times the standard deviation of the vertical velocity distribution) gave the optimum closure. Considering only positive values of vertical velocity responsible for activation events [118], we use a half-normal distribution (a normal distribution with mean 0 and parameter θ limited to domain $x \in [0,\infty)$) to represent updraft distributions. The pdf of updraft velocity with parameter θ is expressed as $p(w) = \frac{2\theta}{\pi} \exp\left\{-\frac{w^2\theta^2}{\pi}\right\}$, and the average updraft, w_+, is computed as,

$$w_+ = \int_0^\infty w p(w) dw = \int_0^\infty w \frac{2\theta}{\pi} \exp\left\{-\frac{w^2\theta^2}{\pi}\right\} dw = \frac{1}{\theta} \tag{47}$$

Note the physical meaning of w_+ is identical to average updraft $\overline{w}$ integrated on the right distribution of Gaussian pdf thus $\overline{w} = w_+$. The standard deviation of a half-normal distribution can also be derived analytically:

$$\sigma_+ = \sqrt{\frac{\pi - 2}{2}} \frac{1}{\theta} \tag{48}$$

with $w_+ = \frac{1}{\theta}$, we obtain $\sigma_+ = \sqrt{\frac{\pi-2}{2}} w_+ \cong 0.76 w_+$, which is consistent with [60] and observed dependence of standard deviation and mean updraft velocity(Figure 12).

The under-cloud temperature, pressure and relative humidity describe the pre-cloud thermodynamic sate of the atmosphere and are used as initial conditions for the simulations (Table 6). Fitted lognormal aerosol size distribution and thermophysical and stoichiometry information used are listed in Table 4 and 5. It is assumed that the aerosol is internally mixed and major compositions are ammonium sulfate, ammonium bisulfate, ammonium nitrite and sodium chloride. The insoluble volume fraction was inferred by subtracting the total soluble volume (obtained from the PILS measurements) from the total aerosol volume (obtained from size distribution measurements). It was found (Table 5) the aerosols were predominantly composed of soluble salts and the mass fraction of the soluble was 1 in clouds analyzed in this study. It is assumed uniform composition with size; this can introduce a significant

amount of uncertainty in predicting CCN concentrations (e.g., [115, 34]. The importance of the size uniform composition in cloud droplet number prediction is discussed in section 2.4.7.

The mass water vapor accommodation coefficient, a_c, used for computing the water vapor mass transfer coefficient [58] is currently subject to significant uncertainty. Laboratory studies have found value of a_c ranging from 0.01 to 0.3 and their magnitudes depend on droplet characteristics. a_c of pure water droplets vary from 0.1 – 0.3, and from 0.04 – 0.06 for aged atmospheric CCN [149, 42, 46] . For dilution droplets and pure water, consistent with existing lab studies, a higher a_c of unity was also suggested by [92]. Ambient CCN measurements show the presence of electrolytes and potentially organic surfactants in concentrated solutions can induce other kinetic processes (e.g., solute dissociation, [10]), which can slow water uptake and droplet growth, as a result, giving an uptake coefficient is much less than 1. The droplet evaluation was sensitive to condensation coefficient used in the simulation; in study of [60] showed the assumption of condensation coefficient used in parcel model contribute one of the greatest uncertainties in N_d prediction. Considering the wide range of a_c, a series of sensitivity analysis of a_c for N_d prediction is investigated and details are in section 2.4.7. We found the optimum value of a_c, obtained from the least average droplet number error for analyzed 13 clouds during MASE, being 0.1 and is used for the droplet number closure simulation.

Figure 13 shows the cloud droplet number closure for all transects of 13 clouds analyzed in this study using the detained parcel model and the modified NS parameterization. The predictions of $N_d$are close to 1:1 line indicate excellent agreement with observations. On average, the modified NS parameterization was found to reproduce observed N_d with the same accuracy as the parcel model. This remarkable performance was evidenced by no systematic bias between the modeled and the observed N_d. In most cases, predictions are within 25% of the observations, the normalized

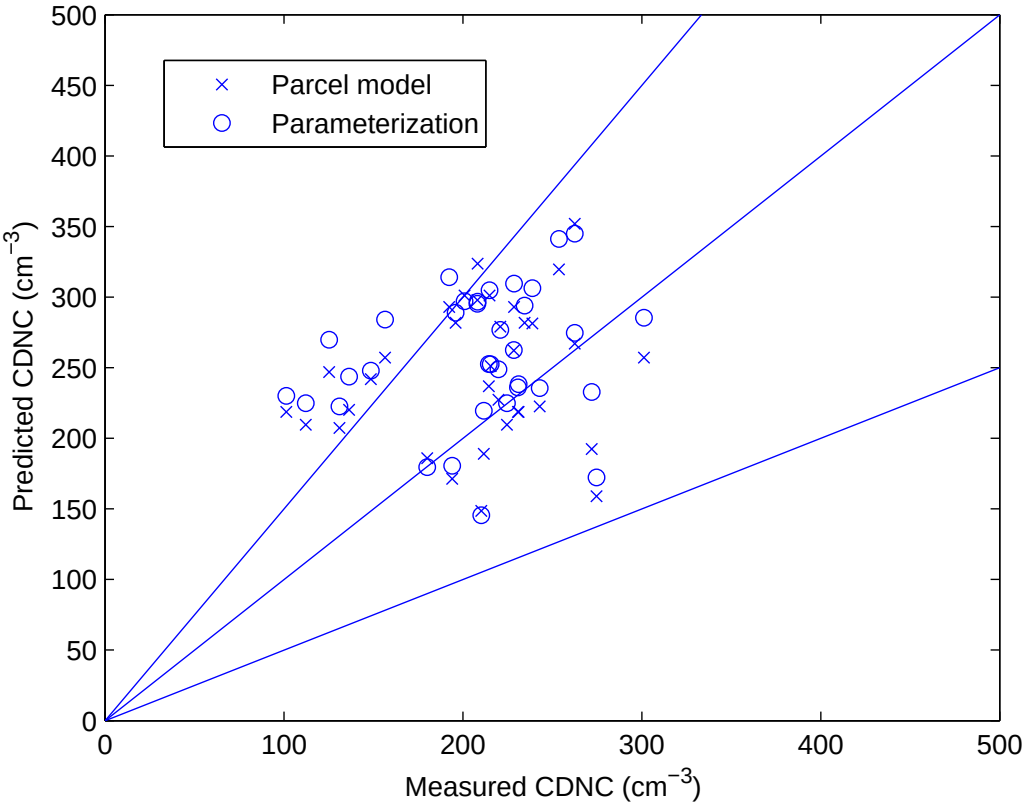

Figure 13: Cloud droplet number closure using parcel model and parameterization.

mean bias which quantify the average error of N_d prediction are 24.9 ± 37.0 % (parcel model) and 30.9 ± 38.8 % (parameterization). This study, combined with the work of [118, 60] clearly show that the modified NS parameterization can accurately and robustly predict the process of cloud droplet formation and its aptness for GCM studies of the aerosol-cloud interactions.

2.4.6 Effect of averaging period on droplet closure

To study the effect of averaging scale on cloud droplet number closure, we used two additional different time periods for averaging updraft velocity and the measured cloud droplet number. The obtained cloud droplet closure for 20 seconds-averaged and 5 seconds-averaged are shown in Figure 14. For the aircraft speed of 50 m s^{-1}, the spatial domain for 20 seconds and 5 seconds are 1 km and 250 m, respectively. The

Table 7: Normalized mean error and standard deviation of droplet number closure based on transect, 20 seconds and 5 seconds averages for parcel model and parameterization.

		Parcel model	Parameterization
Transect	Mean (%)	24.9	30.9
	Standard deviation (%)	37.0	38.8
20 seconds	Mean (%)	33.1	45.6
	Standard deviation (%)	313.6	362.7
5 seconds	Mean (%)	148.8	174.1
	Standard deviation (%)	1598.3	1788.4

spatial averaging transect for all the analyzed cases ranges from 6 to 44 km, depending on the duration of transect, which is chosen based on cloud droplet number and Gerber liquid water content profiles. The number of closure point increases for smaller time interval and so does the extent for scattering. The average normalized mean error and standard deviation for droplet number evaluation with three averaging intervals are summarized in Table 7. In general, the error based on parcel model is smaller and for parameterization, which is in good agreement with parcel model but tends to give larger biases. The average error obtained from the 20 seconds-averaged for parcel model is 33 %, and is closer to the error based on transect average (25 %). However, the average standard deviation for 20 seconds average is almost an order of magnitude larger than the one based on transect average. A lot of scatter shown in 5 seconds-averaged closure is also reflective on the calculated mean error, which is 149 % and 174 % for parcel model and parameterization.

2.4.7 Sensitivity tests and source of uncertainty

In order to validate if the accuracy of fitted size distributions and its uncertainty in droplet closure, we did analysis of CCN concentration calculations. Based on Köhler theory, the number of CCN is equal to the concentration of particles whose critical supersaturation are less than the maximum supersaturation encountered in a cloud

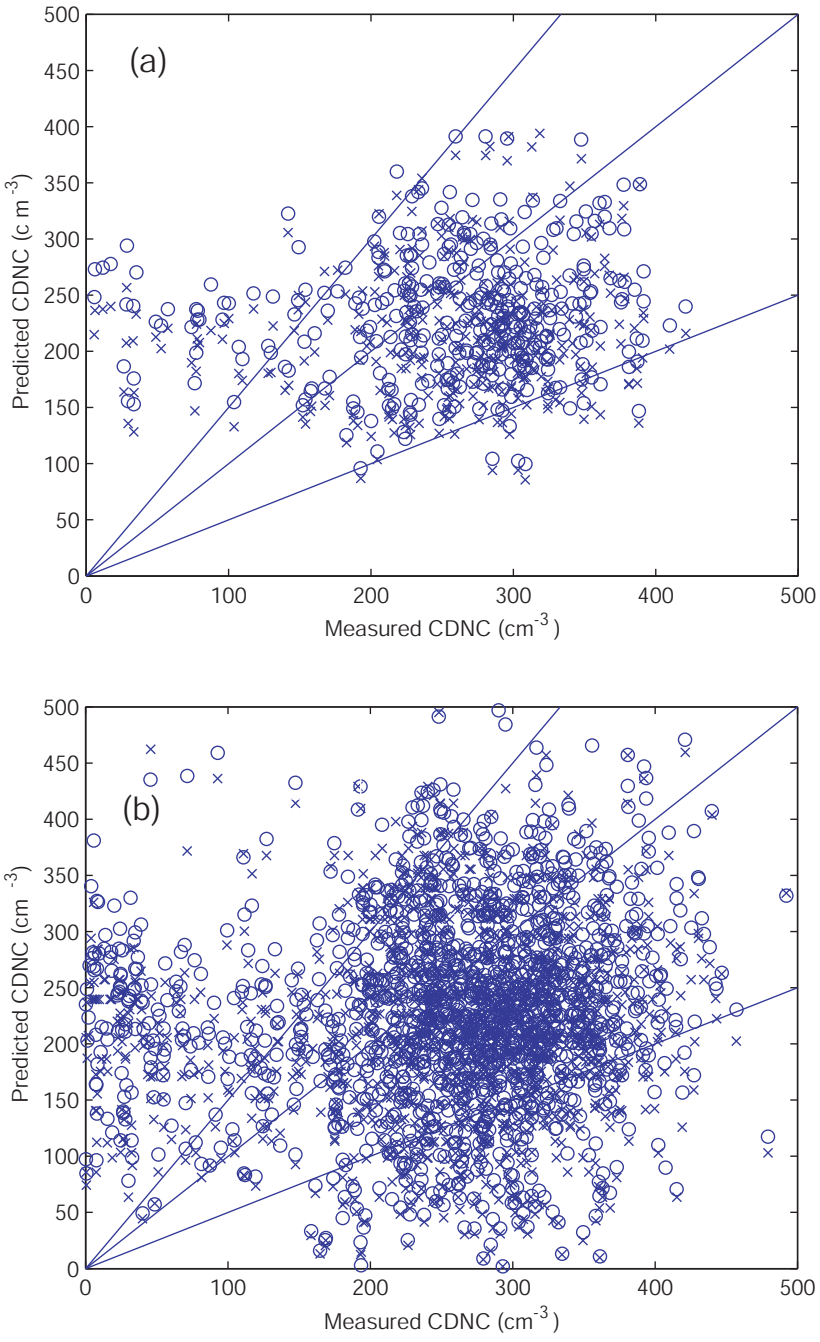

Figure 14: Cloud droplet number closure using parcel model and parameterization. (a) 20 seconds average (b) 5 seconds average. Cross sign is for parcel model and circle is for parameterization.

updraft. The critical supersaturation s_c of a particle can be expressed as [148]

$$s_c = \exp\left(\frac{4A^3}{27B}\right)^{1/2} - 1 \tag{49}$$

with

$$A = \frac{4M_w\sigma_w}{RT\rho_w}, B = \frac{6n_sM_w}{\pi\rho_w} \tag{50}$$

where M_w is the water molar mass, σ_w is the surface tension of water, R is the universal gas constant, T is the temperature, ρ_w is the water density, n_s is the mole of solutes. Similar to approach to derive critical supersaturation, a critical diameter D_{pc} of particle is obtained as $D_{pc} = \left(\frac{3B}{A}\right)^{1/2}$. Thus once the minimum D_{pc} is determined for aerosol spectra with inputs of bulk aerosol chemistry from the PILS measurement, and then integrate number of particles whose diameters are above D_{pc} over the entire aerosol spectra gives CCN number.

In our analysis, we used the maximum supersaturation (s_{max}), predicted from parameterization in which fitted aerosol size distributions and chemical composition from the PILS measurement are used, to compute the number of CCN directly from DMA measurement with known measured aerosol chemical compositions. Figure 15 shows the predicted CCN concentrations from the DMA measured and the fitted aerosol size distributions at the predicted s_{max} obtained from parameterization. Data are close to 1 to 1 line indicates the fitted aerosol size distributions are well represented size distribution characteristics from measurement and does not contribute a high level of the uncertainty in droplet number concentration prediction. We also testify the sensitivity of CCN number calculation to different Van't Hoff factors used; the calculations are tested only for NH_4HSO_4 whose dissociation value is usually between 2 and 3. A higher CCN number is obtained when a higher value is adopted, which is in accord with theory. An explicit consideration of combined Van't Hoff factor from contribution of different aerosol chemical composition for each case is also shown (Figure 15) as a reference to compare with different setting of Van't Hoff factor.

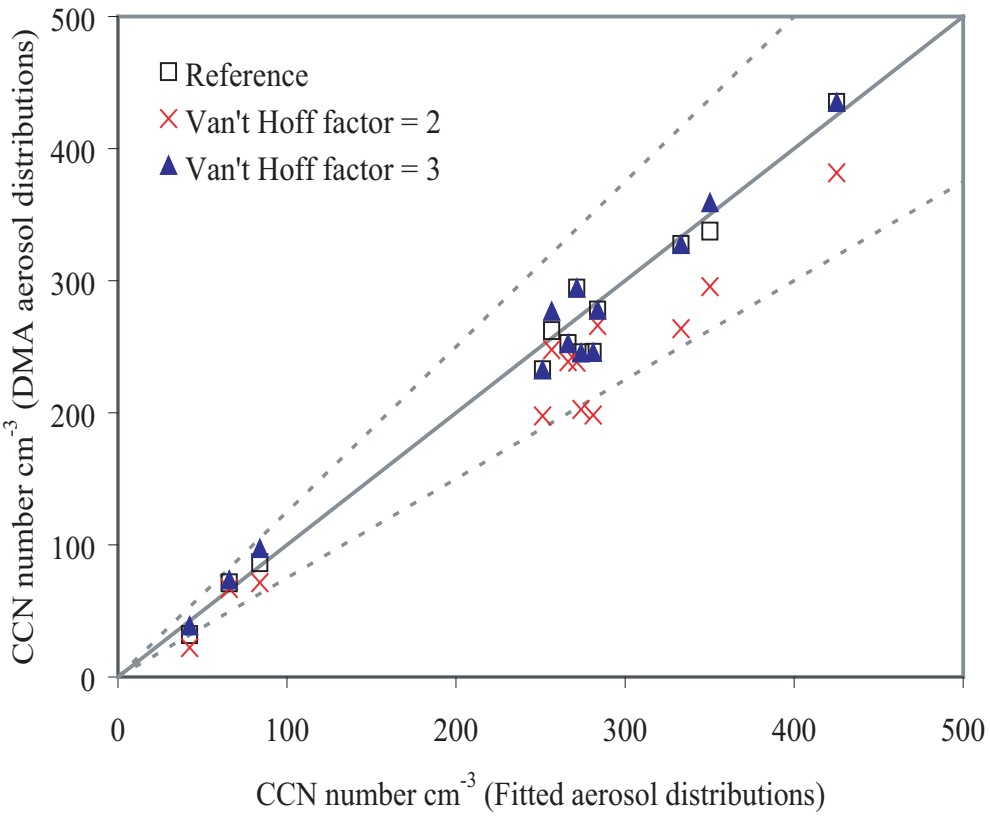

Figure 15: Predicted CCN concentrations from the DMA and the fitted aerosol distributions at the predicted maximum supersaturation.

Overall, the predicted CCN number using the fitted aerosol distributions are within 25% with calculated CCN number directly using DMA size distribution measurements at S_{max} predicted by parameterization. The pertained average CCN error of the fitted aerosol size distribution is 0.68 % and standard deviation is 8.88 %. The aerosol properties and thermal conditions for CCN number calculation in analyzed cases were presented in Table 5.

Sensitivity of water uptake coefficient (α_w) to the droplet number error is shown in Figure 16, the optimal value of α_w is 0.1 for the clouds analyzed in this study. To identify the key influential factors to cloud drop number N, which depends on not only dynamics but also on the aerosol microphysics, we exam the correlation analysis of N with key parameters affecting N, being i) total aerosol number N_a,

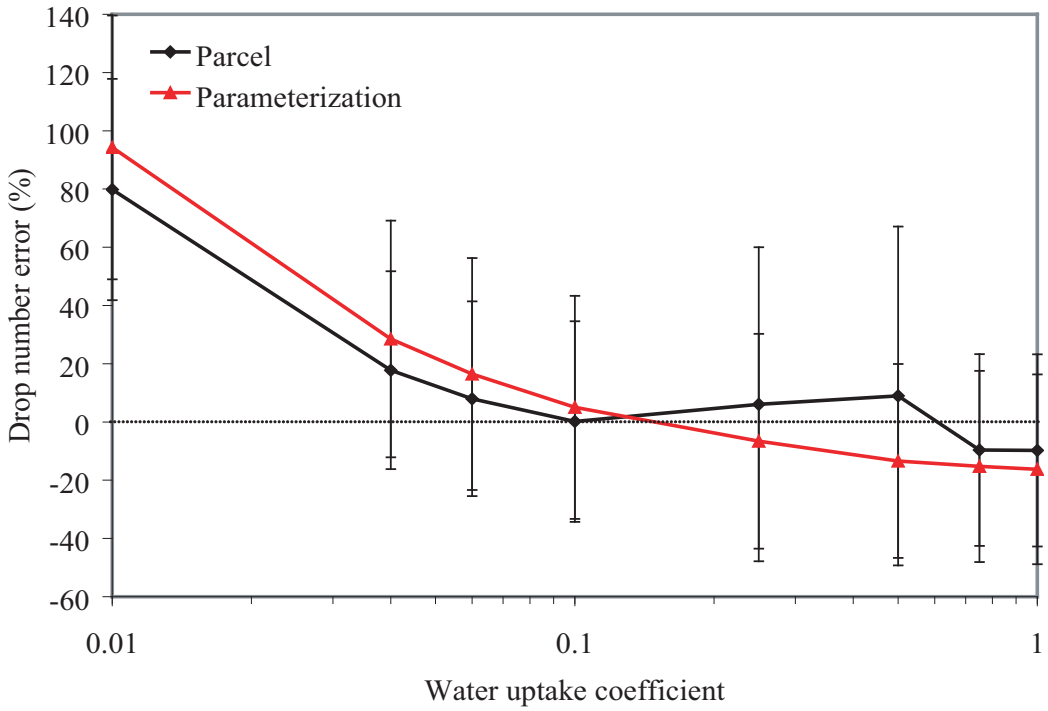

Figure 16: Sensitivity of water uptake coefficient to drop number error (%).

ii) accumulation mode aerosol number, N_{ac}, *iii*) average in-cloud updraft velocity, *iv*) in-cloud updraft velocity variance, and *v*) aerosol sulfate mass fraction, ε_{SO4}, *vi*) aerosol bisulfate mass fraction, ε_{HSO4} and *vii*) aerosol nitrate mass fraction, ε_{NO3}. The correlation analyses are presented in Table 8. N is mainly controlled by the number of aerosol and accumulation mode aerosol number as identified as particles size between 0.1 to 1 μm in diameter measured during MASE. The correlation coefficients of N between N_a and accumulation N_a are 0.76 and 0.61. The correlations are statistically significant as the pertained p-values are less than 0.05, being 0.0025 and 0.026. N is less correlated with the average in-cloud vertical velocity (0.21) and in-cloud updraft velocity variance (0.17), whose magnitude can be similar to in-cloud updraft velocity during MASE (Figure 12).

Droplet closure with size-resolved aerosol composition as compared to size-averaged

Table 8: Correlation of cloud drop number with key factors influencing cloud formation process.

Statistical property	N_a	N_{ac}	w	σ_w	ε_{SO4}	ε_{HSO4}	ε_{NO3}
Correlation coefficient	0.76	0.61	0.21	0.17	-0.79	0.85	-0.55
p-value	0.0025	0.0260	0.4951	0.5776	0.0013	0.0003	0.0522

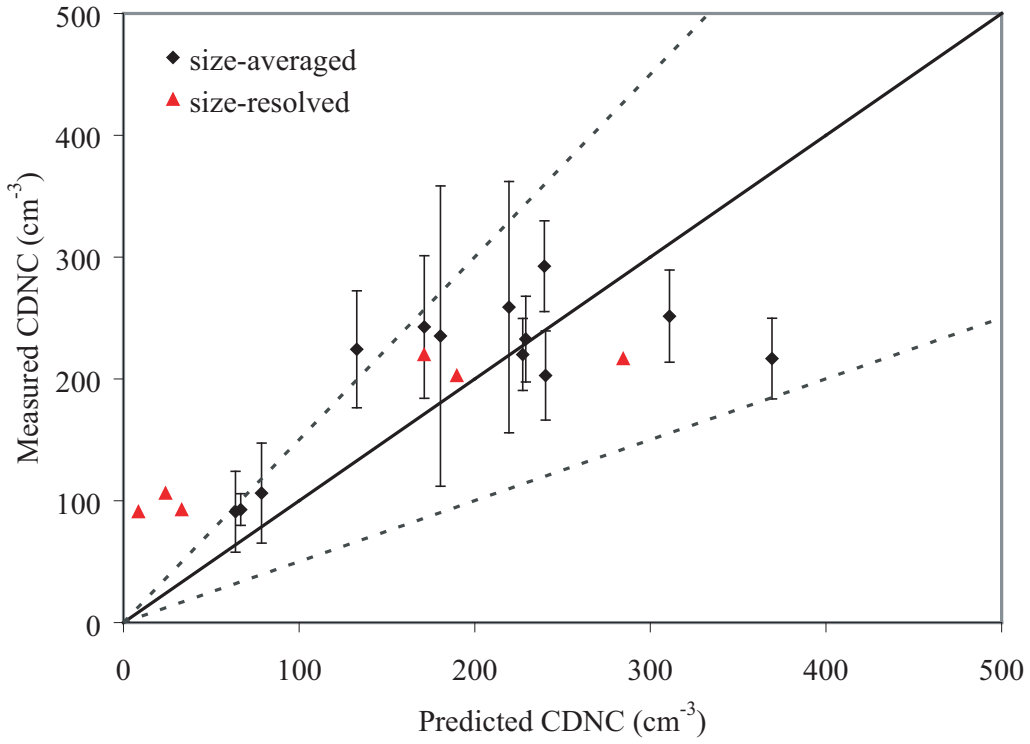

Figure 17: Cloud droplet number closure using size-resolved and size-averaged aerosol composition.

case is shown in Figure 17. The aerosol chemical composition is obtained from Aerodyne Aerosol Mass Spectrometer (AMS) which measures particle aerodynamic diameter. AMS measure the mass concentration of sulfate, nitrite and organic and we assumed each particle is internally mixed and made up of soluble (ammonium sulfate, ammonium nitrite) and insoluble parts (organic). The stoichiometry, particle density and soluble/insoluble mass fraction of each particle is calculated and the insoluble density is taken as 1500 kg m^{-3}. For the aerosol size distribution, we use DMA measurements, which measure the aerosol mobility diameter. To determine the corresponding chemical composition of DMA aerosol size distribution, aerodynamic diameter(d_{va}) from AMS is converted to mobility diameter(d_m) by, $d_m = \frac{\rho_0}{\rho_p} d_{va}$, where ρ_0 is the standard density (1000 kg m^{-3}). ρ_p is the particle density which is calculated as average of soluble and insoluble density as weighted by mass fraction of each portion. Considering size-resolved aerosol chemical composition (Figure 17, the droplet closure of RF3C2 and RF9C1 has better agreement with observation. The size-resolved measurement show that variation of the soluble mass fraction is large among particles Figure 18. The soluble mass fraction of uniform chemical composition is summarized in Table 3.

2.5 Summary

This study analyzes 13 stratocumulus clouds sampled onboard the CIRPAS Twin Otter aircraft during the 2005 MASE (MArine Stratocumulus Experiment). A unique feature of MASE was sampling marine stratocumulus clouds under the influence of ship emissions. In-situ observations of aerosol characteristics, chemical composition, updraft velocity and ambient thermodynamic properties were inputs for i) a detailed adiabatic cloud parcel model [121, 119], and, ii) the modified NS parameterization [58, 122]; predicted drop number is then compared with the observations. Most of clouds, observed CDNC was positively correlated with average updraft velocity. The

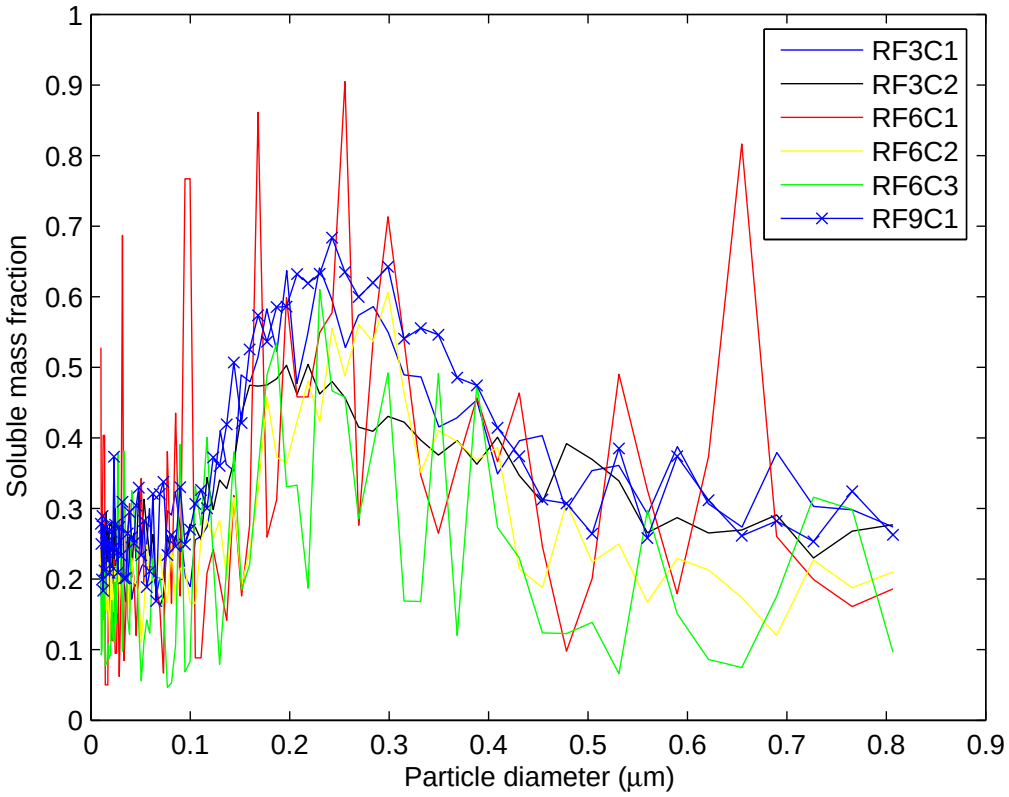

Figure 18: Average soluble mass fraction size distribution.

error in predicted cloud droplet concentration due to fitted aerosol distribution was found to be less than 25 % and the CCN number calculation is sensitive to Van't Hoff factor used. A number of significant findings arise from this study:

1. Cloud droplet number closure is remarkable even for clouds perturbed by high aerosol concentration emitted from ship exhaust.

2. The aptness of using the average updraft velocity for N prediction is justified as compared to observed drop number.

3. The chemical compositions of particles during MASE are partially soluble content from the PILS analyses.

4. Sensitivity analysis of water vapor uptake coefficient ranges from 0.01 to 1 were taken; optimum closure (for which average cloud droplet number error is minimal and its standard deviation is within droplet measurement uncertainty) is achieved when the water vapor uptake coefficient is about 0.1.

5. The cloud droplet activation parameterization used in this study [122, 58] agree as well as the detailed numerical parcel model in a high level of accuracy. Remarkable performance has also been reported by [118] and [60]. Together with the current study suggests that the parameterization can robustly be utilized in GCM assessments of the aerosol indirect effect.

CHAPTER III

PARAMETERIZATION OF CLOUD DROPLET SIZE DISTRIBUTIONS: COMPARISON WITH PARCEL MODELS AND OBSERVATIONS

3.1 Abstract

This work examines the efficacy of various physically-based approaches derived from 1-D adiabatic parcel model frameworks (a numerical model and a simplified parameterization) to parameterize the cloud droplet distribution characteristics for computing cloud effective radius and autoconversion rate in regional/global atmospheric models. Evaluations are carried out for integrations with single (average) and distributions of updraft velocity, assuming that a) conditions at s_{max} are reflective of the cloud column, or, b) cloud properties vary vertically, in agreement with 1-D parcel theory. The predicted droplet distributions are then compared against in-situ cloud droplet observations obtained during the CRYSTAL-FACE and CSTRIPE missions. Good agreement of droplet relative dispersion between parcel model frameworks indicates the parameterized parcel model essentially captures 1-D dynamics; the predicted distributions are overly narrow, with relative dispersion being a factor of 2 lower than observations. However, if conditions at cloud maximum supersaturation are used to predict relative dispersion and applied throughout the cloud column, better agreement is seen with observations, especially if integrations are carried out over the distribution of updraft velocity. When considering the efficiency of the method,

calculating cloud droplet spectral dispersion at s_{max} is preferred for linking aerosol with droplet distributions in large scale models.

3.2 Introduction

The greatest uncertainty in assessments of anthropogenic climate change arises from aerosol-cloud-climate interactions [75], termed "aerosol indirect effects". Increased aerosol concentrations tend to increase the number of droplets in warm clouds, which can enhance cloud albedo [166]; increasing droplet number also tends to reduce precipitation efficiency, which can affect cloud structure, lifetime and radiative properties [8].

Quantifying indirect effects requires a relationship between cloud microphysical properties (like number and size distribution) and its precursor aerosol. Current treatments range from empirical correlations between an aerosol proxy (such as mass) and a droplet distribution moment (typically number) [29], to explicit calculation of droplet number using a "mechanistic parameterization" [64, 122, 58, 14]. Although this is an important step towards addressing issues of aerosol-cloud interactions, calculation of droplet number and cloud liquid water content alone are not sufficient. Cloud processes are sufficiently sensitive to droplet size, so parameterizations must also include some measure of the droplet distribution. For example, autoconversion of cloud water to rain (i.e., formation of drizzle from self collision of small droplets) is a key cloud process and very sensitive to droplet size distribution; in fact, the largest uncertainty in assessment of aerosol impacts on precipitation is associated with the treatment of rain formation in large scale models [108]. Although numerous autoconversion parameterizations exist (e.g. [84, 113, 141, 87, 103], the uncertainty associated with their application is large, about a factor of ten [73], and largely related to the treatment of droplet size distribution and the size-dependence of the collection kernel.

Explicit consideration of droplet size distribution is important also for calculation

of cloud radiative properties. The effective radius, required for calculation of cloud optical depth and radiative forcing, is given by $r_e = (\frac{3L}{4\pi\rho_w kN})^{1/3}$, where ρ_w is the density of water, and the spectral parameter "k" expresses the effect of droplet width; k=1 for monodisperse droplets, decreasing as the distribution broadens. For example, [114] proposed k=0.80 for marine clouds (narrow size distribution) and k=0.67 for polluted clouds (broad size distribution). Although qualitatively correct, these k values do not capture the extent of variability in droplet distribution width seen in ambient clouds. [101, 102] recognized this and derived formulas for r_e by assuming droplets follow a gamma size distribution, and explicitly included the effect of relative dispersion (i.e., the ratio of standard deviation to average radius). When included in GCM assessments of the indirect effect, variability in droplet spectral broadening decreased indirect forcing between 14.3 and 16% [124, 140], with an upper limit of 33.1% [140].

Although resolving the droplet size distribution is required to reduce the uncertainty of aerosol indirect effects, explicit cloud droplet microphysics is computationally expensive. Parameterizations reduce the computational burden, but may (as seen in the previous examples) introduce significant predictive uncertainty. Efficient parameterization of droplet spectral width and its dependence on the cloud microphysical state (and changes thereof from aerosol perturbations) is an active area of research. [172] proposed a generalized droplet distribution derived from observational data; a number of physically-based alternatives have also been proposed to link aerosol with cloud distribution properties. [88] also relate N and droplet distribution width to cloud parameters such as updraft velocity dispersion and the vertical profile of cloud thermodynamic properties. Similarly, the cloud droplet spectrum tends to broaden when the updraft velocity decreases [126, 179]. [105] derived an analytical formula that relates the relative dispersion of cloud droplet distribution to cloud condensation nuclei (CCN) spectra and updraft velocity, based on adiabatic growth theory

of cloud droplets. These approaches apply some form of parcel theory towards computing cloud droplet spectral properties. However, few studies exist that evaluate, through the usage of in-situ cloud observations, the uncertainty in predicted droplet spectral parameters and autoconversion associated with application of parcel-based approaches.

In this work, we explore the potential of parcel-based approaches for parameterizing cloud droplet size distribution in regional and global climate models. All approaches tested assume droplets form adiabatically in individual updrafts (using a parcel model and a parameterization thereof based on the [122] and [58] activation parameterizations) to explicitly compute the size distribution and growth of an activated droplet population throughout a cloud column. We also explore another approach, based on computing the relative dispersion at s_{max} using the [122] parameterization, assuming that it applies to the whole cloud column. The overall droplet distribution, $n(D_p)$, is then computed for either a single updraft (corresponding to the average of the measured distribution), or as the superposition of droplet distributions for each updraft measured in the cloud. Each approach is evaluated by comparing predicted droplet spectral characteristics with in-situ measurements of cloud droplet size distributions for a wide range of aerosol and cloud forming conditions sampled during the CRYSTAL-FACE [46] and CSTRIPE field compaigns [118]. The importance of predicted size distribution deviations is expressed in terms of the uncertainty in the predicted spectral dispersion parameter k, and autoconversion rate; the latter is done by introducing parameterized and observed size distributions into the R_6 (i.e., sixth-moment mean radius) parameterization of [103], and quantifying the resulting differences in autoconversion.

3.3 Simulating cloud droplet growth

3.3.1 Numerical parcel model

Computation of the cloud droplet size distribution is based on the 1-D adiabatic cloud parcel framework, in which buoyant air parcels develop water vapor supersaturation, and cloud droplets activate upon aerosol particles contained within them. After a maximum supersaturation, s_{max}, is reached, all droplets have formed and grow subsequently via condensation. Since a cloud is characterized by a distribution of updrafts, the parcel concept can be further extended, so that the average droplet number and size distribution is the superposition of distributions from each updraft (or some moment thereof, e.g., [118, 125, 60]).

3.3.2 Parameterization of parcel model

Instead of numerically solving the full set of differential equations that describe the process of activation and condensational growth (e.g., [121]), we develop a simplified approach that involves two steps: *i*) calculation of the cloud drop number concentration and size distribution at the point of s_{max}, using one of the activation parameterizations of [122], [58], or [14], and, *ii*) simulation of the subsequent droplet growth as the cloud parcel ascends through a simplified treatment of condensational growth.

3.3.2.1 Determination of cloud drop size distribution at s_{max}

According to Köhler theory, a cloud condensation nucleus (CCN) requires exposure to a minimum "critical" supersaturation, s_c, before it can experience unconstrained growth and transform into a cloud droplet. s_c depends on particle size and chemical composition; therefore, the number of droplets forming in a cloud can be computed if the cloud supersaturation and the aerosol properties are known. In the initial stages of cloud formation, cooling of the air parcel leads to water vapor supersaturation; CCN then begin to activate into cloud droplets and rapidly grow. When enough CCN activate, the condensation of water vapor is strong enough to balance the availability

of water vapor for condensation (through cooling); this is the point where supersaturation reaches its maximum value, s_{max}, and determines the number of droplets that form [121]. Numerical parcel models simulate this process by solving a system of coupled differential equations (e.g., [121]), an approach that is computationally too demanding to be included within a global model. Instead, simplified approaches, known as "mechanistic activation parameterizations" (e.g., [4, 122, 58, 14]) predict CDNC at the point of s_{max} in an ascending parcel; of these, the formulations of [122], [58] and [14] explicitly predict the droplet size distribution (i.e., the concentration of droplets, dN, within a wet diameter interval dD_p) at s_{max}, as the size of all activated droplets is known. Droplet size is determined from the droplet growth equation, [132, 148],

$$\frac{dD_{pi}}{dt} = \frac{G}{D_{pi}}\left(s - s_{eq}\right) \tag{51}$$

$$G = \frac{4}{\frac{\rho_w RT}{p^s D_v M_w} + \frac{\Delta H_v \rho_w \left(\frac{\Delta H_v M_w}{RT} - 1\right)}{\kappa_a T}} \tag{52}$$

where D_{pi} is the diameter of droplet size class i, ρ_w is the water density, R is the universal gas constant, T is the parcel temperature, p^s is the saturation vapor pressure, D_v is the water vapor diffusivity, M_w is the molar mass of water, ΔH_v is the latent heat of condensation of water, k_a is the thermal conductivity of air, s is the parcel supersaturation, and s_{eq} is the equilibrium supersaturation of the droplet.

Integrating Equation (51) provides the droplet diameter, $D_p(t_{max})$ of an activated CCN at the point of s_{max},

$$D_p^2(t_{max}) = D_p^2(\tau) + 2\int_{\tau}^{t_{max}} G(s - s_{eq})dt \tag{53}$$

where τ is the time at which the CCN activates into a droplet (assumed to occur when the parcel supersaturation is equal to the CCN critical supersaturation, [122]),

t_{max} is the time in the updraft corresponding to s_{max}, and, $D_p(\tau)$ is the size of CCN at time τ.

Equation (53) can be simplified if droplet growth is assumed to be unaffected by curvature and solute effects (i.e., $s_{eq} = 0$),

$$D_p^2(t_{max}) = D_p^2(\tau) + 2\int_{\tau}^{t_{\max}} Gsdt \tag{54}$$

Since $\int_{\tau}^{t_{\max}} sdt \simeq \frac{1}{2\alpha V}\left[s_{\max}^2 - s(\tau)^2\right]$ [164], substituting into equation (54) gives for $D_p(t_{max})$,

$$D_p(t_{max}) = \sqrt{D_p^2(\tau) + \frac{G}{\alpha V}\left[s_{\max}^2 - s(\tau)^2\right]} \tag{55}$$

For most CCN, $D_p(\tau)$ can be approximated by the critical diameter, $D_c = \frac{2A}{3s_c}$, where $A = \frac{4M_w\sigma_w}{RT\rho_w}$, and M_w, σ_w are the molar mass and surface tension of water, respectively [122]; $s(\tau)$ can be approximated with the droplet critical supersaturation, $s_c = \frac{4A^3\rho_w M_s}{27\nu\rho_s M_w d_s^3}$, where M_s, ρ_s, ν, are the molar mass, density, effective Van't Hoff factor of the soluble fraction, and d_s is the dry diameter of the CCN from which the droplet formed.

Depending on the particle s_c, *i)* $D_p >> D_c$, *ii)* $D_p << D_c$ (i.e., the CCN never strictly activates), or, *iii)* $D_p \sim D_c$ (i.e., the CCN is very close to the activation point at s_{max}). The particles that have s_c lower than a characteristic "partition supersaturation" [122, 58, 14] exhibit behavior type *i* and *ii*, so Equation (55) simplifies to $D_p(t_{\max}) \simeq \sqrt{\frac{G}{\alpha V}\left[s_{\max}^2 - s_c^2\right]}$. The remaining CCN exhibit behavior type *iii*, and $D_p(s_{\max}) \simeq D_c$.

3.3.2.2 Parcel supersaturation profile beyond s_{max}

The growth of droplets beyond the point of s_{max} in the cloud requires the knowledge of the cloud supersaturation profile. Using the droplet spectrum at s_{max} (section 3.3.2.1) as an initial condition, we can then compute supersaturation with finite difference over

a small time step interval, Δt

$$s(t + \Delta t) = s(t) + \left(\frac{ds}{dt}\right) \Delta t \tag{56}$$

where $s(t)$, $s(t + \Delta t)$ are the supersaturations at time t and $t+\Delta t$, respectively, and ds/dt is the supersaturation tendency in the parcel. Assuming that the droplets are characterized by n size classes with diameters D_{pi}, concentration N_i, and growth rate dD_{pi}/dt (from Equation 51), ds/dt is given by [**?**, e.g.,]]Nenes01,Nenes03,

$$\frac{ds}{dt} = \alpha V - \gamma \frac{\pi}{2} \frac{\rho_w}{\rho_a} \sum_{i=1}^{n} D_{pi}^2 \frac{dD_{pi}}{dt} N_i \tag{57}$$

where $\alpha = \frac{gM_w\Delta H_v}{c_p RT^2} - \frac{gM_a}{RT}$, $\gamma = \frac{pM_a}{p^s M_w} + \frac{M_w \Delta H_v^2}{c_p RT^2}$, g is the acceleration of gravity, M_a, c_p is the molar mass, heat capacity of air, respectively, and p is the ambient pressure. The first term at the right hand side of Equation (57) represents the availability of water vapor from the parcel updraft motion (i.e., cooling), and the second term refers to consumption of water vapor by condensation on droplets. All properties in Equation (57) are computed for the average temperature throughout the cloud column, as simulations with a numerical cloud parcel model [121] demonstrate that this assumption does not substantially affect the supersaturation profile over a wide range of cloud conditions. With updated parcel supersaturation (equation 56), the droplets are then grown by integration of equation (51) between time t and $t + \Delta t$,

$$D_{pi}^2(t + \Delta t) = D_{pi}^2(t) + \Delta t \left\{2Gs(t + \Delta t)\right\} \tag{58}$$

The liquid water mixing ratio, W, can be computed as

$$W = \frac{\pi}{6} \frac{\rho_w}{\rho_a} \sum_{i=1}^{n} D_{pi}^3 N_i \tag{59}$$

Equations (56), (58) and (59) can be integrated until the desired liquid water mixing ratio has been reached. If the aerosol size distribution is described in terms

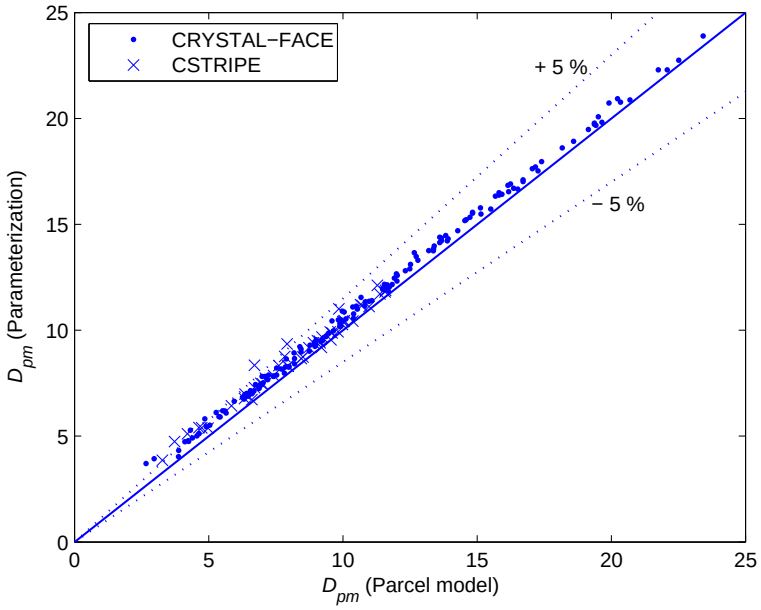

Figure 19: Mean droplet diameter (μm) as predicted by numerical and parameterized parcel models (MS, PS approaches) based on aerosol characteristics measured during CRYSTAL-FACE and CSTRIPE.

of lognormal modes, they are descretized onto size bins that range from $D_{gj} - 10\sigma_j$ to $D_{gj} + 10\sigma_j$, where D_{gj} is the geometric mean diameter of mode j, and σ_j is the geometric standard deviation for mode j.

A series of sensitivity tests were carried out to determine the optimal number of sections used in the parameterization. Using 50 sections per mode and a 0.5 s time step ensured that droplet number calculated with the parameterization agrees with the numerical parcel model predictions to within 5% (not shown).

3.3.3 Relative dispersion at s_{max} represents the cloud column

In the initial stages of cloud formation, new (small) droplets are continuously formed and grow via condensation. When supersaturation reaches its maximum value, cloud droplet formation ceases, and condensational growth, which exhibits a D_p^{-1} dependency, tends to narrow the distribution over time. This means that within the adiabatic condensational parcel model framework, relative dispersion of the droplet size

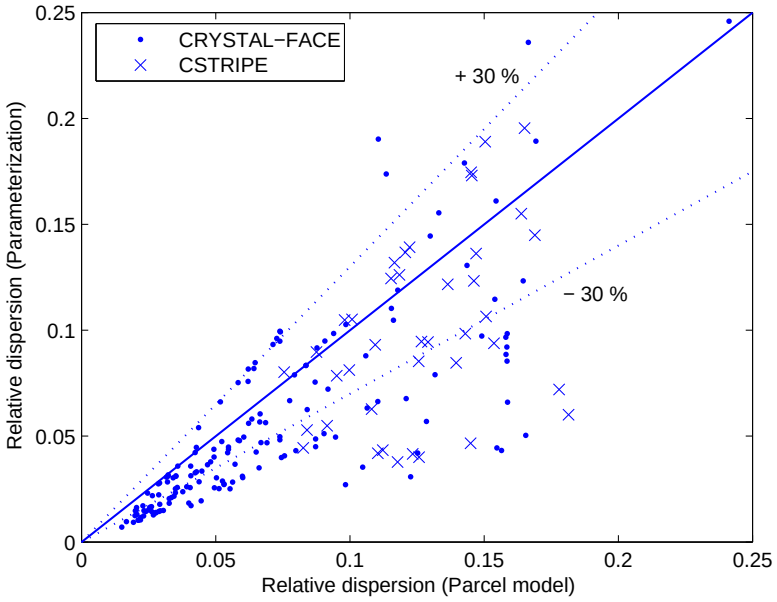

Figure 20: Same as Figure 19 but for prediction of relative dispersion.

distribution is largest at the point of maximum supersaturation. If one assumes that relative dispersion at s_{max} is representative of the entire cloud (which implies that the tendency for spectral narrowing from condensation growth is compensated by broadening from entrainment), one can use the approach described in Section 3.3.2.1 to determine the cloud spectral dispersion.

3.4 Approaches used to parameterize size distributions

Vertical profiles of droplet distribution characteristics, such as size and relative dispersion, can be computed using either of the three approaches described in Section 3.3. One issue still remaining however is the treatment of updraft velocity, as droplet distributions can be computed for a single updraft, or a distribution of updrafts. Overall, six approaches are evaluated (summarized in Table 9), as combinations of the droplet growth (Section 3.3) and updraft distribution treatments (described below), to parameterize droplet size distribution characteristics.

Table 9: Approaches used to parameterize droplet size distribution characteristics.

Symbol	Description of approach
MS	Numerical parcel model, single updraft. $\overline{D_p}(z)$, $\sigma(z)$, and $\varepsilon(z)$ computed as described in Sections 3.3.1, 3.4.1
MP	Numerical parcel model, distribution of updrafts. $\overline{D_p}(z)$, $\sigma(z)$, and $\varepsilon(z)$ computed as described in Sections 3.3.1, 3.4.2
PS	Parameterized parcel model, single updraft. $\overline{D_p}(z)$, $\sigma(z)$, and $\varepsilon(z)$ computed as described in Sections 3.3.2, 3.4.1
PP	Parameterized parcel model, distribution of updrafts. $\overline{D_p}(z)$, $\sigma(z)$, and $\varepsilon(z)$ computed as described in Sections 3.3.2,3.4.2
SS	$\varepsilon(z)$ at s_{max} for a single updraft apply to the whole cloud column. Parameterized parcel model used.
SP	$\varepsilon(z)$ at s_{max} for a distribution of updrafts apply to the whole cloud column. Parameterized parcel model used.

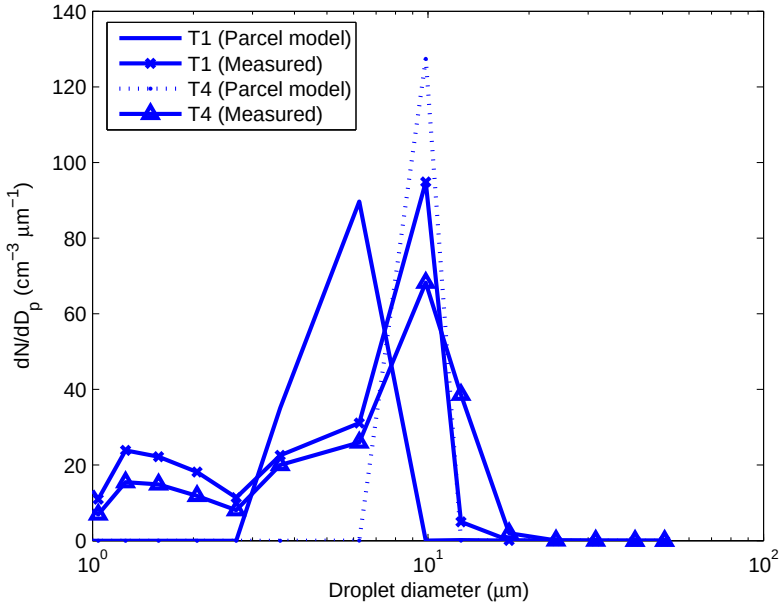

Figure 21: Observed and predicted (using approach PS) droplet spectra for CRYSTAL-FACE cloud C12-1. T1 and T4 refer to transect 1 and 4 of C12-1 [118]

.

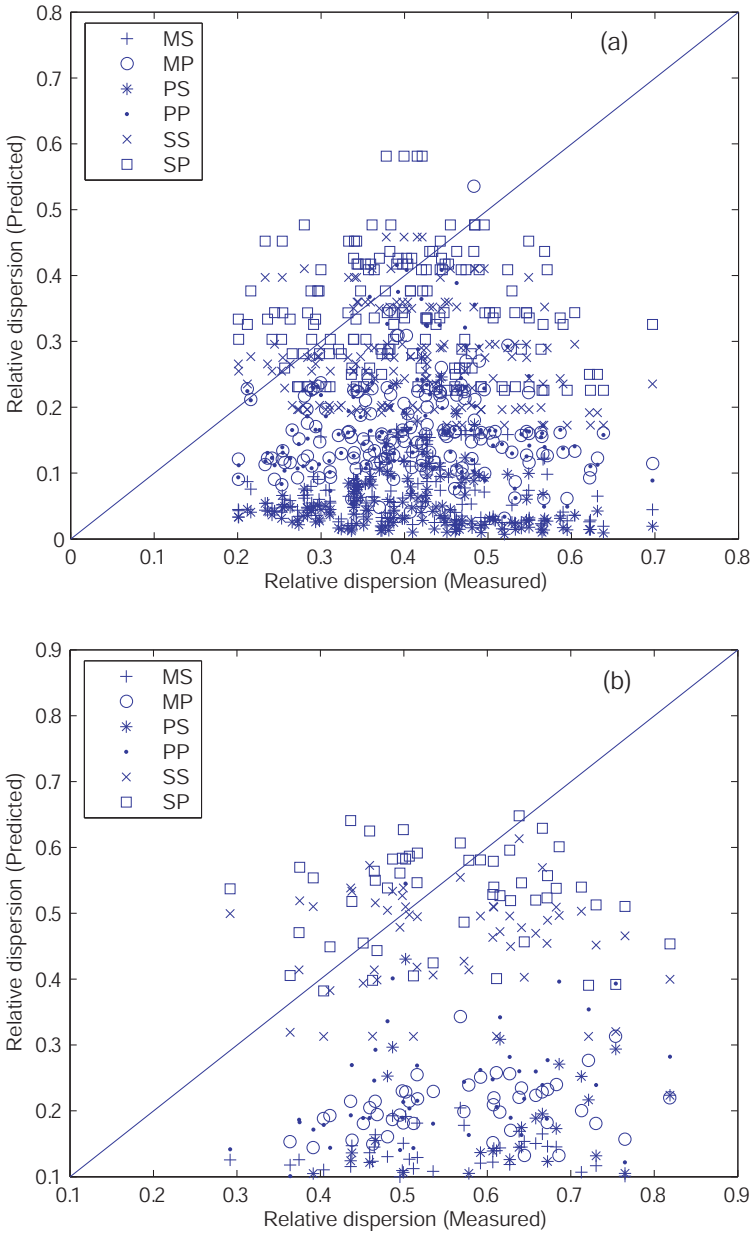

Figure 22: Prediction of relative dispersion by six approaches summarized in Table 9 compared to measurement for clouds sampled during (a) CRYSTAL-FACE and (b) CSTRIPE.

3.4.1 Single updraft

The droplet distribution computed for a single updraft at a given height (z), $n(D_p, z)$, is used to compute the vertical profile of average droplet diameter, $\overline{D_p}(z)$,

$$\overline{D_p}(z) = \frac{\int_0^\infty D_p n(D_p, z) dD_p}{\int_0^\infty n(D_p, z) dD_p} \tag{60}$$

where $\int_0^\infty n(D_p, z) dD_p = N$ is the total droplet number concentration. The vertical profile of standard deviation, $\sigma(z)$, of the size distribution is given by

$$\sigma(z) = \left(\frac{\int_0^\infty n(D_p, z)(D_p - \overline{D_p}(z))^2 dD_p}{\int_0^\infty n(D_p, z) dD_p} \right)^{1/2} \tag{61}$$

After $\overline{D_p}(z)$ and $\sigma(z)$ are determined, the relative dispersion at any given height, $\varepsilon(z)$ is

$$\varepsilon(z) = \sigma(z)/\overline{D_p}(z) \tag{62}$$

3.4.2 Distribution of updrafts

Clouds are characterized by a range of updrafts, so that the cumulative droplet size distribution becomes the superposition of distributions from each updraft. Assuming that the updraft distribution can be described with a probability density function (PDF), $p(w)$, the cloud droplet number concentration averaged over $p(w)$ is then computed as

$$N = \int_0^\infty \int_0^\infty p(w) n(D_p, w, z) dD_p dw \tag{63}$$

where by definition $\int_0^\infty p(w) dw = 1$, and, $n(D_p, w, z)$ is the droplet size distribution for a given updraft, w, and height, z. The vertical evolution of average droplet diameter and standard deviation based on averaging a series of updraft runs can be expressed as

$$\overline{D_p}(z) = \frac{\int_0^\infty \int_0^\infty D_p n(D_p, w, z) p(w) dD_p dw}{\int_0^\infty \int_0^\infty p(w) n(D_p, w, z) dD_p dw} \tag{64}$$

$$\sigma(z) = \left(\frac{\int_0^\infty \int_0^\infty n(D_p, w, z)(D_p - \overline{D_p}(z))^2 p(w) dD_p dw}{\int_0^\infty \int_0^\infty p(w) n(D_p, w, z) dD_p dw} \right)^{1/2} \tag{65}$$

$\varepsilon(z)$ is computed in a distribution of updrafts with Equation (62). In this study, $p(w)$ is assumed to follow a Gaussian PDF, the moments of which are constrained by the observed average and standard deviation of updraft velocity.

3.5 Evaluating droplet growth approaches

Each droplet approach is evaluated using in-situ measurements of ambient cloud droplet size distributions collected during the CRYSTAL-FACE and CSTRIPE field campaigns [46, 118]. Simulations were carried out for the aerosol characteristics summarized in Table 10 for CRYSTAL-FACE, and Table 11 for CSTRIPE data. [73] give a description of the cloud conditions, instrumentation and cloud droplet distribution characteristics for both datasets. To ensure that the observed distributions used to evaluate each approach were not influenced by the effects of collision-coalescence, we select horizontal transects for which the droplet distributions are single-mode and the liquid water content is within a factor of two of the adiabatic value. All of the CSTRIPE data fit this criterion, while the subset of CRYSTAL-FACE dataset used is summarized in Table 12.

In the sections that follow, we first evaluate the parameterization against the parcel model for cloud data measured during CRYSTAL-FACE and CSTRIPE. The predictions are then evaluated against the in-situ data; spectral quantities are compared at the cloud height where predicted LWC is equal to the measured value. Given that the ability of each approach to reproduce droplet number was evaluated by [46] and [118], this study focuses primarily on spectral dispersion.

Table 10: Characteristics of aerosol sampled during CRYSTAL-FACE. Size distribution is composed of four lognormal modes, with modal diameter, D_{pgi} in μm, geometric standard deviation, σ_i in μm, and concentration, N_i in cm^{-3}. Flight naming adopted from [118].

Flight	D_{pg1}	σ_1	N_1	D_{pg2}	σ_2	N_2	D_{pg3}	σ_3	N_3	D_{pg4}	σ_4	N_4
H4-1	0.011	1.32	321.8	0.052	1.49	296.8	0.15	1.45	190.3	-	-	-
H4-2	0.012	1.35	174.7	0.064	1.83	635.8	0.49	1.23	5.3	-	-	-
H4-3	0.022	1.15	15.1	0.051	1.46	215.5	0.14	1.50	168.9	-	-	-
C4	0.019	1.31	179.4	0.049	1.44	817.7	0.12	1.53	493.0	1.55	1.30	0.5
C6-1	0.012	1.13	21.1	0.038	1.60	287.8	0.13	1.41	117.0	1.66	1.22	2.7
C6-2	0.016	1.19	31.6	0.039	1.53	280.0	0.11	1.39	117.0	1.50	1.31	0.3
C6-3	0.014	1.25	97.6	0.047	1.63	672.8	0.13	1.42	187.3	1.60	1.28	0.3
C8-1	0.019	1.31	21.9	0.104	1.99	1246.0	0.61	1.25	6.2	1.62	1.27	1.5
C8-2	0.014	1.22	68.7	0.114	2.02	1127.0	0.52	1.21	11.6	1.56	1.30	1.6
C10-1	0.015	1.40	459.2	0.035	1.24	421.8	0.11	1.71	3325.0	1.57	1.30	0.5
C10-2	0.011	1.07	47.3	0.033	1.65	3833.0	0.11	1.64	3162.0	1.52	1.30	0.6
C11-1	0.020	1.10	27.6	0.095	2.06	2143.0	0.57	1.25	3.5	1.63	1.27	0.5
C11-2	0.014	1.20	181.7	0.037	1.61	1369.0	0.12	1.78	2493.0	1.77	1.20	2.1
C12-1	0.010	1.08	16.8	0.045	1.44	211.0	0.14	1.57	270.4	1.59	1.29	0.4
C12-2	0.011	1.21	137.9	0.056	1.59	241.4	0.15	1.43	259.8	1.58	1.29	0.8
C16-1	0.013	1.10	37.3	0.031	1.57	355.3	0.12	1.52	133.8	1.51	1.31	0.4
C16-2	0.017	1.26	84.1	0.033	1.54	305.6	0.14	1.35	117.6	1.65	1.25	0.6
C17-1	0.012	1.11	67.6	0.024	1.53	803.4	0.15	1.53	235.6	1.67	1.22	1.5
C17-2	0.011	1.06	51.4	0.021	1.70	494.8	0.15	1.54	226.1	1.63	1.19	1.4
C17-3	0.011	1.05	47.4	0.025	1.79	829.0	0.14	1.61	290.0	1.74	1.21	3.5

Table 11: Same as Table 10, but for aerosol sampled during CSTRIPE.

Flight	D_{pg1}	σ_1	N_1	D_{pg2}	σ_2	N_2	D_{pg3}	σ_3	N_3	D_{pg4}	σ_4	N_4
CS1	0.012	1.08	29.3	0.059	1.55	1550.0	0.18	1.31	323.7	0.54	1.21	8.6
CS2	0.013	1.19	4.2	0.061	1.32	263.7	0.16	1.53	338.0	0.83	1.06	1.0
CS3	0.029	1.18	15.6	0.064	1.47	1361.0	0.92	1.18	7.0	1.42	1.27	21.7
CS4	0.011	1.03	1.1	0.058	1.40	617.5	0.15	1.46	366.4	0.53	1.44	8.6
CS5	0.014	1.04	2.9	0.060	1.47	871.7	0.15	1.42	362.5	0.66	1.14	6.8
CS6	0.013	1.06	2.2	0.055	1.39	256.4	0.16	1.55	219.4	0.70	1.21	3.0
CS7	0.011	1.03	1.4	0.064	1.43	481.8	0.15	1.44	393.7	1.55	1.25	0.3
CS8	0.014	1.04	1.4	0.095	1.95	650.3	0.58	1.05	1.2	0.72	1.13	0.4

3.5.1 Comparison of parcel model and parameterization

The parameterized parcel model is first evaluated by comparing predicted droplet mean size, spectrum width, and relative dispersion against those of a full numerical activation adiabatic parcel model [121]. Based on the suggestion of [60], we use an effective water vapor uptake coefficient, α, of 0.06. Figure 20 shows the predicted relative dispersion from parameterization (PS approach) and parcel model (MS approach) for all clouds sampled. The comparison is carried out at the observed LWC. $\overline{D_p}$ is always well captured, as the discrepancy between parameterization and parcel model rarely exceeds 5% (Figure 19). Parameterized relative dispersion agrees with the parcel model, for most cases, to within 30% (Figure 20). The reasonably good agreement between numerical and parameterized parcel model suggests that the latter can be used for predictions of cloud droplet distributions in place of the full parcel model.

3.5.2 Comparison against observations

Predicted droplet spectra using the MS, PS approaches agree reasonably with observations for transect 4 (T4) when the cloud droplet size distributions are narrow, liquid water content is close to the adiabatic values, and the distribution is measured close to cloud base. An example of such a situation is given in Figure 21; uncertainties in measured cloud base are likely responsible for the shift between observed and measured distributions. Spectral broadening can also occur from instrument artifacts, such as laser beam non-homogeneity and coincidence error. [171] demonstrated that beam non-homogeneity in the FSSP overestimates droplet size by 10-15% when in the 15-30 micron size range, and, by 5-10% for 30-50 micron droplets. However, the same study indicated that spectrum broadening is negligible between 2 and 14 micron radius (which covers the majority of observed distributions in CSTRIPE and CRYSTAL-FACE). [171] and [17] indicated that instrument response time may cause

broadening of the distribution for air speeds higher than 55-60 m s^{-1}. Given that the Twin Otter platform operational velocity ranges between 50 - 55 m s^{-1}, broadening due to air speed is negligible. Coincidence error can also lead to broadening of the distribution when CDNC > 500 cm^{-3} [31]. Using this criterion, only a small fraction of the data could be affected, as the 75^{th} percentile of CSTRIPE data has CDNC below 370 cm^{-3}, and CRYSTAL-FACE, below 590 cm^{-3}.

Most often, however, predictions deviate significantly from observations, and is not a result of measurement uncertainty. This is shown in Figure 22, which shows the predicted relative dispersion for all six approaches versus measured values for CRYSTAL-FACE and CSTRIPE distributions. The predicted values from the parameterized parcel model are close to the results based on the numerical parcel model; however, the MS, PS approaches tend to predict narrow distributions relative to those measured. On average, relative dispersion was substantially underestimated by both numerical and parameterized parcel models using single updrafts (MS, PS). Integrating over updraft distributions (MP, PP) tends to increase predicted relative dispersion, although relative dispersion is still underestimated on average by a factor of two (Table 17). SS and SP approaches agree more closely with measurements, suggesting that when considering only condensational growth, the relative dispersion at s_{max} is a better representation of the cloud droplet size distribution than a full treatment with a 1D parcel model. This implies, to first order, that spectral narrowing from condensation balances broadening from entrainment.

3.5.3 Sensitivity of relative dispersion to the effective water uptake coefficient

It is important to assess the sensitivity of predicted spectral dispersion on the water vapor uptake coefficient, α, as the latter is a highly uncertain parameter [81, 143] that can have a profound impact on droplet number and size. This sensitivity exercise is shown in Figure 23, where predicted spectral dispersion (using the SP approach; Table

Table 12: Observed and modeled D_{pavg} (μm), σ (μm), ε for CRYSTAL-FACE clouds used in this study. Predictions carried out with the MS approach.

Flight (cloud)	D_{pavg} obs (pred)	σ obs (pred)	ε obs (pred)
C6 (1- 1)	12.48 (11.73)	3.93 (1.45)	0.31 (0.12)
C6 (3- 2)	9.47 (6.93)	1.80 (1.43)	0.19 (0.21)
C8 (1- 1)	4.34 (4.69)	1.78 (1.45)	0.41 (0.31)
C8 (1- 2)	4.70 (5.17)	1.91 (1.40)	0.41 (0.27)
C10 (1-10)	8.57 (6.54)	1.99 (0.99)	0.23 (0.15)
C12 (1- 1)	8.47 (5.98)	2.19 (0.82)	0.26 (0.14)
C12 (1- 2)	9.58 (8.08)	2.42 (1.81)	0.25 (0.22)
C12 (1- 3)	8.53 (8.08)	2.27 (1.81)	0.27 (0.22)
C12 (1- 4)	9.43 (9.85)	2.88 (0.24)	0.31 (0.02)
C12 (1- 5)	14.47 (13.27)	3.15 (1.75)	0.22 (0.13)
C12 (2- 2)	8.31 (9.50)	2.04 (1.12)	0.25 (0.12)
C16 (2- 2)	13.25 (11.99)	3.43 (1.13)	0.26 (0.09)
C16 (2- 3)	14.86 (15.03)	3.94 (2.46)	0.27 (0.16)
C17 (1- 1)	9.53 (11.69)	2.70 (1.32)	0.28 (0.11)
C17 (1- 2)	13.66 (14.12)	3.24 (2.31)	0.24 (0.16)
C17 (2- 4)	11.07 (9.97)	3.25 (0.73)	0.29 (0.07)
C17 (2- 5)	13.95 (17.45)	5.13 (0.31)	0.37 (0.02)
C17 (3- 2)	11.49 (11.46)	2.33 (1.43)	0.20 (0.12)
H4 (1- 1)	9.27 (9.10)	3.22 (1.46)	0.35 (0.16)
H4 (2- 2)	8.63 (9.65)	1.87 (0.93)	0.22 (0.10)
H4 (2- 3)	8.98 (9.93)	1.89 (0.50)	0.21 (0.05)
H4 (3- 2)	10.18 (10.57)	1.93 (1.20)	0.19 (0.11)
H4 (3- 3)	9.61 (9.88)	1.91 (0.34)	0.20 (0.03)

9) is presented against observations. The range of α considered (0.03 to 1.0) is based on the suggestions of [60], whom found that this range gives CDNC closure to within measurement uncertainty for clouds sampled during the ICARTT campaign. Overall, the water uptake coefficient has a minimal impact on relative dispersion since the normalized mean error in ε is -5.2 $\pm$ 33.8 %(0.1 $\pm$ 28.3 %) for CRYSTAL-FACE (CSTRIPE) and $\alpha = 1$, -10.4 $\pm$ 32.1 % (-0.7 $\pm$ 26.1 %) when $\alpha = 0.06$, and, -14.4 $\pm$ 31.6 % (-2.9 $\pm$ 25.4 %) for $\alpha = 0.03$.

3.5.4 Relationship between relative dispersion and droplet number concentration

[105] showed a positive correlation between relative dispersion and droplet number, with important implications for aerosol indirect forcing. We attempt to explore this in the data of our study. Figure 24 presents observed and predicted spectral dispersion (SS method) versus droplet number for all analyzed clouds from (a) CRYSTAL-FACE and (b) CSTRIPE. At first glance, the observed data seems to contradict [105], since relative dispersion tends to negatively correlate with droplet number concentration. However, the data in CSTRIPE and CRYSTAl-FACE were highly variable (both in aerosol properties and cloud dynamics), hence this variability may mask any inherent correlation between ε and CDNC. This is supported by the fact that the modeled spectral dispersion, which is consistent with the framework of [105], also exhibits a negative correlation between spectral dispersion and droplet number. Hence figure 24 expresses that, the diversity of cloud states is much larger at relatively low droplet number (i.e. resulting from clouds with high updraft velocity and low CCN concentrations, to polluted clouds with low updrafts), compared to high droplet number (which form in polluted clouds with high updraft velocity).

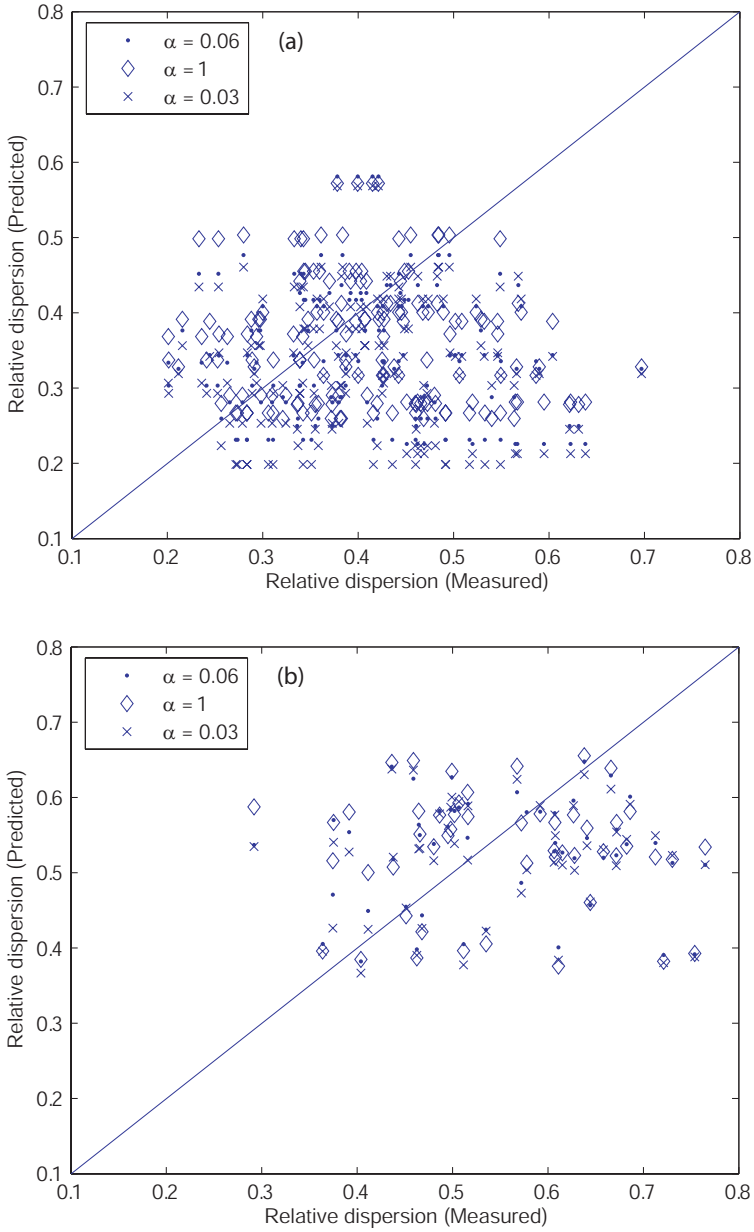

Figure 23: Predicted versus measured relative dispersion (SP approach) for a range of α for (a) CRYSTAL-FACE, and, (b) CSTRIPE clouds.

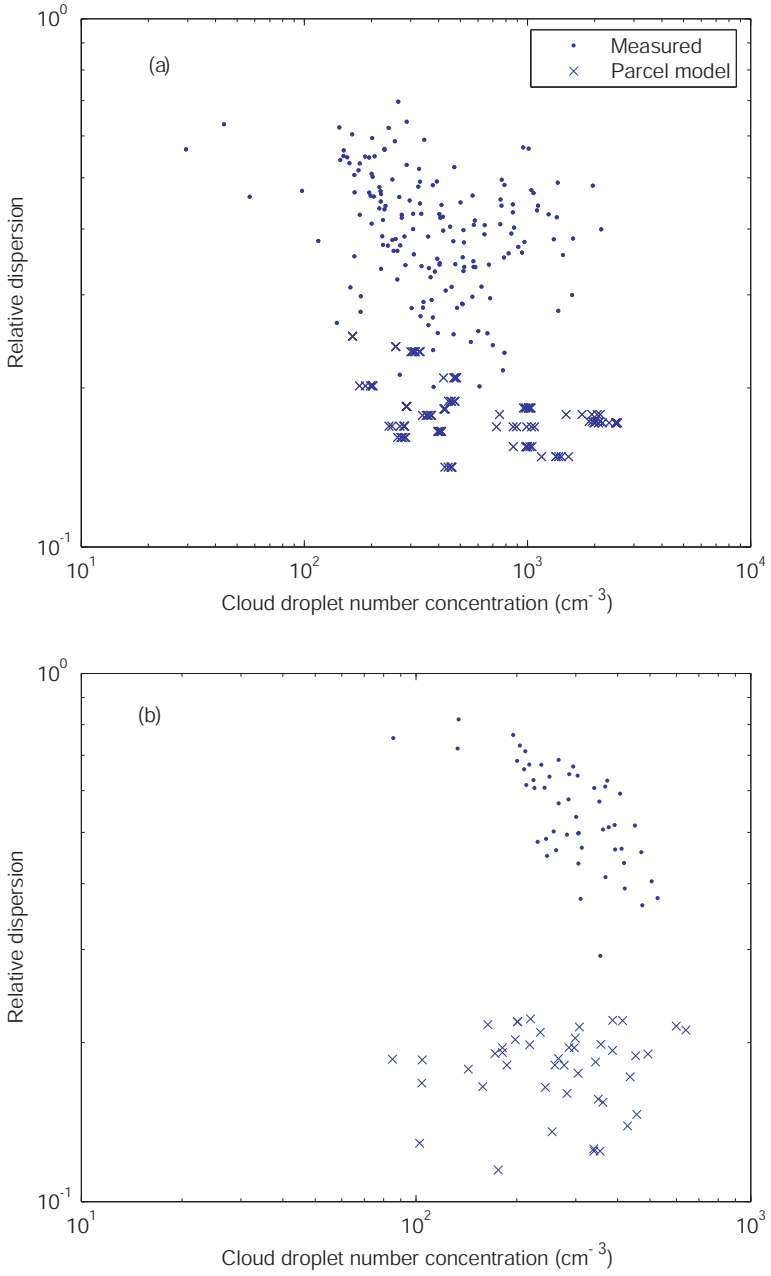

Figure 24: Measured and predicted relative dispersion (MP approach) versus droplet number concentration for (a) CRYSTAL-FACE, and, (b) CSTRIPE clouds.

3.5.5 Prediction of k

The six approaches are evaluated in terms of their ability to reproduce the spectral shape parameter k, which is the cube of the ratio of volumetric to effective radius (the analysis could also be done instead terms of the more mathematically consistent β parameter of [103], defined as r_e over the droplet volumetric radius; both analysis however are equivalent). Figure 38 shows the comparison of k between the predictions and measured data. k is substantially overpredicted using the MS, MP, PS and PP approaches for the majority of the data considered, consistent with the fact that these approaches predict narrow droplet distributions relative to those measured. Compared to CRYSTAL-FACE data, k is further overestimated in the CSTRIPE data (Figure 38, Table 17), consistent with the complex dynamics in stratocumulus clouds. With the exception of SS and SP approaches, deviations in predicted k (Table 17) is too large, being comparable to the range seen for k in the whole cloud dataset. The scatter in predicted k is fairly large, even for SS, SP; whether it is important for indirect forcing assessments requires the application of a global model, and is left for a future study.

3.5.6 Prediction of autoconversion

We now address the uncertainty in autoconversion that results from discrepancy in predicted spectral dispersion associated with each approach of Table 9. For this purpose, the R_6 autoconversion parameterization of [103] is used,

$$P_6 = \alpha_6 N^{-1/3} L^{7/3} H\left(R_6 - R_{6c}\right) \tag{66}$$

where P_6 is the autoconversion rate. N is the cloud drop number concentration, L is the liquid water content. H stands for the Heaviside function which characterizes the threshold process that controls the onset of autoconversion as the sixth moment of the cloud drop distribution, R_6, is greater than the specified threshold value R_{6c}. Finally,

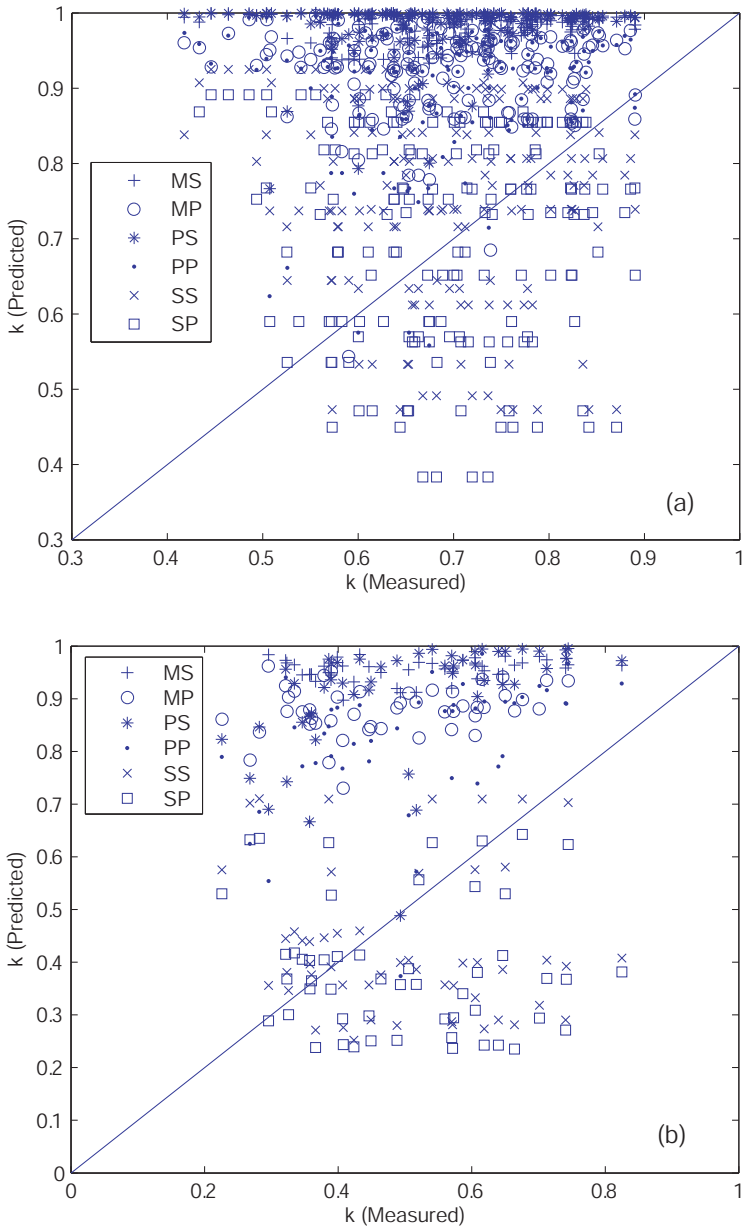

Figure 25: Observed vs. predicted k using the six approaches of Table 9 for (a) CRYSTAL-FACE, and, (b) CSTRIPE clouds.

$\alpha_6 = \left(\frac{3}{4\pi\rho_w}\right)^2 k_2 \beta_6^6 \left(\frac{L}{N}\right)^{2/3}$, where $k_2 = 1.9 \times 10^{11}$ cm^{-3}s^{-1} and β_6 is a parameter related to the relative dispersion of a gamma distribution,

$$\beta_6 = \left[\frac{(1+3\varepsilon^2)(1+4\varepsilon^2)(1+5\varepsilon^2)}{(1+\varepsilon^2)(1+2\varepsilon^2)}\right]^{1/6} \tag{67}$$

The R_6 parameterization is used for two reasons: *i*) it predicts the total coalescence rate and gives an upper limit for autoconversion (and discrepancy thereof), [73, 172], and, *ii*) total coalescence computed from the kinetic collection equation is in good agreement with R_6 for the data considered in this study [73]. Autoconversion calculations are done only for CRYSTAL-FACE clouds, given that CSTRIPE clouds are far from a precipitating state [73].

Figure 26 shows the R_6 predicted autoconversion rate, calculated based on approaches in Table 9 compared to that computed from measured cloud spectra. A summary of the normalized mean error and standard deviation is given in Table 17. Because the predicted autoconversion rates are computed using the same liquid water content as the measured values, the discrepancy between the prediction and the measurement is due to the difference in cloud droplet number and relative dispersion. On average, MS, MP, PS, PP underestimate R_6 autoconversion rate for CRYSTAL-FACE and CSTRIPE clouds on average by a factor of 3, mostly because of their underestimation of droplet relative dispersion. The autoconversion discrepancy can be large as a factor of 10, which is larger than the inherent variability of the parameterization [73]. The SS, SP tend to be in better agreement with autoconversion rate predicted from the observed spectra (Figure 26) and tends to be within the estimated uncertainty of the parameterization.

3.6 Summary

This work examines the ability of physically-based 1-D adiabatic parcel approaches to parameterize the cloud droplet distribution characteristics relevant for computation

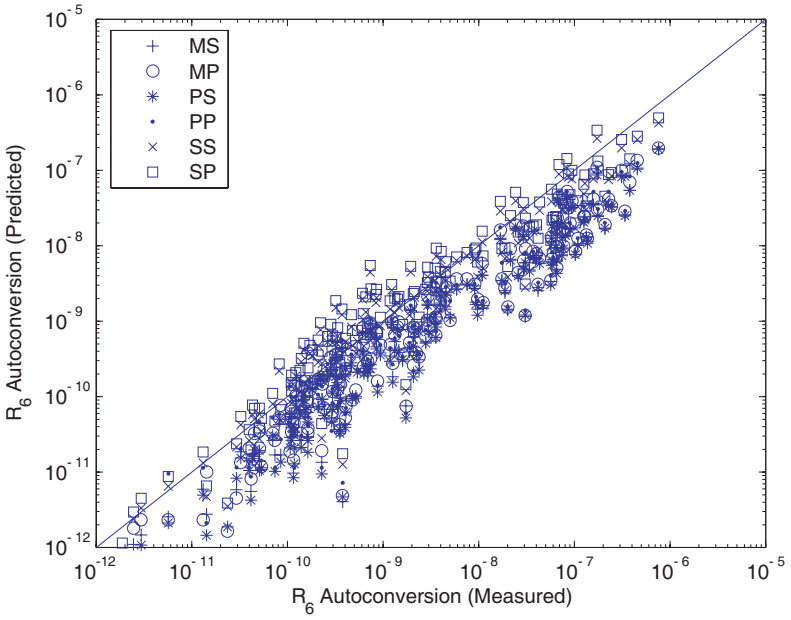

Figure 26: Observed vs. predicted autoconversion rate [kg m^{-3} s^{-1}] using the six approaches of Table 9 for CRYSTAL-FACE clouds.

Table 13: Normalized (%) mean fractional error (standard deviation) of predicted ε, k and autoconversion rate for the CRYSTAL-FACE and CSTRIPE droplet distributions.

Data set	Approach	relative dispersion	k	P_6 autoconversion
CRYSTAL-FACE	MS	-85.37(32.25)	41.30(44.27)	-66.38(24.63)
CRYSTAL-FACE	MP	-58.92(19.04)	37.04(25.20)	-58.24(32.99)
CRYSTAL-FACE	PS	-87.42(25.32)	43.37(35.53)	-68.09(24.19)
CRYSTAL-FACE	PP	-55.67(21.64)	34.12(25.30)	-59.45(31.48)
CRYSTAL-FACE	SS	-28.51(27.19)	13.79(29.61)	97.26(1278.90)
CRYSTAL-FACE	SP	-10.41(32.09)	4.97(29.62)	181.70(2011.80)
CSTRIPE	MS	-91.51(51.80)	46.84(170.20)	-
CSTRIPE	MP	-62.77(8.29)	99.46(59.90)	-
CSTRIPE	PS	-83.90(40.35)	76.89(106.70)	-
CSTRIPE	PP	-56.73(16.27)	74.22(53.38)	-
CSTRIPE	SS	-13.19(24.82)	-3.50(51.24)	-
CSTRIPE	SP	- 0.71(26.07)	-12.72(46.61)	-

of cloud effective radius and autoconversion in regional/global atmospheric models. A total of six approaches is examined, which are combinations of a numerical parcel model, a simplified parameterization, and their integrations over single updrafts and distributions thereof. Integrations are applied assuming that *i*) conditions at s_{max} are reflective of the cloud column, or, *ii*) cloud properties vary vertically, in agreement with 1-D parcel theory. Good agreement of droplet relative dispersion between parcel model frameworks indicates the parameterized parcel model captures most of the 1-D dynamics of the numerical model. When compared against in-situ cloud droplet observations obtained during the CRYSTAL-FACE and CSTRIPE missions, the distributions predicted with the parcel model (for single updrafts and distributions thereof) are too narrow, with relative dispersion being on average a factor of 2 lower than observations. However, if conditions at cloud maximum supersaturation are used to predict relative dispersion and applied throughout the cloud column, a better agreement is seen with observations, especially if integrations are done over the relevant distribution of updraft velocity; this implies that spectral narrowing from condensational growth is largely balanced by broadening from entrainment. The superiority of the latter method is reflected in predictions of the spectral dispersion parameter k (used for calculation of effective radius), but to a lesser degree in calculations of autoconversion; nevertheless, the simplicity of calculating spectral dispersion at s_{max} is attractive. Evaluation of this method however with additional in-situ cloud datasets is required before it could be recommended for usage in large scale models.

Although the SS, SP methods outperformed all approaches considered, they are based on adiabatic cloud parcel theory and may still introduce unacceptable levels of uncertainty in global modeling. Given that clouds are diabatic, parameterization that accounts for some degree of entrainment (e.g., [14]) may address this issue and further improve predictions. Such an application will be the subject of future work.

CHAPTER IV

ON THE REPRESENTATION OF DROPLET COALESCENCE AND AUTOCONVERSION: EVALUATION USING AMBIENT CLOUD DROPLET SIZE DISTRIBUTIONS

4.1 Abstract

In this study we evaluate eight autoconversion parameterizations against integration of the Kinetic Collection Equation (KCE) for cloud size distributions measured during the NASA CRYSTAL-FACE and CSTRIPE campaigns. KCE calculations are done using both the observed data and fits of these data to a gamma distribution function; it is found that the fitted distributions provide a good approximation for calculations of total coalescence, but not for autoconversion because of fitting errors near the drop-drizzle separation size. Parameterizations that explicitly compute autoconversion tend to be in better agreement with KCE, but are subject to substantial uncertainty, about an order of magnitude in autoconversion rate. Including turbulence effects on droplet collection increases autoconversion by about a factor of 1.82 and 1.24 for CRYSTAL-FACE and CSTRIPE clouds, respectively, as comparison is relative to the gravitational collection. Shifting the droplet-drizzle separation size from 20 to 25 μm in radius results in about a twofold uncertainty in autoconversion rate. The polynomial approximation to the gravitation collection kernel used to develop parameterizations provides computation of autoconversion that agree to within

30%. Collectively, these uncertainties have an important impact on autoconversion, but are all within the factor of 10 uncertainty of autoconversion parameterizations. Incorporating KCE calculations in GCM simulations of aerosol-cloud interactions studies is computationally feasible by using precalculated collection kernel tables, and can quantify the autoconversion uncertainty associated with application of parameterizations.

4.2 Introduction

Quantifying the impacts of aerosol on global cloud, known as the "aerosol indirect climatic effect" is an important agent of climate change. Increases in aerosol concentration from natural background levels tend to decrease average cloud drop size, which enhances cloud albedo ("first indirect effect", [166]) and can reduce precipitation efficiency ("second indirect effect", [9]). The precipitation rate predicted in general circulation models (GCMs) is controlled by autoconversion, the process of collision-coalescence that leads to the formation of new small drizzle drops; changes in precipitation from aerosol effects are then represented as changes in the autoconversion rate. Estimates of indirect effects are subject to large uncertainty [75], a result of the incomplete representation of cloud microphysical processes, especially autoconversion of cloud water to rain [108, 106, 80, 117, 116]. Predicted spatial and temporal evolution of liquid water path (LWP) in large-scale models is strongly influenced by the autoconversion scheme; hence accurately quantifying the autoconversion rate is ultimately required for reducing indirect effect uncertainty.

Drizzle drops, defined as those with radius larger than a threshold, r_0 (typically 20 μm with corresponding mass x_0; [173]), are the precursor to rain and are produced mainly by the collisions of small cloud droplets from activation of cloud condensation nuclei (CCN). "Autoconversion" can then be defined as the coalescence of cloud droplets, each with mass less than x_0, to form drizzle drops of mass larger than

x_0. A collision event can also produce a cloud drop with mass less than x_0, and is called "self-collection" [20, 19, 147]. If the droplet size distribution is known, the autoconversion rate A can be computed from the Kinetic Collection Equation (KCE) [132, 173]:

$$A = \int_0^{x_0} \left[\int_{x_0 - x}^{x_0} K(x, x') x' n(x') dx' \right] n(x) dx \tag{68}$$

where $K(x, x')$ is the collection kernel and $n(x)$ is the drop size distribution (DSD).

Explicitly resolving the collection process is generally considered computationally expensive [87, 135] and has seen limited usage in GCM simulations. Instead, parameterizations are used, where the autoconversion rate is expressed in terms of size distribution moments, such as liquid water content (LWC) [84], cloud droplet number concentration (CDNC) [113, 141, 87], and spectral dispersion [19, 45, 103]. Parameterizations are often developed from simplified forms of KCE with prescribed cloud droplet size distributions and collection kernels. For example, [113] developed a formulation assuming that autoconversion is a threshold process, which commences once a "critical" value for liquid water content is exceeded. When autoconversion is active, an average collision frequency is assumed for all cloud droplets, resulting in an autoconversion rate that scales with $\mathrm{LWC}^{7/3}$. [103] developed an analytical expression for autoconversion rate as a function of LWC, CDNC, and the relative dispersion (a measure of DSD width) of the cloud drop size distribution. Their formulation is derived by analytically integrating the KCE, using an approximate form of the gravitational collection kernel assuming the DSD follows a gamma distribution. The magnitude of autoconversion rate is given by the product of rate function and threshold function, as the later represents the fraction of the total coalescence and is recently derived as a function of droplet distribution width [105]. Another approach to developing autoconversion parameterizations is to derive them from detailed microphysical simulations with a numerical cloud model. [87] adopted this approach, and

used a wide range of simulated DSDs obtained from Large-Eddy Simulation (LES) of drizzling marine stratocumulus to fit autoconversion rates (using least square minimization) to simple power-law expressions that depend on droplet number and liquid water content.

Autoconversion parameterizations are subject to considerable uncertainty, as when applied to the same cloud microphysical state can give autoconversion rates that vary up to three orders of magnitude [173]. The implications are very important for hydrological cycle simulations, as the timescale for forming precipitation can be in substantial error, leading to systematic shifts in precipitation patterns. The process of "tuning" a parameterization to match observed precipitation patterns (e.g., [141]) may partially offset this bias, but is inherently limited owing to the multiple scales involved and the nonlinearity of the autoconversion process.

Many reasons exist for the large differences seen between autoconversion parameterizations. First, parameterizations do not necessarily use the same definition for autoconversion. For example, the threshold size used for separating drizzle from cloud drops by [87] is 25 μm, and, 20 μm by [173]. [103] do not consider a threshold at all, and instead predict total coalescence P (i.e., all collection events, regardless of their droplet size), done by changing the integration limits of (86) to,

$$P = \int_0^\infty \left[\int_0^\infty K(x, x') x' n(x') dx' \right] n(x) dx \tag{69}$$

Uncertainty in predicted autoconversion may also result from the DSD assumed (e.g., gamma or lognormal) in the development of each formulation. Substantial uncertainties in predictions of autoconversion rate also arise from the form of the collection kernel used. The essential kernel is that for gravitational coalescence under quiescent conditions, and is that which the exclusive majority of parameterizations employ. Cloud-scale turbulence however is known to augment the coalescence rate, and can be included by adding a turbulent kernel into the collection process (e.g.,

[136, 137]). Incorporating turbulence effects in a parameterization, however, is challenging, given the complex form of the collection kernel (e.g., [11, 12]). Whether or not turbulence effects should be included in parameterizations still remains an open question, given that the augmentation in autoconversion rate may still be within the inherent uncertainty of parameterizations.

In this study, we assess the importance of assumptions used in the development of autoconversion parameterizations. We first examine the error in autoconversion associated with using an analytic distribution (such as the gamma distribution), by comparing predicted autoconversion rates from the KCE employing observed distributions and fits to them. KCE calculations of autoconversion rate are then compared against parameterizations, to characterize their inherent uncertainty. We also explore the sensitivity of predicted autoconversion to the droplet size threshold used for calculating A, by comparing KCE calculations of A against P. The importance of including turbulence effects in KCE calculations of autoconversion rate is also examined. Finally, we assess the computational efficiency of KCE against autoconversion parameterizations.

4.3 Cloud microphysics

4.3.1 Observational datasets

Cloud droplet size distributions used in this study were collected aboard the CIRPAS Twin Otter aircraft (http://www.cirpas.org/) during two field campaigns: CRYSTAL-FACE in Key West, FL (July 2002) and CSTRIPE in Monterey, CA (July 2003). Measurements taken during CRYSTAL-FACE focused on low-level cumuliform clouds [46, 167], whereas marine stratocumulus clouds were the focus of CSTRIPE [118]. Detailed description of flights and sampling strategies for both campaigns are provided in [167], [46], and [118]. In both campaigns, droplet size distributions were measured

Table 14: Droplet size distribution characteristics of clouds sampled during CRYSTAL-FACE and CSTRIPE.

Cloud Property	Mean Value	Standard deviation	Percentile 25^{th}	Percentile 50^{th}	Percentile 75^{th}
CRYSTAL-FACE					
LWC (kg m^{-3})	4.80×10^{-4}	4.06×10^{-4}	1.80×10^{-4}	3.45×10^{-4}	6.98×10^{-4}
CDNC (cm^{-3})	480	367	227	365	593
$\overline{D_p}$ (μm)	10.67	4.00	7.78	9.67	13.67
σ_p (μm)	4.34	2.28	2.49	3.51	6.06
ε_p	0.41	0.10	0.34	0.41	0.47
CSTRIPE					
LWC (kg m^{-3})	1.50×10^{-4}	9.56×10^{-5}	5.89×10^{-5}	1.39×10^{-4}	2.39×10^{-4}
CDNC (cm^{-3})	304	97	234	298	370
$\overline{D_p}$ (μm)	7.18	2.08	5.22	7.22	8.79
σ_p (μm)	3.84	0.89	3.29	3.74	4.64
ε_p	0.56	0.12	0.47	0.55	0.64

with a Cloud and Aerosol Spectrometer (CAS) optical probe [16] and a Forward Scattering Spectrometer Probe (FSSP) [31]. The observed DSDs range between 1 to 25 μm in radius; haze droplets (less than 1 μm) and their impact on collection will not be considered. We use transect-averages for KCE calculations (using higher resolution data does not affect the closure between parameterizations and KCE); 164 transects are available from CRYSTAL-FACE, and 52 from CSTRIPE. Table 14 summarizes DSD characteristics (LWC, CDNC, mean droplet diameter $\overline{D_p}$, standard deviation σ_d for D_p, and relative dispersion for D_p, $\varepsilon_d = \sigma_d/\overline{D_p}$) for CRYSTAL-FACE and CSTRIPE data. In CRYSTAL-FACE (CSTRIPE) clouds, 25^{th} and 75^{th} percentiles of CDNC are 227 (234) cm^{-3} and 593 (370) cm^{-3}. The 25^{th} and 75^{th} percentiles of mean diameter for CRYSTAL-FACE (CSTRIPE) are 7.78 (5.22) μm and 13.67 (8.79) μm. Compared to CRYSTAL-FACE, CSTRIPE clouds are characterized by smaller LWC, CDNC, $\overline{D_p}$ and σ_p; this is consistent with the weaker dynamics and cloud depths associated with marine stratocumulus.

4.3.2 Autoconversion parameterizations studied

The parameterization schemes used in this study are summarized in Table 20 and include (a) [113], MC, (b) [19], BH, (c) [87], KK, (d) [103], LD4, (e) [103], LD6, (f) [159], (SD-L for over land, and, SD-O for over ocean) with modifications by [48] to include a stronger dependence of autoconversion on LWC. These parameterizations, when applied to the same cloud, predict substantially different autoconversion rates. This is shown in Figure 39, which presents predicted autoconversion rate for each parameterization in Table 20. The assumed CDNC is 300 cm^{-3}, and the relative dispersion is taken as 0.5 for the LD4, LD6, and BH parameterizations. At these cloud conditions, the BH scheme exhibits the largest dynamic range of autoconversion rate. KK generally predicts the lowest autoconversion rate and LD4 the highest; the two expressions on average, differ by a factor of 120, and at low values of LWC, by 3 orders of magnitude. At lower LWC range, SD-O is close to LD6, but for LWC $>\sim$1.3 g m^{-3} converges to SD-L at a higher level than KK. To assess the importance of these differences, one can express them in terms of a timescale for rain formation, τ_{rain}. Since autoconversion is the rate-limiting step for forming rain [45], τ_{rain} can be approximated with the timescale of autoconversion, τ_{auto} = LWC/A . If, for example, a cloud is characterized by LWC $\sim$1 g m^{-3} and an autoconversion rate of $\sim 10^{-7}$ kg $m^{-3}s^{-1}$, τ_{rain} $\sim$2.7 h; hence, such a cloud may form rain during its lifetime (20 mins - few hours); for clouds with lower autoconversion rates ($<10^{-8}$), τ_{rain} is too large (>27 h), and such clouds are unlikely to produce rain. Hence, a factor of 10 difference in autoconversion in the $\sim 10^{-8}$ - 10^{-7} range represents the difference between a precipitating and non-precipitating cloud. Large uncertainties in autoconversion rates when $A < 10^{-9}$ or $A > 10^{-6}$ are, on the other hand, less important.

Table 15: Autoconversion parameterizations considered in this study. [a]

Scheme	Autoconversion rate (kg m^{-3} s^{-1})
MC, [113]	$A_{MC} = \pi\kappa_1 \left(\frac{3}{4\pi\rho_w}\right)^{4/3} EN^{-1/3}L^{7/3}H\left(R_3 - R_{3c}\right)$
BH, [19]	$A_{BH} = -6.0 \times 10^{28} w^{-1.7}(N \times 10^{-6})^{-3.3}(L \times 10^{-3})^{4.7}$
KK, [87]	$A_{KK} = 1350 q_c^{2.47}(N \times 10^{-6})^{-1.79}$
LD4, [103]	$P_{LD4} = \pi\kappa_1 \left(\frac{3}{4\pi\rho_w}\right)^{4/3} E\beta_4^4 N^{-1/3}L^{7/3}H\left(R_4 - R_{4c}\right)$
LD6, [103]	$P_{LD6} = \left(\frac{3}{4\pi\rho_w}\right)\kappa_2\beta_6^6\left(\frac{L}{N}\right)^{2/3} N^{-1/3}L^{7/3}H\left(R_6 - R_{6c}\right)$
SD, [159]	$A_{SD} = C_0 q_c \left\{1 - \exp\left[-\left(\frac{L}{L_c}\right)^4\right]\right\}$

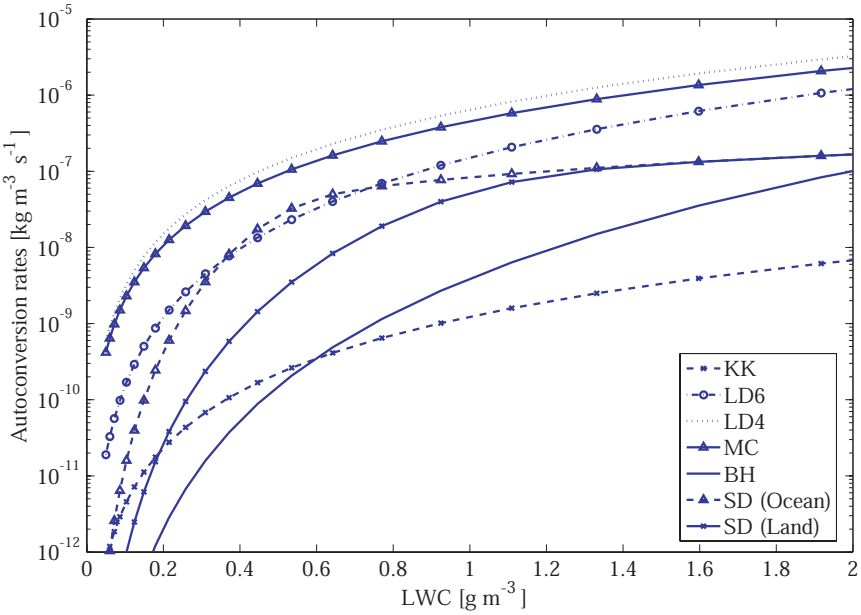

Figure 27: Autoconversion rate predicted by the parameterizations in Table 20, as a function of LWC for a cloud with a total drop concentration of 300 cm^{-3}. For LD4, LD6 and BH, a spectral dispersion of 0.5 is assumed.

4.4 Parameterizations vs. KCE with fitted DSD

In this section, we assess the ability of LD6 to reproduce the autoconversion and total mass collection rate predicted by integration of KCE for gamma distributions (obtained from fits to ambient observed size distributions). Other parameterizations are not evaluated here, since the fitted and observed DSD have identical microphysical moments (i.e., CDNC, LWC, ϵ); the comprehensive intercomparison will be considered in Section 4.5. In the following sections, we present the procedure to fit a gamma distribution to observed DSDs, and then proceed to quantifying the error in autoconversion rate associated with *i*) assuming $P{=}A$, and, *ii*) using the polynomial approximation to the gravitational collection kernel as the former is used in the derivation of LD6.

4.4.1 Relating gamma distribution to DSD moments

A DSD is said to follow a gamma distribution, $n(r)$, with shape parameter k and scale parameter θ, if [103],

$$n(r) = N_0 r^{k-1} e^{-r/\theta} \tag{70}$$

N_0, k and θ are constants, and can be related to the total droplet number concentration N, the liquid water content LWC obtained from the measured distributions, and the relative dispersion ε (a measure of the width of $n(r)$),

$$\varepsilon = \sigma / r_m \tag{71}$$

where σ, r_m are the standard deviation and mean radius of the cloud drop distribution,

$$\sigma = \sqrt{\frac{\int_0^\infty (r - r_m)^2 n(r) dr}{\int_0^\infty n(r) dr}} \tag{72}$$

$$r_m = \frac{\int_0^\infty r n(r) dr}{\int_0^\infty n(r) dr} \tag{73}$$

N_0 is expressed in terms of k and θ from the zeroth moment of measured DSD:

$$N_0 = \frac{N}{\Gamma(k)\theta^k} \tag{74}$$

where Γ is the gamma function and k is related to the observed relative dispersion, which is given by [103]:

$$k = \varepsilon^{-2} \tag{75}$$

The parameter θ in Equation 70 is determined by equating the the third moment of the gamma distribution with the measured LWC [45],

$$\theta = \left(\frac{6}{\pi} \frac{LWC}{\rho_w} \frac{\Gamma(k)}{\Gamma(3+k)} \right)^{1/3} \tag{76}$$

4.4.2 Procedure for fitting DSD and calculation of A

The gamma distribution fit to each measured DSD (Equation (70)) is determined by first computing the LWC, σ_c, and r_m from the observed data. Then, k is computed from Equations (71) and (75); θ is computed from Equation (76), and N_0 from Equation (74). Examples of measured vs. fitted distributions for the two field campaigns are given in Figure 28. In general, the gamma distribution provides a better fit to CRYSTAL-FACE data (which tend to be narrow) than for CSTRIPE; the importance of these discrepancies is assessed in Section 4.4.3.

After determining the k, θ and N_0 for each measured DSD, we proceed with computing A (Equation (86)) for the fitted $n(r)$ of each measured distribution. This is done by discretizing $n(r)$ onto a grid; the number of droplets in each size bin is equal to $F(r_+) - F(r_-)$, where r_-, r_+ are the lower and upper size bounds of the discretized droplet bin, respectively, and $F(r)$ is the cumulative number concentration

from 0 to r,

$$F(r) = \int_0^r N_0 \chi^{k-1} e^{-\chi/\theta} d\chi = N_0 \theta^k \gamma(k, \frac{r}{\theta}) \tag{77}$$

where γ is the incomplete gamma function [5].

When computing A (Equation (86)) or P (Equation (69)), the polynomial approximation to the gravitational collection kernel (for $r \leq 50\mu m$) is used [110],

$$K(r_1, r_2) = K_2(r_1^6 + r_2^6) \tag{78}$$

with $K_2 = 0.04 \times 10^{15}$ m^{-3} s^{-1}; r_1 and r_2 are the colliding droplet radii (m). Equations (86) and (69) are then numerically integrated with the discretized size distributions to obtain the autoconversion rate. For measured DSDs, we use the CAS size bins (covering 1 to 25 μm in mean radius) and for the fitted gamma distribution, we discretize over 100 sections with logarithmically-spaced size bins from 1 to 25 μm in radius.

4.4.3 The appropriateness of gamma distribution fits for coalescence and autoconversion

The sensitivity of KCE integration to the specified DSD is evaluated first using the fitted DSDs for CRYSTAL-FACE clouds. The excellent agreement between LD6 and KCE (average relative difference, 5 %) confirms that the polynomial collection kernel (used in the analytical derived LD6) is a good approximation to Equation (78). Table 16 summarizes the mean error and standard deviation in predicted coalescence and autoconversion rates that results from fitting the observed CRYSTAL-FACE and CSTRIPE DSDs to a gamma function (Section 4.4.2). Generally, the mean error for autoconversion that results by fitting distributions is much greater than for coalescence rate; in fact, the coalescence rate is well captured by the fit, even for the broad size distributions of CSTRIPE (which may not be described well by a gamma distribution, Figure 28b). This implies that the autoconversion computation by integrating KCE is very sensitive to the fitting distributions, because the distribution

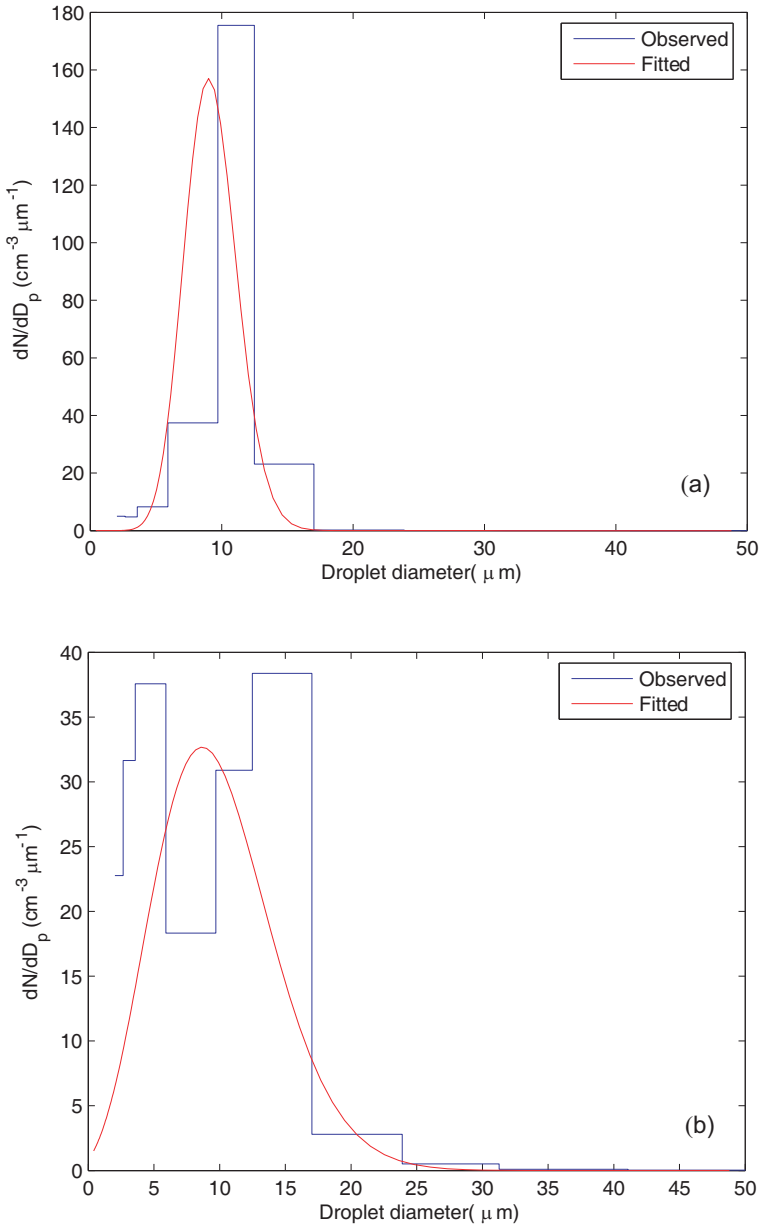

Figure 28: Examples of measured and fitted DSD (a) CRYSTAL-FACE C4 cloud (transect 3) and (b) CSTRIPE CS1 cloud (transect 4).

of droplets which are close to the drizzle threshold size strongly depends on the distribution function used. To estimate the autoconversion uncertainty resulting from the droplet binning scheme, the fitting procedure of size distribution is also repeated with designated particle bins from CAS probe. The difference in autoconversion is decreased but still large (2.66 for CRYSTAL-FACE, 4.17 for CSTRIPE). Most of this uncertainty arises from the deviations in the fitted distribution to the observations at large droplet sizes (which is more pronounced for the CSTRIPE dataset); the latter effect is magnified when autoconversion is computed. This suggests that the skewness of DSD may need to be accounted for an effective parameterization of the autoconversion process.

4.5 Parameterizations vs. KCE with measured DSD

Here, we quantify the autoconversion rate discrepancy between KCE calculations using the observed DSD and the parameterizations of Table 20. Figure 29 presents the predicted total mass coalescence of cloud droplets calculated using LD6, against KCE computations for observed CRYSTAL-FACE DSDs. The agreement in coalescence rate between KCE and LD6 is almost as close as in the evaluation using fitted (gamma function) DSDs (not shown). For higher autoconversion rates (10^{-7} - 10^{-6}, which correspond to clouds most susceptible to rain formation), LD6 overestimates coalescence by about a factor of 2 (Figure 29); however, this may not be important for simulations of the hydrological cycle, as the precipitation timescale is already small for such clouds. This further supports that prescribing a gamma distribution is a good approximation for calculations of total coalescence.

Total coalescence is not autoconversion; because LD6 predicts coalescence rates, it overestimates autoconversion by about a factor of 49 for CRYSTAL-FACE and 5 for CSTRIPE clouds (Figure 30). This is consistent with [173], who showed an overestimation by a factor of 3.8 to 112 for marine boundary layer clouds sampled in the

northeast Atlantic Ocean. This overestimation does not exhibit a constant bias, nor does it have a strong correlation with LWC, given that the ratio of self-collection to autoconversion varies significantly between clouds (Figure 31a). However, the ratio correlates strongly with τ_{auto} (Figure 31b); application of LD6 would give a good approximation to A when the ratio is less than unity, i.e., only for heavily drizzling clouds with $\tau_{auto} < 30$ hr for CSTRIPE, and, $\tau_{auto} < 3$ hr for CRYSTAL-FACE (Figure 31b). The KK parameterization (which was explicitly developed to provide A) predicts systematically lower conversion when compared to LD6 (Figure 29). KK is in better agreement with KCE integrations for autoconversion rate (Equation (86) for $r_0 = 20$ μm; [173]) and consistently tends to give the lowest mean error for CRYSTAL-FACE clouds (Table 17, Figure 30), but is still subject to substantial uncertainty (Figure 30; Table 17). As substantial as it may seem, this scatter is within the inherent uncertainty of the parameterization ($\sim$ 1-2 orders of magnitude; [87]). A sensitivity analysis (section 4.5.3) suggests that the different thresholds used for KCE are not responsible for the bias and scatter of Figure 30. The other parameterizations in Table 20 do not give better results than KK. LD4 and MC closely agree with each other (Figures 30a and 30b) but substantially overestimate autoconversion, largely because both assume that the collection efficiency is independent of drop size [113]. SD-L substantially overestimates as well, while SD-O agrees within a factor of 2 at high autoconversion rates. Large discrepancy between KCE calculations and parameterizations is also seen for the CSTRIPE DSDs (Figure 30b; Table 17); LD6 on average most closely approximates overall KCE calculations.

4.5.1 LD6 with threshold function

The overestimation of autoconversion from LD6 was initially pointed out in the study of [173]; in response, [104] state that LD6, which is a rate function, should be multiplied with a threshold function to give the autoconversion rate. In this section, we

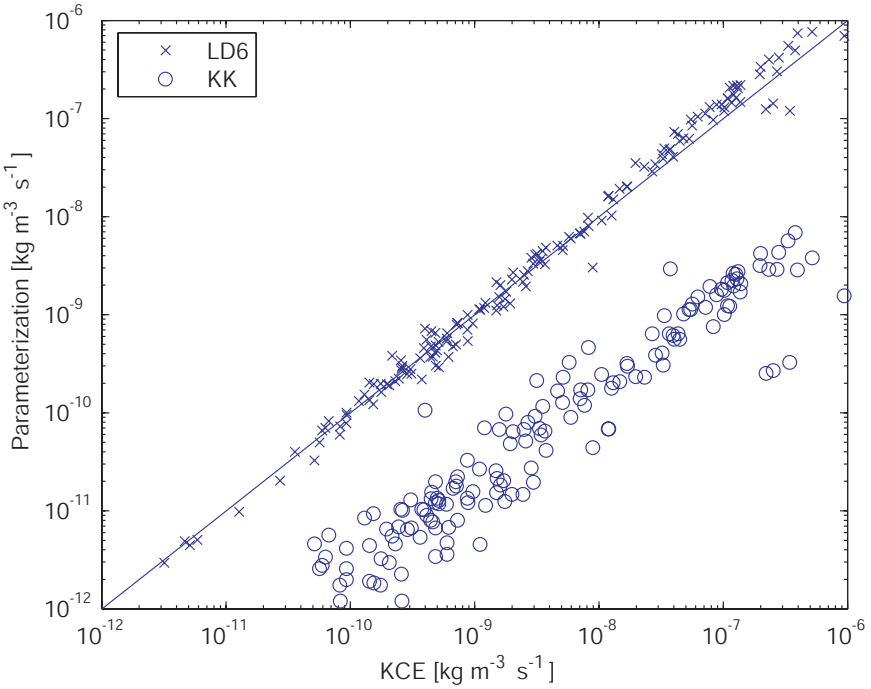

Figure 29: Parameterized autoconversion versus coalescence from KCE calculations for measured CRYSTAL-FACE DSDs. Note LD6 predicts total coalescence [173].

Table 16: The mean error and standard deviation of KCE autoconversion (coalescence) rate from application of KCE. Calculations are done using fitted and measured DSD for CRYSTAL-FACE and CSTRIPE data sets. The difference is represented in terms of orders of magnitude.

	$\log(A_{measured}/A_{fitted})$	
Dataset	Mean	Standard deviation
Coalescence rate		
CRYSTAL-FACE	-0.01	0.13
CSTRIPE	0.33	0.29
Autoconversion rate		
CRYSTAL-FACE	3.55	5.70
CSTRIPE	5.18	3.50

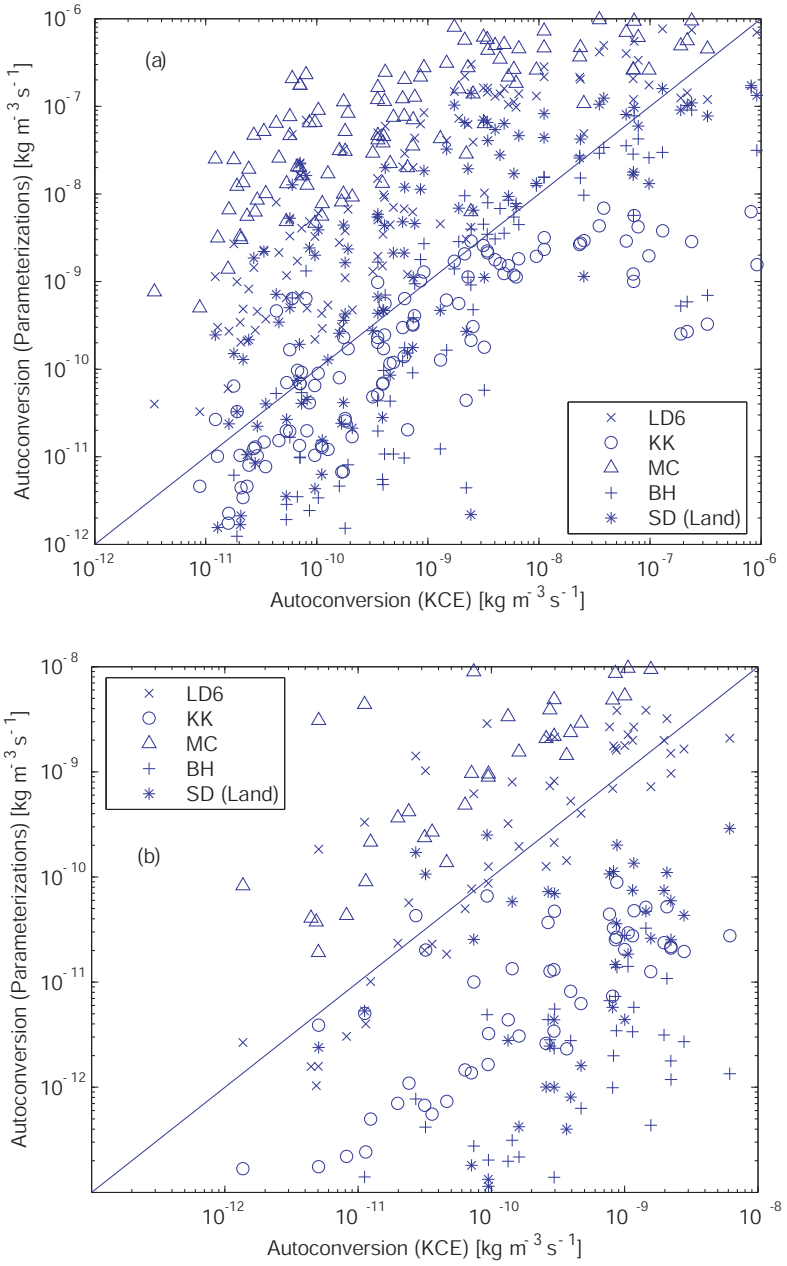

Figure 30: Autoconversion rates predicted by LD6, KK, MC, BH and SD-L parameterizations versus KCE calculations using measured DSDs from (a) CRYSTAL-FACE, and, (b) CSTRIPE

Table 17: Mean (standard deviation) of $\log(A_{KCE}/A_{param})$ and $\log(\tau_{KCE}/\tau_{param}$. Error statistics for LD6 multiplied with the threshold function (T), parameterization are computed for data points with an autoconversion rate $> 10^{-9}$.

Parameterization	$\log(A_{KCE}/A_{param})$	$\log(\tau_{KCE}/\tau_{param})$
	CRYSTAL-FACE	
KK	1.43 (1.70)	-4.30 (1.67)
LD6	-2.75 (1.52)	0.79 (1.00)
LD6(T)	-1.89 (1.88)	0.66 (1.13)
LD4	-4.95 (1.74)	1.93 (0.79)
MC	-4.67 (1.80)	1.50 (0.82)
BH	2.81 (2.87)	-2.13 (2.18)
SD-O	-2.51 (2.30)	-0.39 (0.80)
SD-L	-0.66 (2.41)	-0.97 (0.99)
	CSTRIPE	
KK	3.34 (1.29)	-4.00 (0.80)
LD6	-0.50 (1.34)	0.18 (0.74)
LD6(T)	5.27 (3.96)	-5.85 (4.50)
LD4	-3.23 (1.33)	2.59 (0.58)
MC	-2.81 (1.40)	2.18 (0.62)
BH	6.46 (1.97)	-6.01 (1.49)
SD-O	2.05 (3.29)	-1.13 (1.44)
SD-L	4.80 (3.30)	-3.88 (1.46)

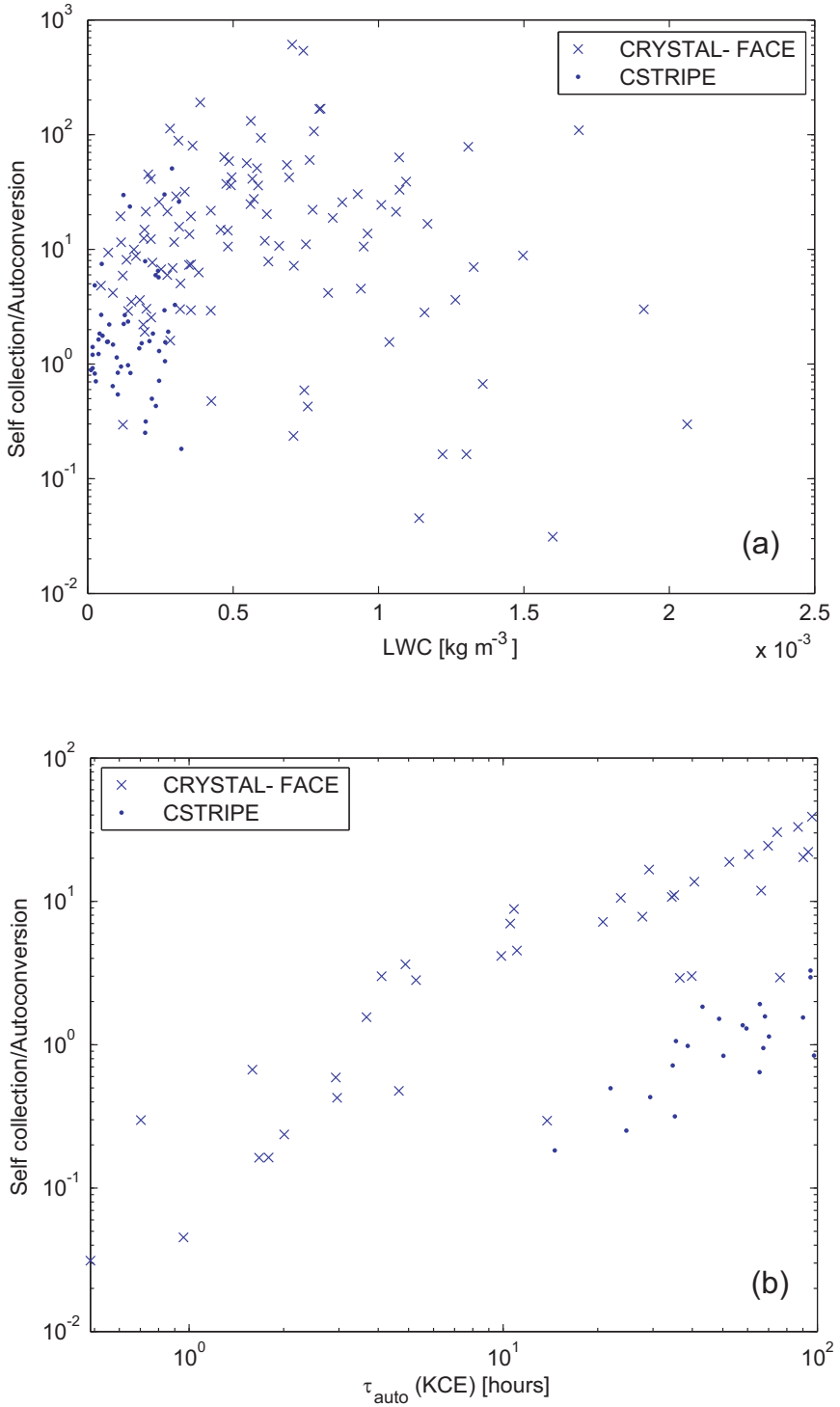

Figure 31: The ratio of self-collection to autoconversion vs. (a) LWC, and, (b) τ_{auto} for CRYSTAL-FACE and CSTRIPE clouds.

evaluate LD6 multiplied by the autoconversion threshold function, T_ε, of [105],

$$T_\varepsilon = \gamma'\left(\frac{6+\varepsilon^{-1}}{\varepsilon^{-1}}, \gamma^{1/(3\varepsilon)}\left(\frac{3+\varepsilon^{-1}}{\varepsilon^{-1}}\right)x_c^{1/(3\varepsilon)}\right)\cdot\gamma'\left(\frac{3+\varepsilon^{-1}}{\varepsilon^{-1}}, \gamma^{1/(3\varepsilon)}\left(\frac{3+\varepsilon^{-1}}{\varepsilon^{-1}}\right)x_c^{1/(3\varepsilon)}\right) \tag{79}$$

where x_c is the critical-to-mean mass ratio, and $\gamma' = \gamma/\Gamma$.

Figure 32 shows the generalized threshold function as a function of the mean-to-critical mass ratio (x_c^{-1}), for DSDs of constant ε (lines), CRYSTAL-FACE (dots) and CSTRIPE clouds (circles). The threshold function values are close to the theory for $\varepsilon = 0.36$ for many cases of CRYSTAL-FACE clouds; the computed threshold function for CSTRIPE DSDs is less than 0.3, very often with values less than 10^{-1}. This suggests that such clouds are far away from a precipitating state, and is consistent with the timescale analysis of Section 4.6. Figure 33 presents predictions of autoconversion using LD6 (with and without the threshold function) against the KCE computations. Considering the threshold function decreases the autoconversion rate (mostly for the CSTRIPE clouds furthest away from a precipitating state), but the changes are not significant in high autoconversion rates for CRYSTAL-FACE (since the value of the threshold function is close to unity). The reduction of autoconversion using the threshold function is sometimes large enough to result in an underestimation of autoconversion, especially for CSTRIPE clouds.

4.5.2 Accuracy of Long's approximate polynomial

It is important to quantify the uncertainty introduced in calculated coalescence (and autoconversion) rate from using the polynomial approximation to Long's gravitational collection kernel. This is shown in Figure 34, which presents total coalescence (top panel) and autoconversion rate (bottom panel) calculations using explicit gravitational collection and approximate polynomial kernels, for CRYSTAL-FACE DSDs. On average, using Long's approximate polynomial overestimates total coalescence

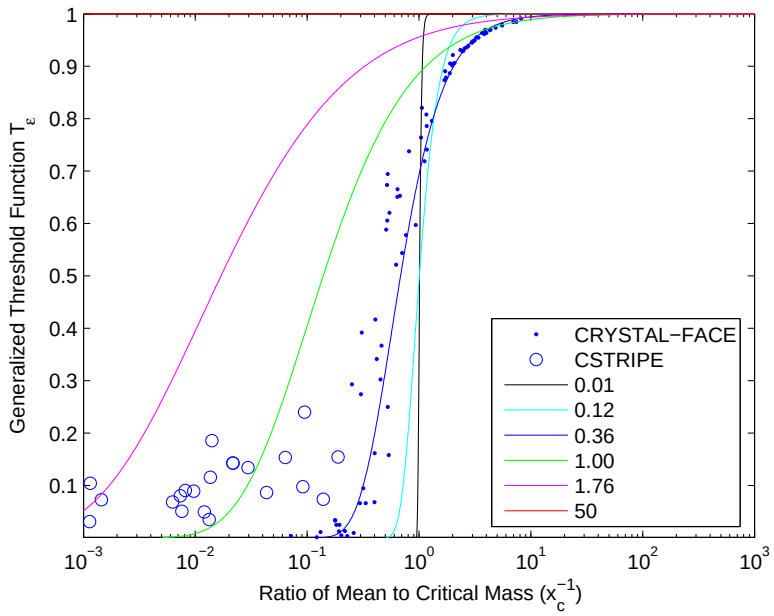

Figure 32: The generalized threshold function of [105]. Lines represent the threshold function for constant ε (values given in legend). Circles and dots represent CRYSTAL-FACE and CSTRIPE DSDs, respectively.

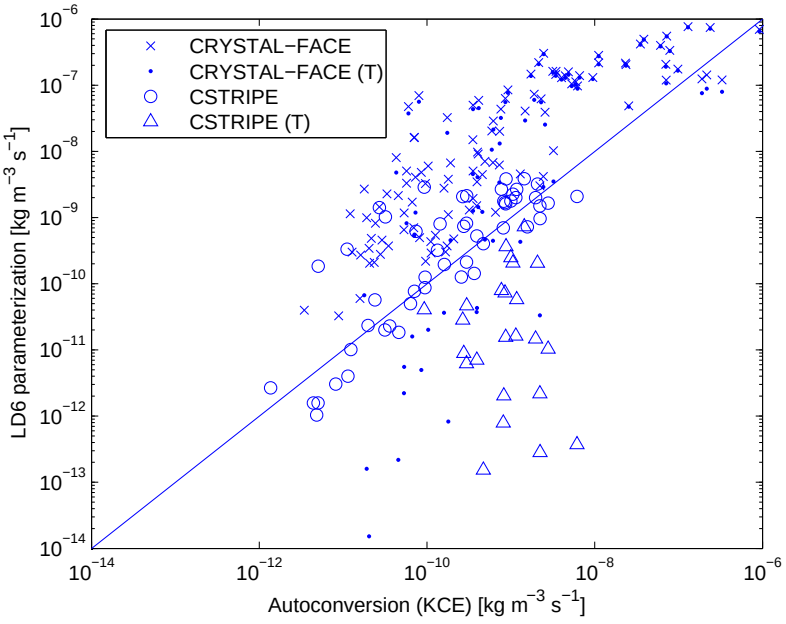

Figure 33: Comparison of autoconversion rate (kg m^{-3} s^{-1}) between LD6 parameterization and KCE integration for CRYSTAL-FACE and CSTRIPE DSD. (T) in legends denotes the consideration of threshold function when applying LD6 scheme.

Table 18: Average conversion rates using polynomial approximation and explicit gravitational collection. Relative difference is computed with respect to KCE calculations with r_0=25μm.

Conversion rate	$r_0 = 20$ μm	$r_0 = 25$ μm	Relative Difference
Coalescence	12.33	12.21	0.11
Autoconversion	0.32	2.35	-0.86
Self-collection	13.14	12.18	0.76

rate by up to a factor of 13, and 32% for autoconversion. These deviations are most prominent at low conversion rates, while the agreement at higher values (most relevant for precipitation) is quite good.

4.5.3 Effect of drizzle threshold size, r_0

The large discrepancy of autoconversion rate between parameterizations may in part be from the separating size used to distinguish cloud droplets from drizzle drops. In this section, we analyze the effects of changing r_0 from 20 μm (as suggested by [173] to 25 μm [87] for DSDs observed in CRYSTAL-FACE clouds. The calculations were done based on Long's gravitational collection kernel, the results of which are summarized in the first two columns of Table 18. As compared to the calculation with $r_0 = 20$ μm, the relative difference of autoconversion rate could increase to 235 % when $r_0 = 25$ μm is used. In general, lower autoconversion rates are obtained for $r_0 = 25$ μm but a slightly higher value for coalescence (Figure 35). The relative difference for autoconversion rate is up to -86 % and 11 % for total coalescence (Table 18). Compared to coalescence, changes in autoconversion are subject to significantly more more scatter (Figure 35), suggesting that the effect of r_0 on collection may not be monotonic.

4.6 Autoconversion error for hydrologically sensitive clouds

Autoconversion rates vary over five orders of magnitude in the CRYSTAL-FACE and four orders of magnitude for CSTRIPE data sets. Not all of this dynamic range

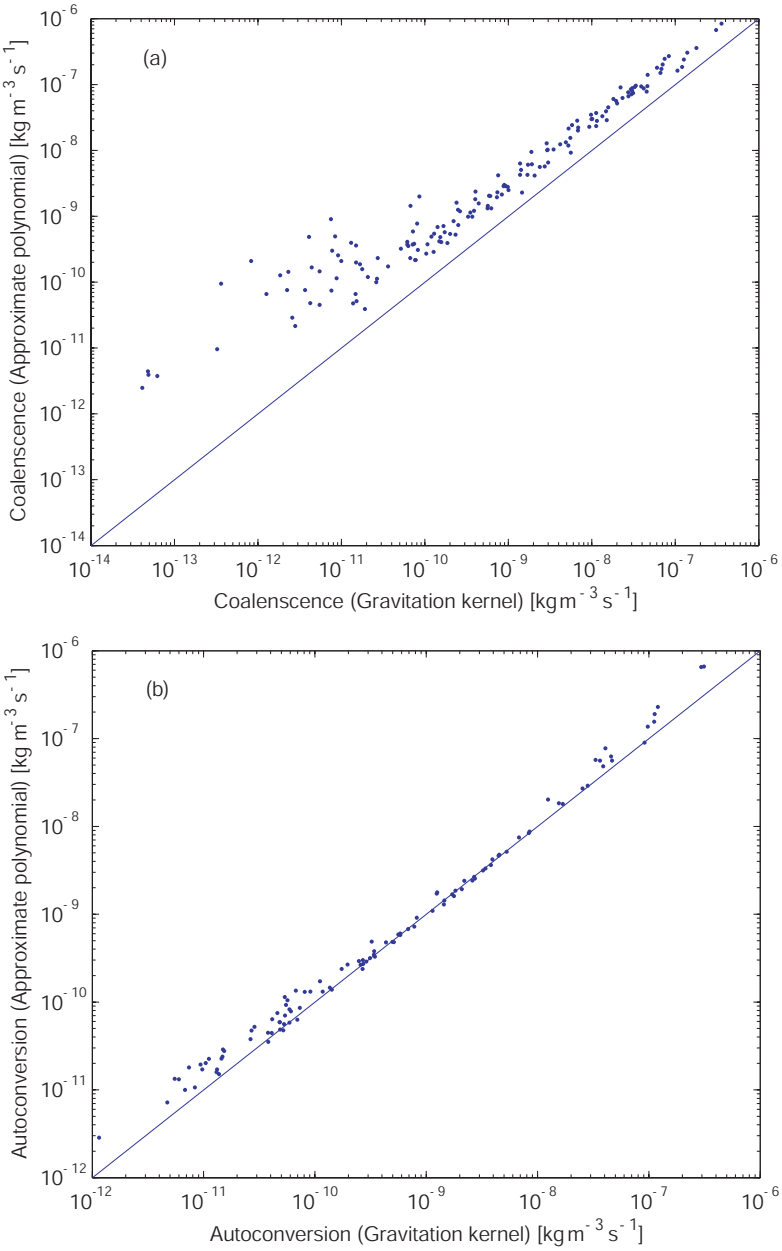

Figure 34: Comparison of (a) coalescence and (b) autoconversion rate between polynomial approximation and explicit gravitational collection kernel for CRYSTAL-FACE DSDs.

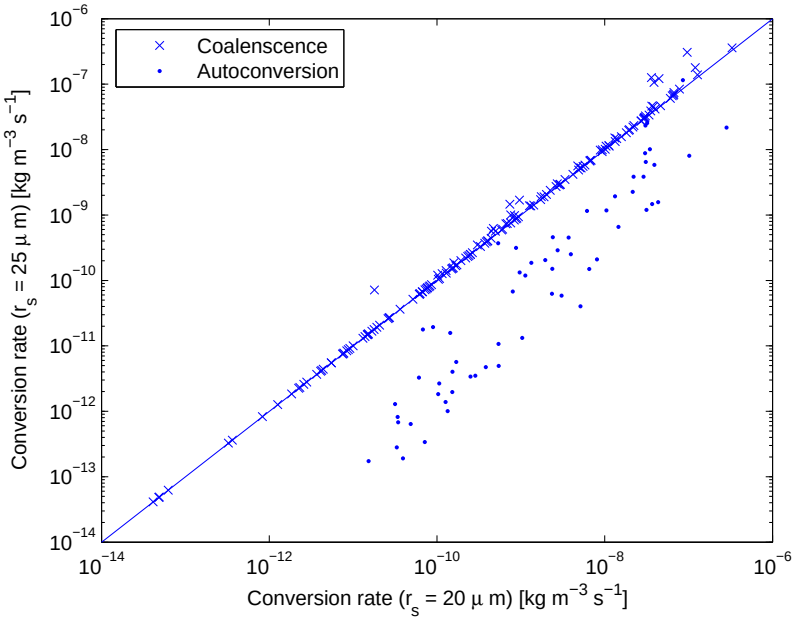

Figure 35: Comparison of conversion rate (kg m^{-3} s^{-1}) between $r_0 = 25$ μ m and $r_0 = 20$ μ m for CRYSTAL-FACE DSDs.

is "hydrologically important" (as noted in Section 4.3.2) so we focus the evaluation for clouds closest to forming drizzle. The evaluation is done by computing τ_{auto} for each observed DSD, using the parameterized and KCE-computed values of autoconversion. Results of this intercomparison for CRYSTAL-FACE and CSTRIPE clouds are shown in Figures 36a and 36b, respectively. τ_{auto} ranges from 0.5 to 10^4 h in cumulus (CRYSTAL-FACE) and 10 to 10^4 h for stratocumulus clouds (CSTRIPE). The CSTRIPE data tend to exhibit larger τ_{auto}, consistent with the lower LWC, weaker dynamical forcing, and low cloud top height. In this study, the "hydrologically important" clouds are those with τ_{auto} less than the typical cloud lifetime, multiplied by a factor of ten to account for the order of magnitude uncertainty associated with autoconversion parameterizations. Thus, for CRYSTAL-FACE clouds, τ_{auto} ranges between 0.1 and 10 h; for CSTRIPE data, τ_{auto} ranges between 0.1 and 100 h. Compared to KCE, application of LD6 tends to underestimate τ_{auto} (because autoconversion rate is overestimated) and they differ by a factor of is about 0.79 $\pm$

1.00 for CRYSTAL-FACE and 0.18 ± 0.74 for CSTRIPE clouds (Table 17). In terms of the other parameterizations, the difference is larger than a factor of 2 for KK and BH in CRYSTAL-FACE clouds and KK, LD4, MC, BH, and SD-L for CSTRIPE cases. LD6 with threshold function, LD6(T), has the lowest error in τ_{auto} and this is consistent with its good agreement in autoconversion rate (Table 17). Among the formulations applied, the standard deviation of A (or τ_{rain}), is of order of the error in τ_{rain} (Table 17). Given that was seen in all parameterizations studied, regardless of their sophistication, this finding may suggest that "tuning" of parameterizations to minimize the average τ_{rain} error (instead of A or LWC), may be accompanied by a strong reduction in prediction scatter, and be an efficient way to improve autoconversion predictions in GCMs.

4.7 KCE with turbulent kernel

LD6 and other parameterizations have been derived assuming that gravitational setting under "quiescent flow" conditions govern droplet collision. However, it is well known that turbulence can affect droplet growth and enhance collision coalescence process [132, 177]. We compare autoconversion rates using KCE with a gravitational kernel, and KCE with a kernel enhanced by turbulent coalescence. In this study, the effect of turbulence on the droplet collection process is represented by application of two collection kernels, by *i*) [180], and, *ii*) [11, 12]. Both kernels are derived from direct numerical simulation (DNS) of droplet collection in a turbulent field. As a result, both kernels are developed for much lower Reynolds number than expected in ambient clouds. [177] showed that the kernel of [180] severely overestimate the effects of turbulence at the very high Reynolds number expected in ambient clouds; nevertheless, we include it in our assessment, to serve as an upper limit of the effect of turbulence on droplet collection.

4.7.1 The [180] turbulence kernel

The collection kernel is of the form:

$$K_t(r_1, r_2) = E_t \Gamma_0 \left[1 + 15 \frac{w_r^2}{v_k^2} \left(\frac{\eta}{R}\right)^2\right]^{1/2} g_{12}(R) \tag{80}$$

where $R = r_1 + r_2$, $\Gamma_0 = (8\pi/15)^{1/2} R^3 v_k(R/\eta)$, $g_{12}(R)$ is given by [180], and, r_1, r_2 are radii of the droplets involved in the collision. $v_k = (ve)^{1/4}$ is the Kolmogorov velocity scale, v is the kinematic viscosity of the fluid and e is the turbulent dissipation rate. $\eta = (v^3/e)^{1/4}$ is the Kolmogorov length scale, and, E_t is the turbulent collection efficiency (assumed to be unity) [136]. Also,

$$\begin{aligned} \frac{w_r^2}{v_k^2} = \; & C_w(\phi) \left(\frac{u'}{v_k}\right)^2 \frac{\gamma}{\gamma - 1} \left\{(\theta_1 + \theta_2) - \frac{4\theta_1\theta_2}{\theta_1 + \theta_2} \left[\frac{1 + \theta_1 + \theta_2}{(1+\theta_1)(1+\theta_2)}\right]^{\frac{1}{2}}\right\} \cdot \\ & \left\{\frac{1}{(1+\theta_1)(1+\theta_2)} - \frac{1}{(1+\gamma\theta_1)(1+\gamma\theta_2)}\right\} \end{aligned} \tag{81}$$

where $\theta_i = \frac{2.5\tau_{pi}e}{u'^2}$, i (=1,2) is the index for droplets involved in the collection, and, u' is the root mean square velocity fluctuation in the flow. $C_w(\phi)$, γ and ϕ are given by [180]. $\tau_p = 2\rho_i r_i^2/(9v\rho)$ is the droplet inertial response time, and ρ_i, ρ is the particle and air density, respectively.

Equation (80) is developed in the absence of gravitational collection. To compute collection rates in the presence of both gravity and turbulence, we add Equation (80) to the gravitational kernel of Long ([110]).

4.7.2 The [11, 12] turbulence kernel

The kernel of [11, 12] considers simultaneously the effects of gravity and turbulence on collection,

$$K_t(r_1, r_2) = 2\pi R^2 \langle |w_r(R)| \rangle \, g_{12}(R) E_{12}^g \tag{82}$$

where $\langle |w_r| \rangle$ is the radial relative velocity and E_{12}^g is the collision efficiency of droplets with radii r_1, r_2 in a quiescent background air. The radial distribution function at

contact, $g_{12}(R)$, is given by [11, 12]. The effects of turbulence on geometric collision kernel is only considered; turbulent effects on collision efficiency is not included because efficiency data is not available for the dissipation rates relevant for ambient clouds. Gravitational collection efficiency is obtained from the Hall kernel, and, terminal velocities of droplets are determined by the nonlinear drag. $\langle |w_r| \rangle$ is expressed as [11, 12],

$$\langle |w_r| \rangle = \sqrt{\frac{2}{\pi}} \sigma \left[\frac{1}{2} \sqrt{\pi} \left(b + \frac{0.5}{b} \right) erf\left(b\right) + \frac{1}{2} \exp\left(-b^2\right) \right] \tag{83}$$

The variance of the relative velocity fluctuation, σ^2, is given as

$$\sigma^2 = \left\langle \left(v_1'\right)^2 \right\rangle + \left\langle \left(v_2'\right)^2 \right\rangle - 2 \left\langle \left(v_1' v_2'\right) \right\rangle \tag{84}$$

where v_1' and v_2' are the fluctuational velocity of two colliding droplets in the radial direction. Finally, the parameter b is defined as

$$b = \frac{|v_{t,1} - v_{t,2}|}{\sigma \sqrt{2}} \tag{85}$$

where $v_{t,1}$ and $v_{t,2}$ are the terminal velocity of droplets with radius r_1 and r_2, respectively.

4.7.3 Effects of turbulence on collection

K_t requires knowledge of the fluctuational velocity, u', and dissipation rate, e (which express the intensity of the turbulent field surrounding the droplet population). In general, e varies from tens cm^2 s^{-3} for stratus clouds to several hundreds cm^2 s^{-3} for cumuli [132]. Therefore $e = 200$ cm^2 s^{-3} for CRYSTAL-FACE clouds, and, $e = 50$ cm^2 s^{-3} for CSTRIPE clouds are assumed; u' can then be inferred from e using the u' vs. e correlation from studies of [111] and [136]. As pointed out by [170], [136] overestimates u' by a factor of $\sqrt{3}$, thus a correction of this factor is also included.

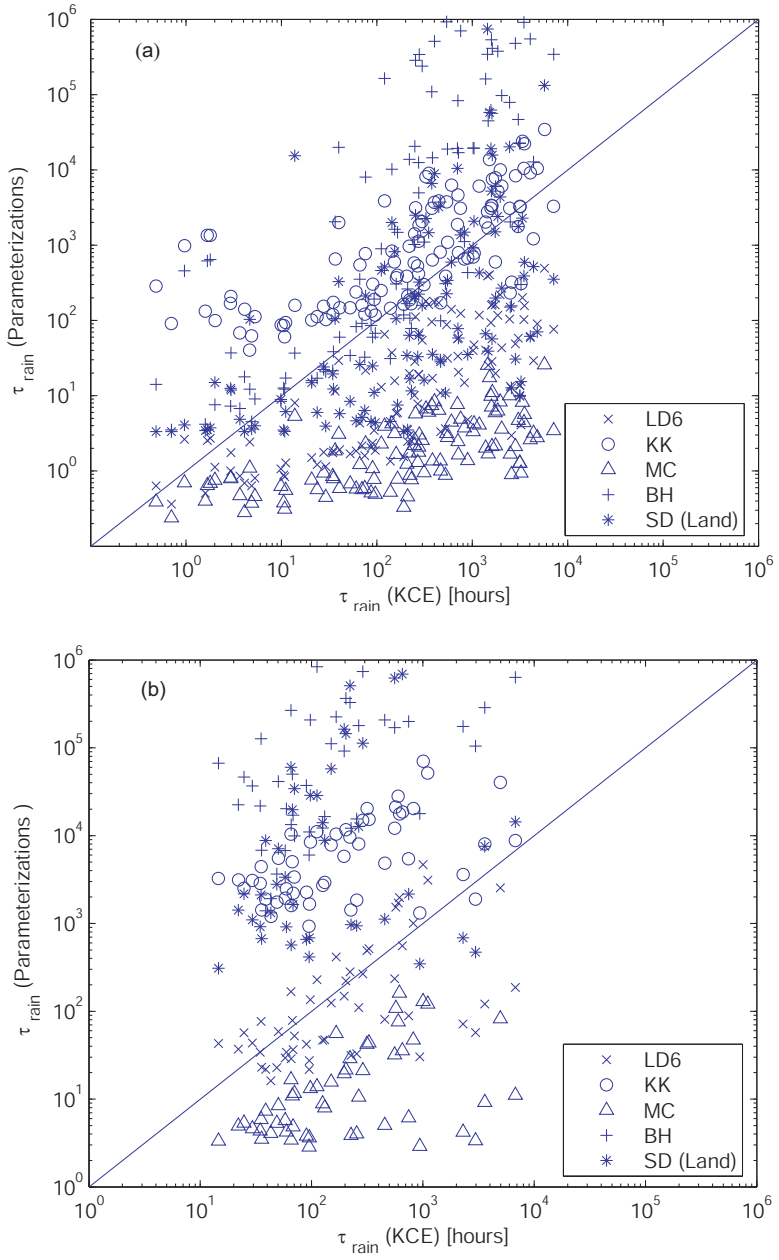

Figure 36: τ_{auto} (Parameterizations) versus τ_{auto} (KCE) for (a) CRYSTAL-FACE and (b) CSTRIPE clouds.

The average u' used for CRYSTAL-FACE clouds is thus 1.73 m s^{-1} and 1.15 m s^{-1} for CSTRIPE clouds.

Figure 37 compares autoconversion rates obtained from KCE integration with gravitational collection under quiescent and turbulent conditions. The Hall kernel is used for gravitational collision process since the [11, 12] kernel is based on the setting of still-fluid terminal velocity and collision efficiency of Hall kernel. Both [11, 12] and [180] kernels are included. For CRYSTAL-FACE cloud size distributions, the average autoconversion rate augmented by the [11, 12] kernel is about a factor of 1.82 $\pm$ 0.09 greater than the average value obtained using the gravitational kernel alone. When applied to CSTRIPE clouds, turbulence enhances autoconversion by a factor of 1.24 $\pm$ 0.01; this difference may be important for clouds for which the time needed for initializing precipitation is slightly longer than its lifetime. When the turbulence kernel of [180] is added to the gravitational kernel, average autoconversion rate increases (compared to a calculation using the gravitational kernel only) by a factor of 3.3 $\pm$ 2.0 for CRYSTAL-FACE clouds, and 3.5 $\pm$ 0.9. Thus, though the kernel of [180] severely overestimates the turbulent kernel [177] and predicts higher autoconversion for the less dissipating CSTRIPE clouds, the effect on autoconversion is about a factor of two different from using the more atmospherically relevant kernel of [11, 12]. For the hydrologically important clouds in the dataset, turbulence (using the kernel of [11, 12]) enhances autoconversion on average by approximate 96% for CRYSTAL-FACE and 24% for CSTRIPE clouds. Although important, the effect of turbulence tends to lie within the inherent uncertainty of autoconversion parameterizations.

4.8 Computational Requirements of KCE

Assuming that the parameterization - KCE autoconversion discrepancy is representative of the parameterization (process) error, one can use KCE as a benchmark

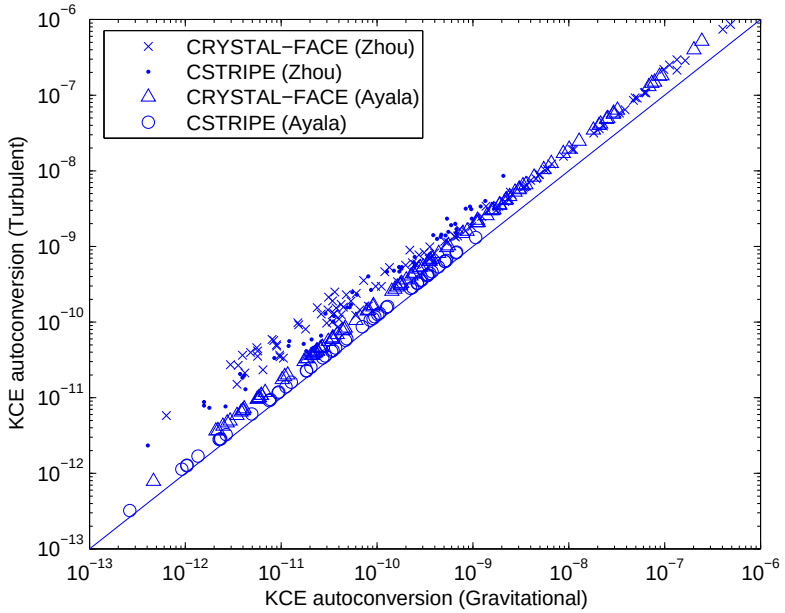

Figure 37: KCE autoconversion rates (kg m^{-3} s^{-1}) using turbulent and quiescent conditions, for CRYSTAL-FACE and CSTRIPE DSD.

calculation. Although expensive for usage in a GCM simulation, KCE can be substantially accelerated if precalculated lookup tables are used for $K(r_1, r_2)$, in place of an online calculation. To evaluate the potential speedup and the impact of using discretized kernels on the calculation, we compare A predicted from KCE (with a lookup table where droplet radii range from 1 to 100 μm with an increment of 1 μm) vs. A from KCE with online calculation of collection kernels. The time needed for computing A from KCE integration is then evaluated for all CRYSTAL-FACE clouds (a total of 164 spectra). Each KCE calculation is executed for all DSDs from CRYSTAL-FACE, and the average time per computation is compared against that required for LD6; the computational platform used for the intercomparison was done in Matlab run on an Intel Pentium-4 2.40 GHz PC running the Windows XP operating system. The total execution time for computing A with KCE calculation includes the procedure of fitting the size distributions and the discretization of the resulting droplet distribution into the droplet bins. Table 19 displays the CPU times of all

Table 19: CPU time required for computing autoconversion using LD6 (only rate function and both rate and threshold function considered) and KCE integration with lookup tables for collection kernel.

	CPU time(s)	
Calculation Method	All executions (164)	Average
KCE (Pre-process kernel)	5.89	3.59×10^{-2}
LD6	2.48	1.51×10^{-2}
LD6 (with threshold function)	2.66	1.62×10^{-2}

calculations; KCE integration with a lookup table for kernels is $\sim$ 2.4 times slower than LD6. Including threshold function for LD6 has the effect to increase computation time, but to a small extent. On average, LD6 with threshold function included is about a factor of 1.07 slower than LD6, but a factor of $\sim$ 2.2 faster than KCE integration. This suggests that application of KCE may be computationally feasible in large scale models, at least for studies that explicitly resolve cloud droplet spectra. Prescribing ε and obtaining N and LWC from an online simulation may further speedup LD6 by a factor of 2.

4.9 Conclusions

This study evaluates assumptions used in autoconversion parameterization development, by comparing them against predictions of the Kinetic Collection Equation (KCE) applied to ambient cloud droplet size distributions collected during the CRYSTAL-FACE and CSTRIPE field campaigns. First, the P6 parameterization of [103] is compared against KCE calculations for gamma distribution fits to the ambient data; both are in excellent agreement for total coalescence. This agreement is largely preserved even when the ambient droplet distribution data is used in the KCE calculation. This means that a gamma distribution provides a good approximation to ambient distributions for calculations of total coalescence, and, the polynomial collection kernel (used in the analytical integration of the KCE) is a good approximation

to the full formulation.

The error in autconversion from fitting a gamma distribution to the data is also assessed. This is done by comparing KCE calculations of autoconversion, using the observed droplet distributions vs. their gamma distribution fits. The error from the fitting is much greater than for coalescence rate and most of this uncertainty arises from the deviations in the fitted distribution, especially for droplet sizes that are close to the drizzle-drop separation threshold. This suggests that higher moments of the DSD (like skewness) may need to be accounted for an effective parameterization of the autoconversion process, in a way so that errors in the fitted distribution are minimized in the region near the drizzle-drop separation size.

KCE calculations of autoconversion rate are also compared against parameterizations currently used in models. Of all parameterizations that consider droplet number, the formulation of [87] on average gives the lowest error and scatter for CRYSTAL-FACE clouds, the latter of which is still substantial ($\sim$ 1 order of magnitude). When the parameterizations are used to predict autoconversion timescale, τ_{auto}, LD6 has the lowest average error. Multiplying LD6 with a threshold function has a minor impact on predicted autoconversion rate for CRYSTAL-FACE clouds, and, a major impact on CSTRIPE clouds. This is consistent with time scale analysis that most of CSTRIPE clouds are far from precipitating state. For higher autoconversion rates in CRYSTAL-FACE clouds, the threshold function is close to unity, consistent with the small autoconversion timescale associated with these clouds.

We also explore the sensitivity of predicted autoconversion to the droplet size threshold used for separating cloud droplets from drizzle. Varying r_0 from 20 to 25 μm radius affects autoconversion to within a factor of two, and the predicted autoconversion rates tend to be lower when using 25 μ m. Overall, the autoconversion difference rising from ambiguity in r_0 is considerably smaller than the inherent scatter of all parameterizations examined.

We also assess the importance of including turbulence effect in KCE calculations of autoconversion rate. Neglecting the turbulent collection process can introduce systematic biases in autoconversion calculations, as enhancement from turbulence is on average by a factor of 1.82 in CRYSTAL-FACE, and, 1.24 in CSTRIPE clouds using the most realistic kernel of [11, 12]. This difference, although within the inherent uncertainty of autoconversion parameterizations, may be important for clouds close to forming precipitation. Surprisingly, collection enhancement from turbulence may be less sensitive to the kernel used as previously thought. Using the kernel of [180], which is known to substantially overestimate turbulence collection for conditions found in clouds, enhances autoconversion rate by roughly a factor of 3 and can be considered an upper limit in enhancement from turbulence.

Finally, we evaluate the computational efficiency of KCE against autoconversion parameterizations. We find that using lookup tables, in place of online calculation of collection kernels result in a considerable acceleration of SCE calculations, which become roughly 2.5-4 times slower than application of the LD6 parameterization. This, together with the substantial predictive uncertainty of current autoconversion parameterizations, suggests that direct KCE integration could be included in studies of the aerosol indirect effect.

CHAPTER V

IMPACTS OF AUTOCONVERSION SCHEMES ON THE AEROSOL INDIRECT EFFECT

Note: This chapter will be submitted to J. Geophys. Res.

5.1 Abstract

The NASA GISS II' GCM, with online simulation of aerosol and cloud droplet number is used to assess the sensitivity of climate and aerosol indirect effects to the approach used for computing autoconversion of cloud water to rain, which are four autoconversion parameterizations, and direct integration of the kinetic collection equation (KCE). In the latter, the relative importance of gravity and turbulence on droplet collection is examined; two collection kernels with substantially different sensitivity to turbulence are considered. Simulations show that Liquid Water Path (LWP) correlates with aerosol loading, because of decreased autoconversion rate. The spatial distribution of indirect forcing is consistent with simulated changes in LWP between preindustrial and present day simulations. The combined first and second indirect effect is quite sensitive to the autoconversion scheme used, varying between -1.30 and -2.05 W m^{-2} when parameterizations are used, and, -0.87 to -1.03 W m^{-2} when the KCE is used.

5.2 Introduction

Autoconversion (the conversion of recently activated cloud droplets into drizzle) and accretion (conversion of drizzle into rain) are the processes used in general circulation models (GCMs) to represent the formation of rain from large-scale warm clouds. Incomplete representation of these processes, especially autoconversion, is a major

source of uncertainty in estimates of the indirect effect of aerosols on climate [108]. While explicit resolution of the droplet collection process could partially resolve this issue, this approach is computationally very expensive [87, 135]. Instead, computationally efficient parameterizations are used, but these tend to be subject to considerable uncertainty. For example, [172] and [73] applied parameterizations to ambient size distributions observed in clouds and report up to 3 orders of magnitude variability in predicted autoconversion rate. [154] show that the calculated global annual average autoconversion rate, for the same levels of liquid water content and droplet number, can vary by an order of magnitude depending on the parameterization used. This level of autoconversion rate uncertainty affects the predicted in-cloud liquid water content (LWC), hence total cloud cover, precipitation, and cloud radiative forcing (e.g., [107, 80, 117, 116, 127]).

Improving the performance of autoconversion parameterizations is an area of active research. Approaches involve either including explicit descriptions of the droplet size distribution and collection process (e.g., [103]), using spectral-resolving cloud model simulations to derive statistical correlations [87], or optimally applying existing parameterizations for specific cloud types and dynamical conditions (e.g., [74]). It is, however, unclear which approach would improve GCM simulations of the hydrological cycle, in part because the true predictive uncertainty of autoconversion parameterizations and their impact on climate are largely unknown. This uncertainty can, however, be quantified if an appropriate reference autoconversion calculation is established, e.g., the Kinetic Collection Equation (KCE); the deviation of each parameterization can be quantified, and allowed to propagate in a climate model simulation for an impact assessment. As insightful as these sensitivity computations are, they do not necessarily suggest which implementation is more realistic. This can be assessed by using the concept of "autoconversion timescale" (defined as the ratio of the cloud liquid water content to the autoconversion rate) and comparing predictions against

observations of this timescale in real clouds. The goal of this study is to assess: (a) the impact of autoconversion scheme on the predicted spatial and temporal distribution of cloud properties; (b) the sensitivity of predicted aerosol indirect forcing and climate state to autoconversion rate; (c) the importance of unresolved collection processes (such as turbulence) on indirect forcing and climate, and; (d) the realism of each autoconversion scheme as judged by comparison with ambient data.

To address the above questions, a series of simulations are carried out with the NASA Goddard Institute for Space Studies General Circulation Model II' (GISS GCM II'), in which both parameterizations and direct integration of the KCE are used online for computing autoconversion rate and climatic state for "preindustrial" and "present day" conditions. The results of these simulations are then evaluated against observations of large-scale precipitation and autoconversion computed from in-situ cloud observations of droplet size distributions.

5.3 Model description and cloud microphysical processes

The global climate model used in this work is the GISS GCM II' [68], coupled with an online aerosol simulation [7, 6, 89]. The model has $4^\circ \times 5^\circ$ horizontal resolution and nine vertical layers between the surface and 10 mb. Sea surface temperature is prescribed (by climatology) and chemical tracer budgets are simulated online. Radiative absorption by gases and particles is calculated using the correlated k-distribution method [94, 68, 93]; for the solar part of spectrum, six k intervals (one in the visible region and five near IR) are used for the spectral dependence of Mie parameters of clouds and aerosols.

Seasonal emissions of SO_2 from fossil fuel combustion and biomass burning are obtained from the Global Emission Inventory Activity (GEIA) [65], and other reports of industrial emissions [15, 21]. Natural sources include SO_2 from non-eruptive volcanoes [155] and oceanic DMS [100, 85]. Aerosols are assumed to be internally mixed

and composed of sulfate, ammonium, nitrate, methanesulfonic acid, and water. Gas-phase species include dimethyl sulfide, sulfur dioxide, ammonia, and hydrogen peroxide. Aerosol transport processes include emissions, chemical transformation, and wet/dry deposition. Aerosol water content is calculated assuming thermodynamic equilibrium, using the relative humidity, temperature and aerosol concentration in each cell. A thorough description of the modeling framework is given by [154] and references therein.

5.3.1 Computing cloud droplet number concentration

Cloud formation occurs at the sub-grid scale and is represented with parameterizations. The [58] formulation (referred as FN hereafter) is used to compute cloud droplet number concentration (CDNC) from the relevant aerosol size distribution, composition, and cloud-base updraft velocity. FN is based on the framework of an ascending adiabatic cloud parcel, and the maximum supersaturation, s_{max} is determined by the balance of water vapor availability from cooling and depletion from the condensational growth of activated droplets. FN uses the concept of "population splitting" to classify droplets according to the proximity to their critical diameter and allows the analytical determination of s_{max}; CDNC is then computed as the number of CCN with a critical supersaturation less than or equal to s_{max}. The accuracy of FN has been evaluated with detailed numerical simulations [58], and with in-situ cloud microphysical observations of cumuliform and stratiform clouds formed in marine and continental airmasses [60, 118]. Aerosol size distributions are not simulated online, but are obtained by scaling prescribed distributions (from observations) to the online simulation of aerosol mass. Two types of aerosol distributions are used: (1) marine, for grid cells over ocean; and (2) continental, for grid cells over land [95]. Cloud-base updraft velocities are also not available online, and are prescribed, as 0.5 m s^{-1} and 1 m s^{-1} for marine and continental grid cells, respectively [154]. Based on the

Table 20: Autoconversion parameterizations considered in this study. [a]

Scheme	Autoconversion rate (kg m^{-3} s^{-1})
MC, [113]	$A_{MC} = \pi\kappa_1 \left(\frac{3}{4\pi\rho_w}\right)^{4/3} EN^{-1/3}L^{7/3}H\left(R_3 - R_{3c}\right)$
KK, [87]	$A_{KK} = 1350 q_c^{2.47}(N \times 10^{-6})^{-1.79}$
R6, [103]	$P_{LD6} = \left(\frac{3}{4\pi\rho_w}\right)\kappa_2\beta_6^6\left(\frac{L}{N}\right)^{2/3} N^{-1/3}L^{7/3}H\left(R_6 - R_{6c}\right)$
SD, [159]	$A_{SD} = C_0 q_c \left\{1 - \exp\left[-\left(\frac{L}{L_c}\right)^4\right]\right\}$

suggestions of [60], the effective water vapor mass uptake coefficient, α_c is set to 0.06.

5.3.2 Computing autoconversion

The parameterization schemes used in this study are summarized in Table 20 and include (a) [159], denoted SD, (b) [103], P6, (c) [87], KK, (d) [113], MC. SD is the formulation used in the GISS GCM II', and, depends exclusively on LWC [159]. The other parameterizations depend, in addition to LWC, on droplet number (P6, KK, MC); P6 also considers the effect of droplet spectral dispersion.

The other approach adopted for computing autoconversion rate is direct integration of the kinetic collection equation (KCE) [132]:

$$A = \int_0^{x_0} \left[\int_{x_0 - x}^{x_0} K(x, x')x'n(x')dx'\right] n(x)dx \tag{86}$$

where A is the autoconversion rate, $K(x,x')$ is the collection kernel, $n(x)$ is the droplet size distribution (DSD), and, x is the droplet mass. x_0 is the droplet mass used to define the drizzle threshold size (typically corresponding to a drop of 20 μm radius).

Equation 86 requires knowledge of the DSD. As the DSD is not computed online, it is assumed to follow a gamma distribution constrained by three cloud properties: (1) cloud liquid water mixing ratio (LWMR) (obtained by dividing the grid-cell cloud

liquid water content by the fractional cloud cover), (2) cloud droplet number concentration (obtained from application of the FN parameterization), and, (3) the droplet distribution relative dispersion, ε (defined as the standard deviation over the average droplet size) [73]. A prescribed value, ε=0.44, is used in this study, based on observed cloud microphysical data obtained during the CRYSTAL-FACE and CSTRIPE campaigns [72]. The distribution is then applied to Equation 86, which is integrated numerically, by discretizing the droplet distribution onto a mass-doubling grid, ranging from 2.1 to 18.8 μm radius over 20 bins [27].

When applied directly to compute autoconversion rate, the P6 scheme and MC tend to give the highest A, and KCE the lowest (e.g., [172, 73]). All other parameterizations lie within the envelope of A values between P6 and KCE [73]; therefore application of the latter two schemes is used to define the range of uncertainty in A within a GCM simulation.

5.3.3 Collection kernels

The collection kernel, $K(x, x')$, which determines the collection rate between droplet collisions (Equation 86), depends on the collection mechanisms active. The two major collection mechanisms are gravitational settling and turbulence. The [67] kernel is used for gravitational collection. [110] provided a polynomial approximation of that kernel which facilitates the analytical integration of the KCE (e.g., [103]), and provides values of A that agree reasonably with those obtained from application of the [67] kernel [73]. [11, 12] expanded the Hall kernel to include effects of both gravitational collection and turbulence, which results in about a 50% enhancment in A for turbulence conditions pertinent to ambient clouds [73]. [180] also proposed a turbulence kernel, and, although it substantially overestimates collection rates, it can be used as an upper limit of the effects of turbulence.

All turbulence kernels require knowledge of the in-cloud fluctuational velocity (u')

and dissipation rate (e), values of which are prescribed separately for marine and continental clouds. For consistency, u' is set to the same updraft velocity used for calculation of cloud droplet number; e can be computed from turbulent kinetic energy (TKE), k,

$$e = (k)^{(3/2)}/l \tag{87}$$

where l is the eddy length scale, related to the size of the flow domain, L, by $l = 0.07L$ [136] we assume $L = 1500$ m to reflect the typical thickness of the atmospheric boundary layer. Based on the k-e model, u' and k are related by $u' = ck^{1/2}$, where c is an empirical scaling constant, typically set for atmospheric flows to 0.7 [132, 107]. Thus, for the values of u' and L considered, e is equal to 34.7 $\mathrm{cm^2 s^{-3}}$ over ocean and 277.7 $\mathrm{cm^2 s^{-3}}$ over continents.

The potential impact of turbulence on the droplet collection kernel can be seen in Figure 38, which shows the turbulent enhancement factor (defined as the ratio of the turbulent and gravitational collection to gravitational collection alone, i.e., the Ayala kernel over the Hall kernel) for droplet radii ranging between 1 and 20 μm, and turbulence conditions calculated for marine (e =34.7 $\mathrm{cm^2 s^{-3}}$) and continental (e =277.7 $\mathrm{cm^2 s^{-3}}$) clouds. In general, the enhancement factor increases with size of the colliding droplets; continental conditions (i.e., lager e) produce up to a factor of two larger enhancement than for marine conditions. The ratio exhibits a local maximum when both colliding droplets approach the same size (i.e., $r_2 = r_1$), where gravitational collection becomes relatively inefficient. Because of this, an upper limit of turbulent enhancement can be approximated by the enhancement factor at r_1=r_2=r_{max}, where r_{max} is the droplet size at the peak of the size distribution (approximately equal to the average droplet size). For droplets ranging between 10-20 μm (i.e., sizes below the typical drizzle threshold), this upper limit ranges 10-30% for marine, and, 50-300% for continental clouds. KCE integrations for ambient cloud droplet size distributions by [73] confirms the validity of this estimate.

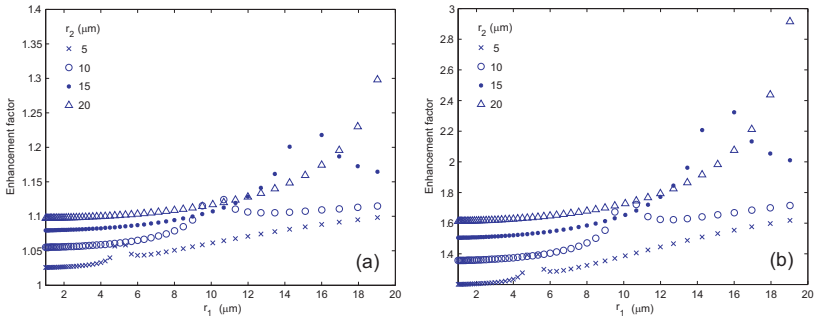

Figure 38: Turbulent enhancement factor for kernels corresponding to (a) marine (ε =34.7 cm^{2}s^{-3}) (b) continental (ε =277.7 cm^{2}s^{-3}) clouds.

5.3.4 Simulations considered

The simulations carried out are summarized in Table 21. Each autoconversion formulation is implemented in the GCM and a pair of 6-year simulations is carried out for each, one using "present day" and one using "preindustrial" aerosol emissions. Output from the last 5 years of each simulation is then analyzed. The reference case (REF) uses the SD scheme (the GISS "default" autoconversion parameterization). The other simulations use P6, KK, and MC parameterizations ; in the P6 and MC simulations, a threshold radius of 7.5 μm is taken for initiating autoconversion [142]. For the TUR and GRV simulations, autoconversion rate is computed based on direct integration of KCE (Section 5.3.2); TUR uses the Ayala kernel for expressing collection under the influence of turbulence and gravitational settling, while GRV uses the Hall kernel, which expresses collection for gravitational settling only. To accelerate the KCE calculations, the collection kernels are precalculated offline and saved as two-dimensional lookup tables with respect to r_1 and r_2. Given the large uncertainty in quantifying turbulence effects on droplet collection, we carry out a sensitivity study using an alternative turbulence collection kernel, developed by [180], discussed in Section 5.4.4.

Table 21: Simulations considered.

Simulation	Method for computing autoconversion
REF	SD parameterization (Reference run)
P6	R6 parameterization
KK	KK parameterization
MC	MC parameterization
TUR	KCE, Ayala kernel (turbulence and gravitational effects on collection).
GRV	KCE, Hall kernel (gravitational effects on collection).
TURZ	KCE, Zhou kernel (turbulence and gravitational effects on collection).

5.4 Results and discussion

5.4.1 Effects of microphysical schemes on present-day LWC and CDNC

We first compare autoconversion rates between simulations for present-day emissions. Figure 39 shows the annual mean global distribution of autoconversion rate in the first vertical GCM layer. All autoconversion parameterizations predict higher autoconversion than using KCE; the SD formulation (REF simulation) falls in the mid range of values (global annual average value 26.17×10^{-10} kg m^{-3} s^{-1}). The P6 parameterization gives on average a factor of 2.1 larger autoconversion rate than REF, and KK, a factor of 2 lower. The spatial variability of autoconversion rate is relatively small for REF, since autoconversion depends only on LWC; P6, MC and KK schemes give much larger spatial variability as a result of their dependence on droplet distribution parameters. The P6 simulation exhibits the largest spatial variability and average autoconversion rate.

Table 22 summarizes the annual global mean cloud and meteorological properties for all simulations of Table 21 using present day aerosol emissions. The global average LWP ranges from 93 g m^{-2} for the REF to 124 g m^{-2} for the GRV simulation. All other autoconversion schemes, compared to REF, give an increase in LWP. This is easily understood for schemes that have a lower autoconversion rate (KK, TUR, GRV; Figure 39) because of the reduced water removal rate. P6 and MC, although

Table 22: Annual global mean cloud and meteorological properties for simulations conducted in this study, using present day emissions.

Simulation	REF	P6	KK	MC	TUR	GRV
CDNC (cm^{-3})	99.3	93.9	96.8	93.9	93.3	92.9
r_e (μm)	8.5	8.9	9.1	8.8	9.2	9.2
Cloud Optical Depth	8.8	9.7	10	9.5	10.4	10.4
Net downwelling SW flux at TOA ($W\ m^{-2}$)	238.7	233.1	235.8	233.3	231.7	232.1
Precipitation ($mm\ day^{-1}$)	3.040	3.048	3.042	3.053	3.048	3.038
Liquid water path ($g\ m^{-2}$)	93.5	116.9	105.4	115.6	124.7	124.0
Total cloud cover (%)	46.7	48.4	47.8	48.4	48.9	48.7
Low level cloudiness (%)	34.4	36.1	35.7	36.1	36.8	36.5
Middle level cloudiness (%)	14.5	14.6	14.5	14.6	14.6	14.6
High level cloudiness (%)	14.1	14.2	14.1	14.2	14.2	14.2

predicting the highest autoconversion rate in the lower levels of the GCM, are surpressed at the higher layers because the effective radius (r_e) of liquid clouds is below the threshold of 7.5 μm. As a result, the amount of water removal for the entire column is still less than that with REF (Figure 40).

The predicted global mean cloud droplet number concentration in the first model layer is the highest (99.3 cm^{-3}) for REF, and varies roughly 2-6% for the others mostly from the enhanced wet scavenging of aerosol associated with the increased LWP (Figure 40). Compared to REF, the change in total cloud cover in P6 (3.5 %) is larger than KK (2.3 %) and TUR is the highest (4.6 %). Changes in total cloudiness are mostly related to changes in low-level cloudiness, where autoconversion has the largest impact on the hydrological cycle (because of the frequency with which large-scale warm clouds occur).

5.4.2 Influence of autoconversion scheme on precipitation

Figure 42 shows the zonal annual means of precipitation, liquid water path, total cloud cover and low level cloudiness from REF, and relative differences from REF for all other simulations. Presented also are observations of precipitation obtained from the NOAA Climate Prediction Center Merged Analysis of Precipitation (CMAP;

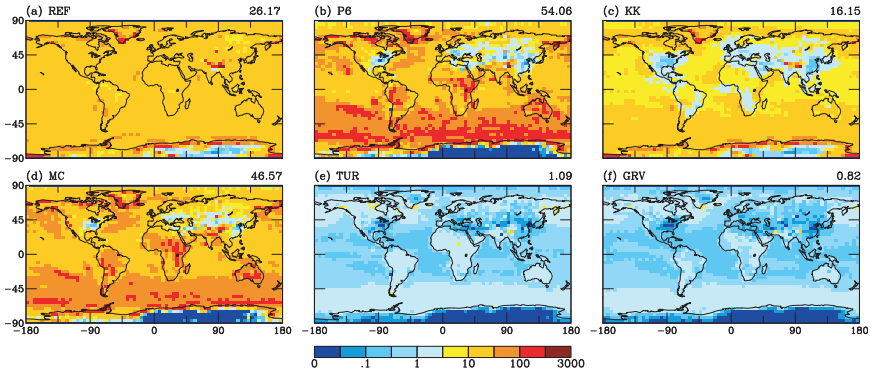

Figure 39: The global distribution of annual average present-day autoconversion rate (in unit of 10^{-10} kg m^{-3} s^{-1}) in the the first model vertical layer, for (a) REF (b) P6 (c) KK (d) MC (e) TUR and (f) GRV simulations. The global annual average value is presented at the top right corner of each plot.

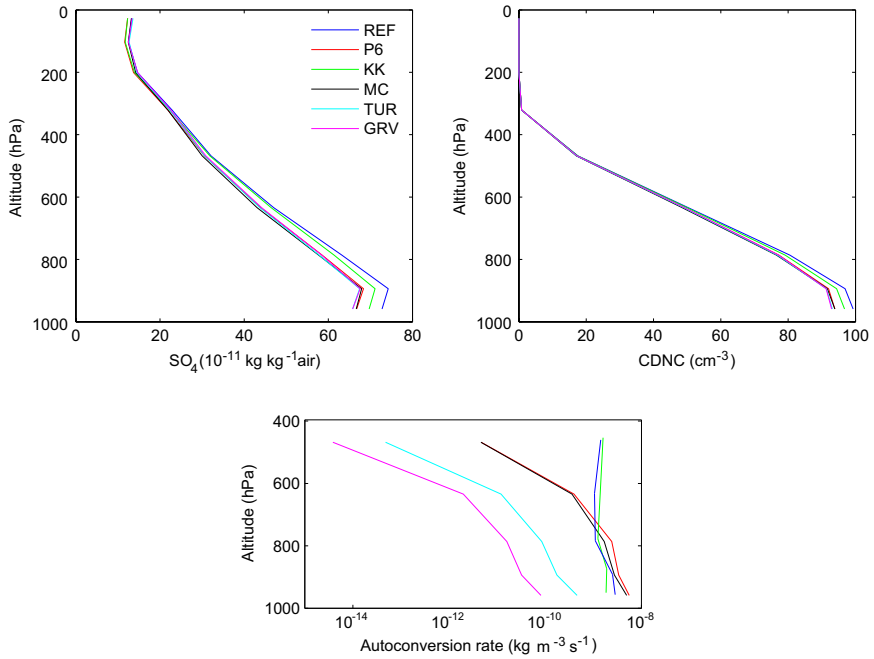

Figure 40: The vertical profile of global annual mean SO_4^{2-}, N_d, and autoconversion rate for present day simulations

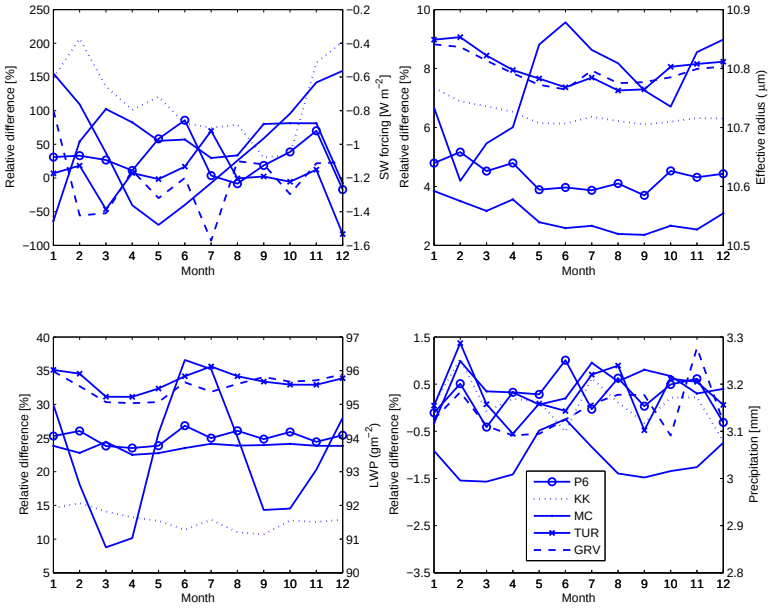

Figure 41: Global, monthly mean relative difference (%) of SW forcing, effective radius, liquid water path, and precipitation. Monthly means are averaged over five years of simulation using present day emissions. Solid line in each plot represent the average values from REF.

http://www.cpc.ncep.noaa.gov/products/global_precip/html/wpage.cmap.html). CMAP is provided at a 2.5° × 2.5° spatial scale, compiled from merged rain gauge observations and satellite-based estimates [176]. We used the 10 year (1980-1989) average for the model comparison . In general, annual mean latitudinally-averaged precipitation is captured by the simulation; the largest rainfall occurs, as expected, in the intertropical convergence zone (ITCZ) where deep convective clouds contribute most of precipitation. The second peak is located in the mid-latitude zone which is the active region for storm tracks and where stratiform clouds contribute most of the precipitation. Furthermore, marine regions are associated with higher precipitation than continents. Compared to the CMAP 10 year average, the GISS model underestimates precipitation in the Tropics by ~ 1.2 mm day^{-1} but overestimation is seen in mid-latitude in both hemispheres. The simulated ITCZ peak shifts to north by $\sim 5°$ where a 10° north shift is predicted in [66]. The GISS model predicts the poleward shift of the secondary precipitation maximum of the storm track in the Southern Hemisphere, and underestimates rain in latitudes greater than 80°S.

Changes in global precipitation for all simulations is relatively small, all agreeing to within 1.5 %. In the P6 run, the global average of annual mean precipitation is 3.048 mm day^{-1} (Table 22), slightly larger than KK and GRV (3.042 and 3.038 mm day^{-1}, respectively). This occurs in part, because using the P6 scheme tends to predict higher autoconversion rate than the latter two [73]. For similar reasons, the MC simulation presents a higher precipitation rate as compared to REF (3.053 mm day^{-1}). The spatial distribution of the annual average difference in precipitation of each simulation with respect to REF is shown in Figure 43. Though relatively small increases are seen in global annual average precipitation, local effects could be substantial, exceeding 1 mm day^{-1} (Figure 43). This implies that uncertainty from autoconversion could result in biases in the simulated precipitation distribution, which could impact the global hydrological cycle. Using different parameterizations

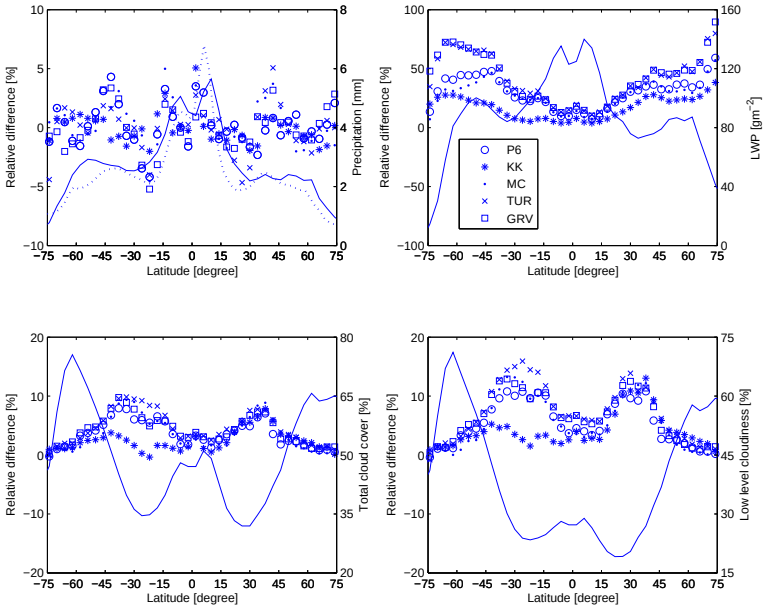

Figure 42: Zonal annual means of precipitation, liquid water path, total cloud cover and low level cloudiness for REF run (scale on the right y-axis, solid line) and relative difference is shown on left y-axis. Observed precipitation from CMAP is also included in left-top plot (dotted line).

or KCE integration for predicting autoconversion rate could cause shifts in the zonal average distribution of rainfall as well.

The global average precipitation rate difference between present day and preindustrial simulation is small, and does not correlate with CDNC or LWP (Table 23); regional variations may be important however.

5.4.3 Influence on the magnitude of the aerosol indirect effect

Table 23 shows the differences in cloud and meteorological parameters between present day and preindustrial conditions. Aerosol indirect forcing is calculated as the change in the net shortwave radiation at the top of atmosphere (TOA) between present day and preindustrial conditions. The changes of LWP and r_e are the largest for the KK simulation and are reflected in the spatial patterns in net outgoing shortwave radiation flux. The global mean r_e in the REF run is 8.6 μm, with global annual

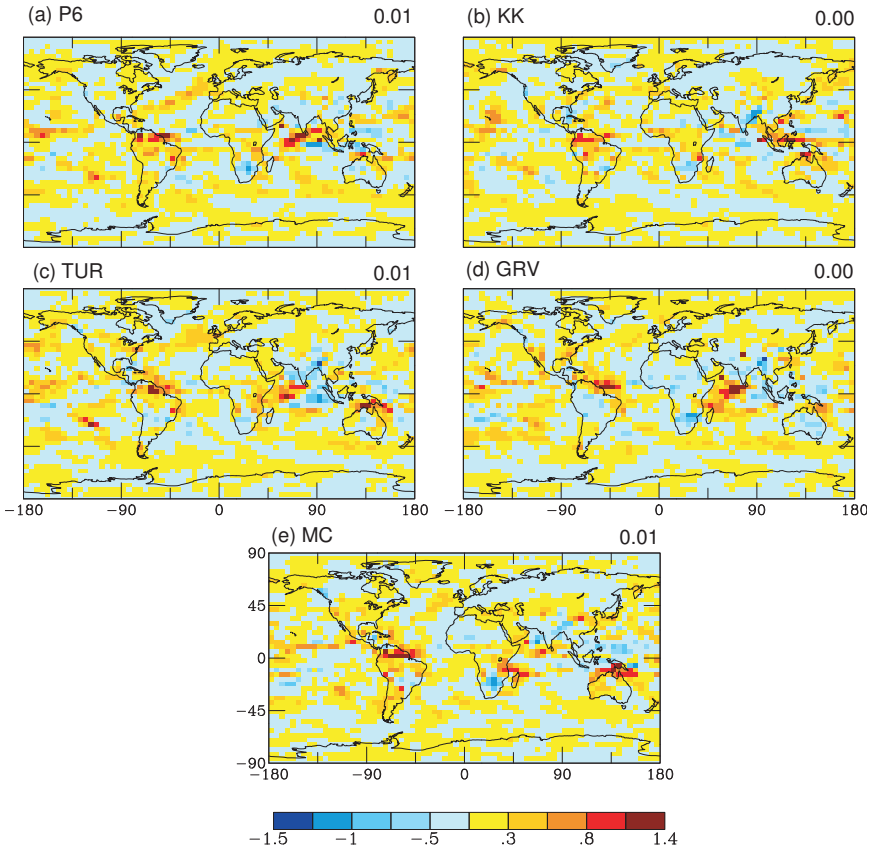

Figure 43: Global spatial distribution of annual mean precipitation difference (mm day^{-1}) with respect to the REF simulation using "present day" emissions. (a) P6, (b) KK, (c) TUR, (d) GRV, and, (e) MC. The global annual average value is presented at the top right corner of each plot.

Table 23: Present day minus preindustrial differences in values of cloud and meteorological parameters (global annual mean) for all simulations conducted in this study.

Simulation	REF	P6	KK	MC	TUR	GRV
CDNC (cm^{-3})	57.3	52.9	55.4	52.9	52.6	52.1
r_e (μm)	-0.5	-0.4	-0.5	-0.4	-0.5	-0.5
Cloud optical depth	0.8	0.9	0.9	0.9	0.8	0.8
Downwelling SW flux at TOA ($W\ m^{-2}$)	-1	-1.3	-2	-1.5	-1	-0.9
Precipitation ($mm\ day^{-1}$)	0	-0.01	-0.006	-0.005	-0.004	0.001
LWP ($g\ m^{-2}$)	0	1.4	4	2.3	0	-0.1
Total cloud cover (%)	0	0.2	0.5	0.3	0.1	0
Low level cloudiness (%)	0	0.2	0.6	0.3	0.1	0
Middle level cloudiness (%)	0	0.1	0.1	0	0	0
High level cloudiness (%)	0	0	0	-0.1	-0.1	0

averages of 8.9, 9.1, and 8.8 for the P6, KK, MC simulations, respectively. The global average relative difference in CDNC between present day and preindustrial simulation ranges from 127.8% for GRV, to 136.5% for REF simulation. Of all simulations, KK exhibits the largest seasonal variability in r_e, changing more than 100% from winter to spring (Figure 41). All "present day" simulations (except REF) show a decrease of r_e with increase of CDNC, accompanied by an increase in LWP. The predicted increase in LWP for the present day simulation is largely a result of enhancements in aerosol number leading to suppressed precipitation. Changes of LWP are also associated with changes in evapotranspiration and transport of water vapor from dynamical feedbacks. The predicted change of total cloud cover between present day and preindustrial simulation is small (but not trivial in terms of aerosol indirect forcing), ranging (in absolute cloud cover) from 0.1 % (TUR) to 0.5 % (KK). No change in LWP, precipitation and macro-scale cloud properties (total cloud cover, high, middle and low level cloudiness) occur in REF, since the effects of aerosols on precipitation rates are not explicitly accounted for. The highest (downwelling) shortwave flux at the top of atmosphere (TOA) is predicted for the REF simulation (238.7 Wm^{-2}), consistent with the lowest predicted LWP.

Annual zonal mean aerosol indirect forcing, changes in cloud droplet number concentration, cloud optical depth and effective radius between present day and preindustrial simulation from REF and relative difference computed based on REF for all other simulations are shown in Figure 44. Aerosol indirect forcing is largest in the mid-latitudes around 50 °N, consistent with high aerosol concentrations. The zonal distribution of the predicted indirect effect is also consistent with changes in droplet effective radius and cloud optical depth. In the mid-latitude region, the difference of r_e, and cloud optical depth between present day and preindustrial simulations are also the largest (Fig. 44). Of all autoconversion schemes considered, KK gives the largest variability in r_e, optical depth and N, likely because KK is most sensitive to N of the schemes considered.

Figure 45 shows the annual mean global distribution of indirect forcing for simulations considered in this study. The predicted aerosol indirect radiative forcing ranges from -0.89 W m^{-2} for GRV to -2.05 W m^{-2} for KK. Throughout most of NH, cooling is predominant in regions of strong anthropogenic influence (e.g., South-East Asia, Western Europe, and Eastern US). As radiative fluxes are sensitive to small changes in the cloud LWP for small LWP [163], the magnitude of aerosol indirect forcing is largely correlated with the LWP change. Figure 46 shows the spatial distribution of LWP difference between present-day and preindustrial simulation for all autoconversion schemes considered (except REF). For the KK simulation, in the regions of largest cooling (South-East Asia, Western Europe, and eastern US), there is also a strong increase of LWP, causing a decline of net shortwave flux at TOA and a cooling effect. Although the overall pattern of indirect forcing is similar for the different microphysical schemes, variations in local areas can be substantial; hence accounting for the feedbacks in precipitation due to aerosols introduces substantial variability in predictions in indirect forcing. For example, positive forcing is predicted in eastern Pacific (west coast of California) for the P6 simulation, however, there is a cooling

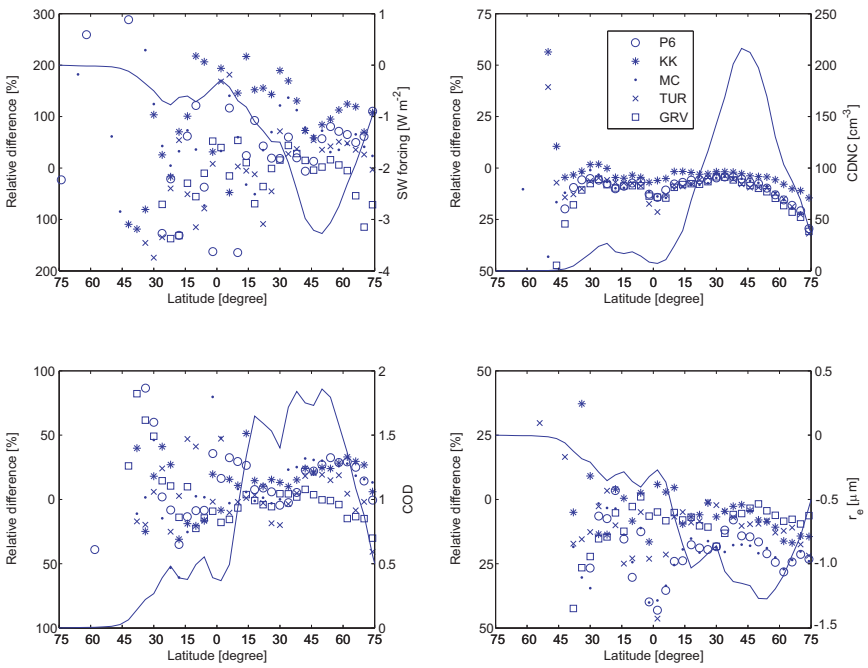

Figure 44: Annual zonal means of top-of-atmosphere shortwave forcing (top-left) and zonal average difference of N_d, cloud optical depth and effective radius between present day and preindustrial simulations for all simulations conducted in this study.

effect in the same region for the KK simulation.

5.4.4 Sensitivity of predicted indirect forcing to collection kernel

In this section, we investigate the sensitivity of LWP, effective radius, and aerosol indirect forcing to the collection kernels used to describe the enhancement in A from turbulence. GCM predictions using the Ayala kernel (TUR simulation, Table 21) are compared against those using the Zhou kernel ([180]), hereafter referred to as "TURZ simulation". Since [180] provides the collection kernel for turbulence only, the combined effects of gravitation and turbulence on droplet collection are obtained by adding the gravitational kernel of [110] to the [180] formulation. In both TUR, TURZ simulations, the turbulence parameters e, u' are applied consistently (as described in Section 2.3).

The large difference between kernels used in TURZ and TUR simulations is shown in Figure 47, which gives isopleths of the (a) Ayala, and, (b) combined Zhou and Long

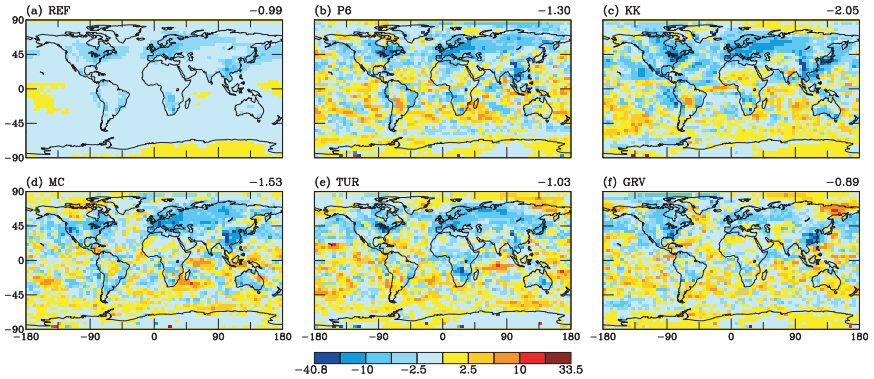

Figure 45: Global distribution of shortwave indirect forcing (W m^{-2}), for (a) REF (b) P6 (c) KK (d) MC (e) TUR and (f) GRV simulations. The global annual average value is presented at the top right corner of each plot.

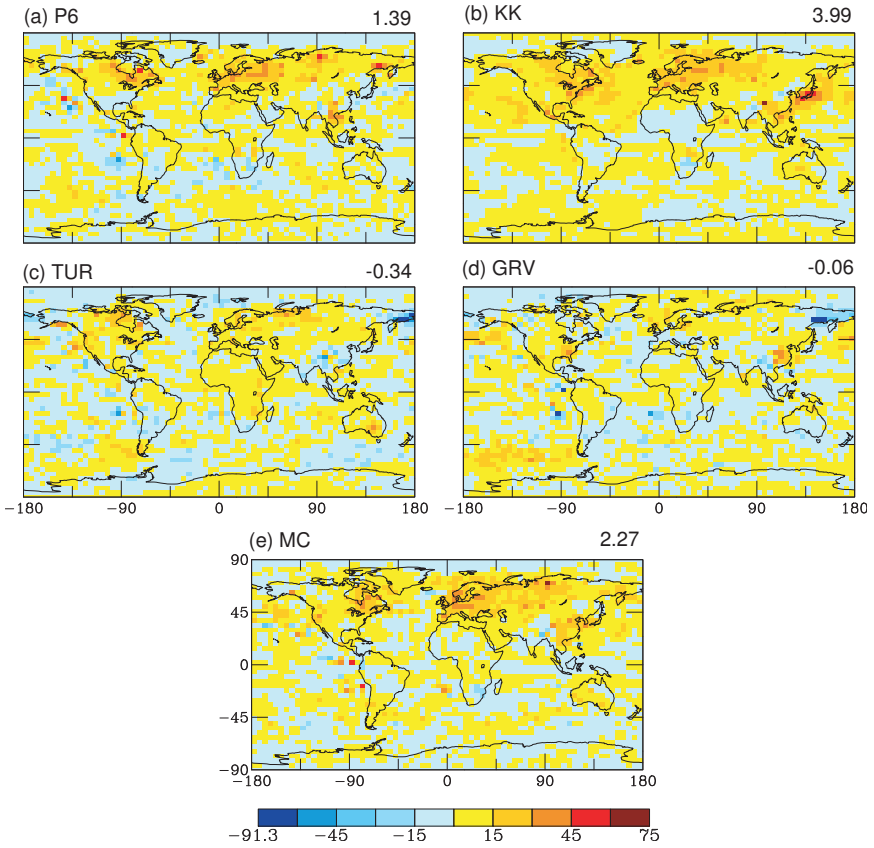

Figure 46: Similar to Figure 43, but for annual average LWP (g m^{-2}).

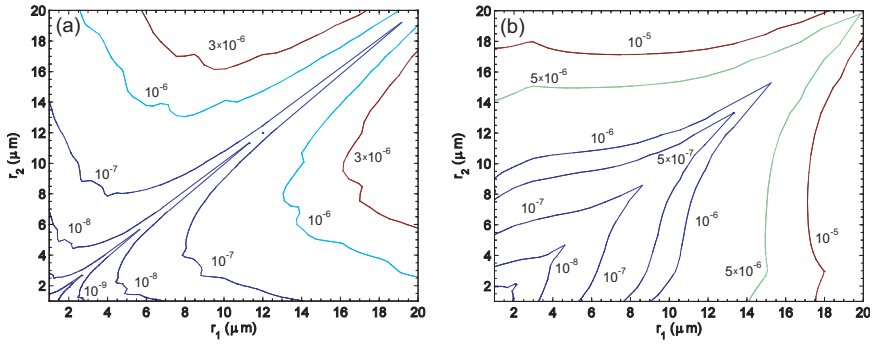

Figure 47: Turbulent collection kernel isopleths (cm^3 s^{-1}) for "marine cloud" turbulence conditions (i.e., e=34.71 cm^2s^{-3}, u' = 0.5 ms^{-1}). Results shown for (a) Ayala kernel (b) combined Zhou and Long kernel.

kernels, computed for "marine cloud" turbulence conditions (i.e., e=34.71 cm^2s^{-3}, u'=0.5 m s^{-1}). For droplet pairs close to threshold size (20 μm), the overestimation of the Zhou kernel could be as large as an order of magnitude. This large difference, however, is not reflected in the computed A, as most collisions occur between droplets of very different sizes; still, a factor of 2-3 difference in autoconversion can result [73]. Figure 48 shows the annual mean global distribution of the surface-layer autoconversion rate (panels a, b), the changes in LWP between present and preindustrial (panels c, d), and shortwave aerosol indirect forcing (panels e, f) for TUR (panels a, c, e) and TURZ (panels b, d, f) simulations. The geographic patterns of autoconversion rate and changes in LWP are similar, the change of global annual mean LWP is -0.36 g m^{-2} and 0.52 g m^{-2} for the Ayala and Zhou kernels, respectively. Spatial distributions of changes of aerosol indirect forcing are consistent with changes in LWP. Compared to simulation with the Zhou kernel, the Ayala kernel produces a stronger negative forcing over the European continent. The estimated shortwave indirect forcing is -1.03 and -0.87 W m^{-2} for Ayala and Zhou kernels, respectively.

5.4.5 Comparison of autoconversion timescale with ambient clouds

We have seen that the range in predicted autoconversion rates in the simulations considered (roughly a factor of 10) lead to about a factor of 2 range in predicted

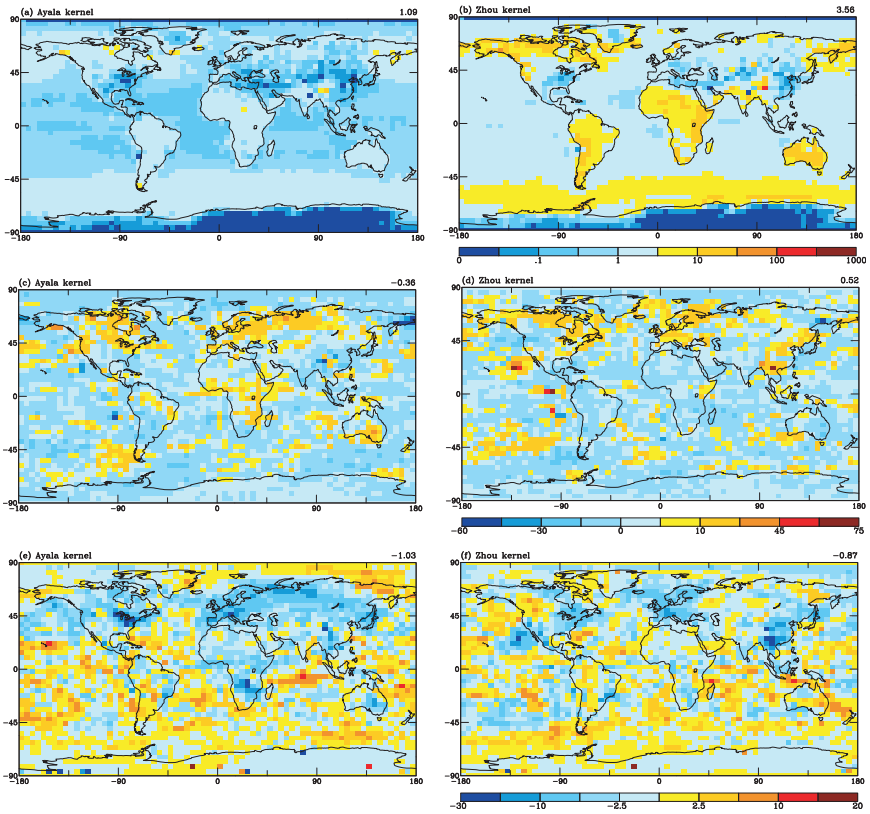

Figure 48: The annual mean, global distribution of autoconversion rate (GCM first vertical layer) for present day simulation: (a) Ayala, and, (b) Zhou kernels (top panels). The changes in LWP between present-day and preindustrial day: (c) Ayala , and, (d) Zhou kernels (mid panels). Shortwave indirect forcing using (e) Ayala, and, (f) Zhou kernels (bottom panels).

aerosol indirect forcing. While this is an important piece of information, it does not, by itself, indicate which of the simulations (if any) has the most realistic description of autoconversion. To address this issue, we use the concept of "autoconversion timescale", $\tau_{auto} = L/A$, expressing the timescale required for conversion of cloud-water into drizzle. Figure 49 shows the annual average predicted τ_{auto} for REF, P6, and KK simulations. A striking feature of REF is the uniformity of τ_{auto} (5-10 hr) virtually throughout the globe. This occurs because REF is based on the SD parameterization, which does not depend on CDNC concentrations (only on LWC). The main contrast in τ_{auto} is seen between marine and continental areas, where the adjustable parameters of the SD parameterization change (Table 21). Although KK exhibits a comparable global annual average A to REF (Figure 39), the scheme exhibits substantially larger spatial variability, because of the dependence of A on L and N. τ_{auto} between KK and REF are comparable only in the remote marine areas (especially in the tropics, where L is highest); in continental and polluted areas, τ_{auto} for KK is substantially increased (>100 h), about an order of magnitude larger than REF. P6 generally predicts about a factor of 2 larger than KK (Figure 39); τ_{auto} nevertheless is larger in polluted areas because of the threshold function applied. τ_{auto} for MC is comparable to P6; this is expected given that the magnitude and spatial distribution of A between the two formulations is quite comparable (Figure 39). Finally, τ_{auto} for GRV, TUR are generally an order of magnitude higher than for P6 and KK (not shown).

Autoconversion parameterizations can be evaluated by the extent to which the predicted τ_{auto} is consistent with observations. Since autoconversion rate is not an observable quantity, it can be estimated by applying the KCE to observed cloud droplet size distributions [73]. The ambient cloud droplet size distributions used in this study were collected during the CRYSTAL-FACE and CSTRIPE field campaigns

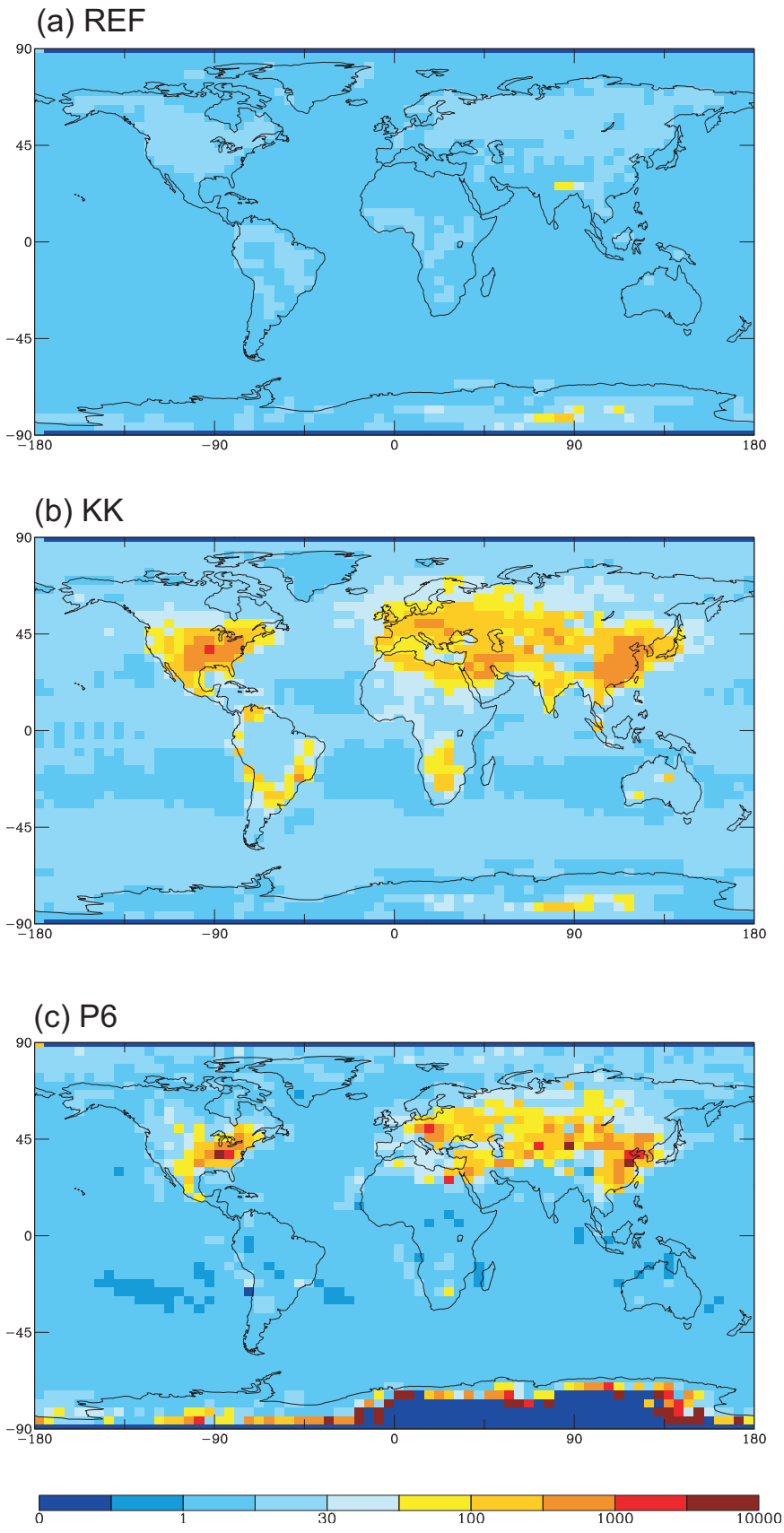

Figure 49: Annual average autoconversion timescale (hr) in the GCM first vertical layer (present day emissions), for (a) REF, (b) KK, and, (c) P6 simulations.

[46, 118], and are described in detail by [73] and [72]. About 165 measured distributions are used to produce "observed" values of A, from which τ_{auto} is computed and expressed against N and L. "Observed" τ_{auto} values are then compared against predictions from each of the simulations of Table 21. This is shown in Figure 50 for REF, P6, MC (top panel), and, TUR, KK (bottom panel) simulations. One can immediately see the effect of increasing N on observed τ_{auto}, a direct expression of drizzle suppression associated with the "second" aerosol indirect effect. As expected, the SD scheme (REF simulation, Figure 50a) exhibits a narrow range of τ_{auto}, ranging between 5 and 10 hours. All other simulations, including sensitivity of autoconversion to N, agree qualitatively with observed τ_{auto}, but are biased (sometimes considerably). Of all schemes, MC, P6 tend to lie within the observed range of τ_{auto} when predicted CDNC lies between 100 and 500 cm^{-3}. Similarly, KK also captures the trend in observed timescale, but with a much narrower envelope of values; this suggests that, depending on the value of L in a specific cloud type, KK may exhibit biased τ_{auto}, likely when the microphysical state (i.e., N, L) is substantially different from the LES simulations used to derive the KK formulation. The TUR (Figure 50b) and GRV (not shown) simulations capture τ_{auto} fairly well when CDNC > 300 cm^{-3}, but is 2-3 orders of magnitude too large for smaller droplet concentrations; this is possibly because the gamma distribution function used to represent the cloud droplet size distributions becomes too broad at low N. Based on Figure 50, P6, MC, KK parameterizations seem to best reproduce the τ_{auto} computed for ambient size distributions. This should not be construed to indicate that these parameterizations are superior to other formulations considered, but rather that their specific implementation exhibits a realistic range of τ_{auto}. Repeating the simulations with a different range of updraft velocity, water vapor uptake coefficient or aerosol microphysical package (used to predict N) may result in substantial shifts in the τ_{auto} ranges. Overall, an autoconversion timescale analysis offers a physically-based approach for assessing and constraining

parameterizations to yield A values consistent with those observed in ambient clouds.

5.5 Summary and conclusions

This paper investigates impacts of applying different autoconversion parameterizations and methodologies for computing autoconversion rate on predictions of the aerosol indirect effect on climate. To address the above questions, a series of simulations are carried out with the NASA Goddard Institute for Space Studies General Circulation Model II' (GISS GCM II'), in which both parameterizations and direct integration of the KCE are used online for computing autoconversion rate and climatic state for "preindustrial" and "present day" conditions. From the simulations, we assess: (a) the impact of autoconversion scheme on the predicted spatial and temporal distribution of cloud properties; (b) the sensitivity of predicted aerosol indirect forcing and climate state to autoconversion rate; (c) the importance of unresolved collection processes (such as turbulence) on indirect forcing and climate, and; (d) the realism of each autoconversion scheme as judged by comparison with ambient data.

Four autoconversion parameterizations ([159] (SD), [103] (P6), [87] (KK), and [113] (MC)), and direct integration of the stochastic collection equation (KCE) are considered for computing autoconversion rate. In the latter, the relative importance of gravity and turbulence on droplet collection is examined, and, two collection kernels with substantially different sensitivity to turbulence are considered. Simulations show that Liquid Water Path (LWP) correlates with aerosol loading, because of decreased autoconversion rate. The spatial distribution of indirect forcing strongly correlates with simulated changes in LWP between preindustrial and present day simulations, the largest cooling is seen in highly polluted areas such as SE Asia, Western Europe, and eastern US.

The combined first and second indirect effect is quite sensitive to the autoconversion scheme used, being -1.30 W m^{-2} for P6, -2.05 W m^{-2} for KK, and -1.53 W

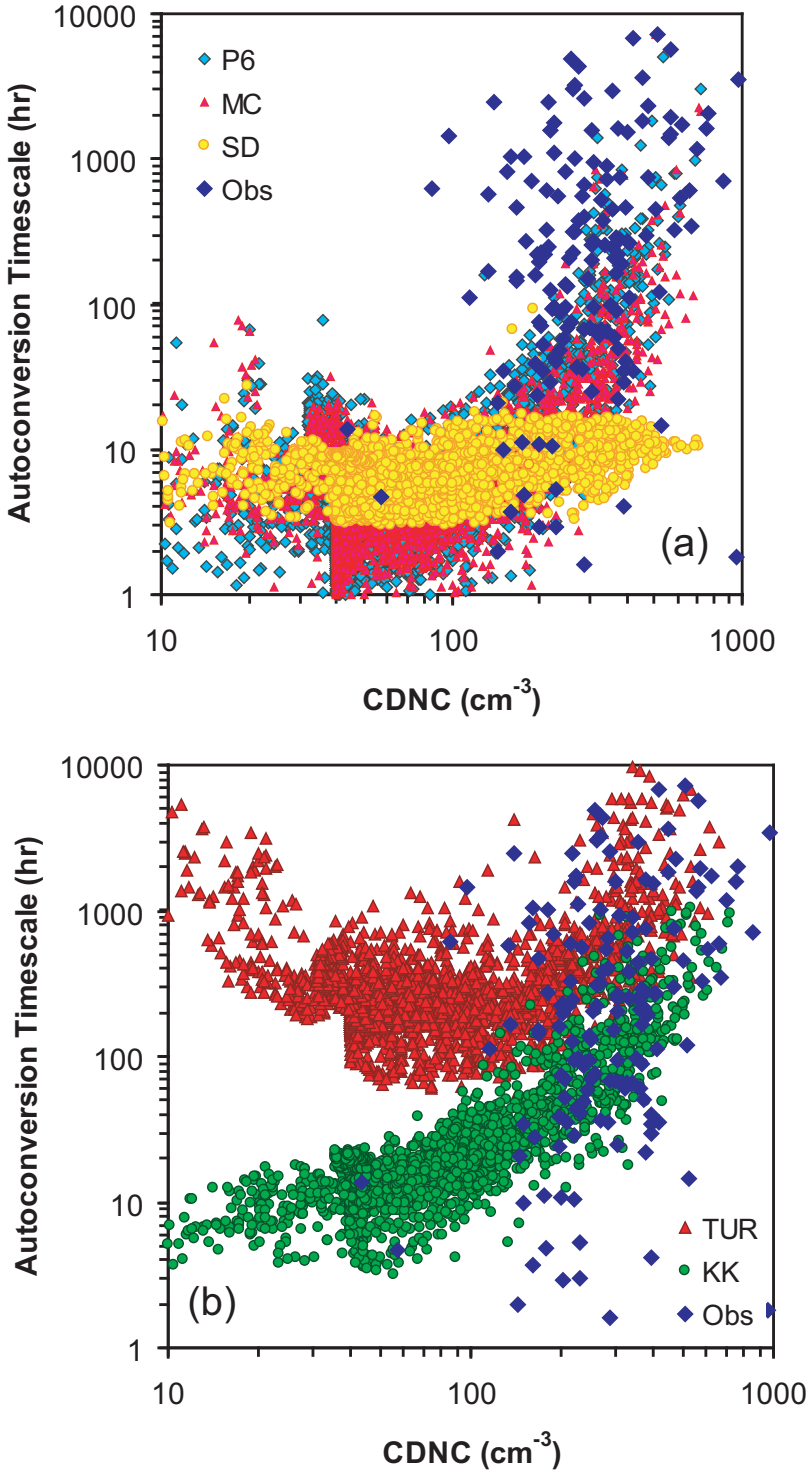

Figure 50: Annual average τ_{auto} vs. CDNC, for (a) REF, P6, MC, and, (b) KK, TUR simulations (present day emissions). "Obs" refer to τ_{auto} derived from application of KCE to ambient cloud droplet size distributions observed during the CSTRIPE and CRYSTAL-FACE campaigns.

m^{-2} for MC. Using KCE integration for computing autoconversion, a smaller indirect effect is simulated, being -0.89 W m^{-2} for GRV, and equal to -1.03 W m^{-2} for TUR simulation. Overall, the order of magnitude envelope in autoconversion rate from application of the autoconversion schemes considered translate to about a factor of two uncertainty in indirect forcing. Although this is an important uncertainty, it is much smaller than changes in TOA cloud forcing that arise from changing autoconversion parameterizations. This means that the sensitivity of climate-relevant parameters to changes in aerosol is fairly consistent, regardless of the autoconversion parameterization used.

Autoconversion parameterizations are evaluated by the extent to which they predict realistic values of "autoconversion timescale", $\tau_{auto} = L/A$, which expresses the timescale required for conversion of cloudwater into drizzle. Since autoconversion rate is not an observable quantity, it can be estimated by applying the KCE to observed cloud droplet size distributions, and used then to obtain τ_{auto} consistent with observations. The SD scheme a narrow range of τ_{auto}, ranging between 5 and 10 hours; all other simulations, including sensitivity of autoconversion to N, exhibit substantial variability. Of all schemes, MC, P6 tend to lie within the observed range of τ_{auto} when predicted CDNC lies between 100 and 500 cm^{-3}. Similarly, KK also captures the trend in observed timescale, but with a much narrower envelope of values; this suggests that, depending on the value of L in a specific cloud type, KK may exhibit biased τ_{auto}, likely when the microphysical state (i.e., N, L) is substantially different from the LES simulations used to derive the KK formulation. The TUR simulation capture τ_{auto} fairly well when CDNC $>$ 300 cm^{-3}, but is 2-3 orders of magnitude too large for smaller droplet concentrations. Hence, P6, MC, KK parameterizations seem to best reproduce the τ_{auto} computed for ambient size distributions. This does not imply that these parameterizations are superior to other formulations considered, but rather that their specific implementation exhibits a realistic range of τ_{auto}; hence,

an autoconversion timescale analysis offers a physically-based approach for assessing and constraining parameterizations to yield A values consistent with those observed in ambient clouds.

Finally, the simulations using the Ayala and Zhou turbulence collection kernels show that despite the factor of 10 discrepancy between collection kernels, predicted autoconversion rate differs by a factor of 3, resulting in comparable changes in LWP between preindustrial and present-day simulations; the estimated indirect forcing is also quite similar, being -1.03 and -0.87 Wm^{-2} for Ayala and Zhou kernel, respectively. This suggests that the magnitude of indirect forcing is not sensitive to the collection kernel used to describe turbulence. However the autoconversion rate computed with application of KCE in this study tends to give low autoconversion rate (i.e., high τ_{auto}); a future study, that exhibits a more realistic range of τ_{auto} will conclusively determine the importance of turbulence collection on autoconversion and the aerosol indirect climatic effect.

CHAPTER VI

CONCLUSIONS

This thesis first investigates cloud droplet number closure for marine stratocumulus clouds measured during MArine Stratus Experiment based on cloud parcel model frameworks. Evaluating cloud parameterization is important for studying aerosol effects on clouds and the number concentration of cloud droplet largely depends on amount of aerosols. Using three time interval for averaging updraft velocity, cloud droplet number to analyze droplet closure, we found taking the transect-average in general predicts the least error in droplet number concentration. The relationship between standard deviation and average cloud-base updraft velocity from measurements shows a good agreement with the analytical formulation. The latter is derived based on using a half-normal distribution to represent updraft distribution. This could be an important application to determine small-scale updraft velocity for cloud activation based on total kinetic energy predicted in large-scale models. Sensitivity study of the effect of water uptake coefficient on droplet number calculation shows a coefficient of 0.1 reveals the optimal closure and the prediction error of droplet number is also within the measurement uncertainty. Using size-resolved measurements from Aerosol Mass Spectrometer (AMS) show the variation of the soluble mass fraction is large among different sizes of particles. Incorporating the effect of size-resolved chemical composition of aerosol gives a better closure for a subset of cloud data analyzed in this study.

Second study evaluates droplet growth characteristics by comparing spectrum parameters from parcel model frameworks and in-situ measurements for cumulus

(CRYSTAL-FACE campaign) and stratocumulus clouds (CSTRIPE campaign). Using the spectra obtained at the level of s_{max}, as compared to using the predicted spectra at the level where predicted LWC is close to the measured LWC, has better agreement of relative dispersion from measurements. This is, to the author's knowledge, the first attempt to evaluate droplet size distributions for an extensive spectrum set of a wide range of cloud conditions. The approach of using a PDF updraft for simulating droplet evolution has the effect to broaden the droplet spectrum as compared to the approach of using a single average updraft, this can be seen for both cloud sets analyzed in this study. The PDF updraft approach exhibits the importance of dynamical variability on droplet spectrum development and the composite size distributions may come from different parcels which may experience varying growth histories along their paths. The sensitivity of relative dispersion to the effective water uptake coefficient shows the value used for water uptake coefficient does not produce a significant change in droplet spectrum closure. This may be an important indication for aerosol indirect estimation studies such that even through chemical heterogeneity of particles is large, this does not cause a significant difference for droplet dispersion.

The third study investigates the effect of turbulence on the calculated autoconversion rate obtained by direct integration of kinetic collection equation (KCE). As compared to KCE integration for gravitational kernel only, including turbulence effects on droplet collection increases autoconversion by about a factor of 1.82 and 1.24 for CRYSTAL-FACE and CSTRIPE clouds, respectively. Using the in-situ measurements to investigate the effect of turbulence on autoconversion rate, to the author's knowledge, is the first study in the field. Even though turbulence can substantially accelerate growth of droplet size distribution, it does not enhance autoconversion to a significant extent. Our study shows the enhancement on average for two cloud data sets is much lower than uncertainty caused by different autoconversion schemes.

Sensitivity study of the separation size used for KCE integration shows about a twofold uncertainty in autoconversion rate is obtained when shifting size from 20 to 25 μm in radius. Certain autoconversion schemes have better agreement for certain types of clouds. The parameterization of [87] reveals better agreement with KCE for CRYSTAL-FACE clouds but the scheme developed by [103] is in better agreement for CSTRIPE clouds. Parameterizations that explicitly compute autoconversion tend to be closer with KCE, but are still subject to substantial uncertainty, about an order of magnitude in autoconversion rate. The timescale of rain formation, τ_{rain} (equivalent to the timescale of autoconversion, τ_{auto} since autoconversion is the rate-limiting step for forming rain), is a useful metric to interpret uncertainty of autoconversion rate. Comparison of τ_{rain} between parameterizations and KCE suggests "tuning" of parameterizations to minimize the average τ_{rain} error, may be accompanied by a strong reduction in prediction scatter, and be an efficient way to improve autoconversion predictions in large scale models.

The last part of this thesis studies the effect of different autoconversion schemes on the estimate of indirect effects. Three simulations, in addition to simulations using traditional parameterizations for autoconversion rate, are conducted where autoconversion rate is calculated based on direct integration of KCE. Using KCE integration to compute autoconversion in GCM, to the author's knowledge, is the first study in the field. Considering the effect of turbulence on estimation of aerosol indirect effect is also the topic which has not been explored. Simulations show that Liquid Water Path (LWP) correlates with aerosol loading and the spatial distribution of indirect forcing strongly is related to the simulated changes in LWP between preindustrial and present day simulations: the largest cooling is seen in highly polluted areas such as SE Asia, Western Europe, and eastern US. Furthermore, our study shows the combined first and second indirect effect is quite sensitive to the autoconversion scheme used, being -1.30 W m^{-2} for P6, -2.05 W m^{-2} for KK, and -1.53 W m^{-2} for MC. Using

KCE integration for computing autoconversion, a smaller indirect effect is simulated, being -0.89 W m^{-2} for GRV, and equal to -1.03 W m^{-2} for TUR simulation. Overall, the order of magnitude envelope in autoconversion rate from application of the autoconversion schemes considered translate to about a factor of two uncertainty in indirect forcing. Although this is an important uncertainty, it is much smaller than changes in TOA cloud forcing that arise from changing autoconversion parameterizations. This means that the sensitivity of climate-relevant parameters to changes in aerosol is fairly consistent, regardless of the autoconversion parameterization used.

CHAPTER VII

FUTURE DIRECTIONS AND IMPLICATIONS

In this thesis we evaluated cloud droplet number concentration and droplet size distribution using 1-D adiabatic cloud parcel model and its simplification of parameterization with in-situ cumulus and stratocumulus clouds. Considering the dynamic variability effect by using PDF for calculating an average droplet spectra, the predicted width of the droplet size distribution is still underestimated. This implies that the common feature of broad spectra obtained from the measurement may be a result of a combination of other effects, such as entrainment and mixing. Their effects on droplet growth and the subsequent changes in cloud properties should be accounted in the future.

The difference among autoconversion parameterizations is large and this uncertainty adds more variability for indirect forcing estimate. The evaluation of autoconversion schemes could be applied to different cloud datasets, for example, to the droplet spectra which are actually drizzling or close to drizzle. Also, to identify if there is a coherent pattern in size distributions (or in certain cloud conditions) that autoconversion schemes perform comparatively well is also an interesting topic for future study. The suitability of cloud parameterizations for providing subgrid scale processes has been studied long time. A realistic simulation must reply on good understanding of physical processes and also the control mechanisms as well. The correct way to represent them must be established in a consistent way. This indicates developing cloud parameterizations and their evaluations would still be needed.

As initially stated aerosol-cloud-climate interactions is complex. This is manifest in our results when the feedbacks of climate system are included in the simulations.

The climate does not response linearly as internal/external perturbations are forced. The fact is that real physical world is not operating in independent way, for the study of aerosol effects, concurrent changes in physical, dynamical and radiative processes must be examined as a whole to provide a better prediction ability for climate change.

REFERENCES

[1] Abdul-Razzak, H. and Ghan, S. J., "A parameterization of aerosol activation: 2. Multiple aerosol types," *J. Geophys. Res.*, vol. 105, pp. 6837–6844, 2000.

[2] Abdul-Razzak, H. and Ghan, S. J., "A parameterization of aerosol activation: 3. Sectional representation," *J. Geophys. Res.*, vol. 107, p. doi:10.1029/2001JD000483, 2002.

[3] Abdul-Razzak, H. and Ghan, S. J., "Parameterization of the influence of organic surfactants on aerosol activation," *J. Geophys. Res.*, vol. 109, p. doi:10.1029/2003JD004043, 2004.

[4] Abdul-Razzak, H., Ghan, S. J., and Rivera-Carpio, C., "A parameterization of aerosol activation: 1. Single aerosol type," *J. Geophys. Res.*, vol. 103, pp. 6123–6132, 1998.

[5] Abramowitz, M. and Stegun, I., *Handbook of Mathematical Functions*. New York: Dover, 1965.

[6] Adams, P. J., Seinfeld, J. H., Koch, D., Mickley, L., and Jacob, D., "General circulation model assessement of direct radiative forcing by the sulfate-nitrate-ammonium-water inorganic aerosol system," *J. Geophys. Res.*, vol. 106, pp. 1097–1111, 2001.

[7] Adams, P. J., Seinfeld, J. H., and Koch, D. M., "Global concentrations of tropospheric sulfate, nitrate, and ammonium aerosol simulated in a general circulation model," *J. Geophys. Res.*, vol. 104, pp. 13791–13823, 1999.

[8] Albrecht, B. A., "Aerosols, cloud microphysics, and fractional cloudiness," *Science*, vol. 245, pp. 1227–1230, 1989.

[9] Albrecht, B. A., "Aerosols, cloud microphysics, and fractional cloudiness," *Science*, vol. 245, pp. 1227–1230, 1989.

[10] Asa-Awuku, A. and Nenes, A., "The effect of solute dissolution kinetics on cloud droplet formation: 1. Extended Köhler theory," *J. Geophys. Res.*, vol. 112, p. doi:10.1029/2005JD006934, 2007.

[11] Ayala, O., Rosa, B., Wang, L.-P., and Grabowski, W. W., "Effects of turbulence on the geometric collision rate of sedimenting droplets: Part 1. Results from direct numerical simulation," *New J. Phys.*, vol. 10, p. 075015, 2008.

[12] Ayala, O., Rosa, B., Wang, L.-P., and Grabowski, W. W., "Effects of turbulence on the geometric collision rate of sedimenting droplets: Part 2. Theory and parameterization.," *New J. Phys.*, vol. 10, p. 075016, 2008.

[13] Bahreini, R., Jimenez, J. L., Wang, J., Flagan, R. C., Seinfeld, J. H., Jayne, J. T., and Worsnop, D. R., "Aircraft-based aerosol size and composition measurements during ace-asia using an aerodyne aerosol mass spectrometer," *J. Geophys. Res.*, vol. 108, p. doi:10.1029/2002JD003226, 2003.

[14] Barahona, D. and Nenes, A., "Parameterization of cloud droplet formation in large scale models: including effects of entrainment," *J. Geophys. Res.*, vol. 110, p. doi:10.1029/2007JD008473, 2007.

[15] Baughcum, S. L., Chan, D. M., Happenny, S. M., Henderson, S. C., Hertel, P. S., Higman, T., Maggiora, D. R., and Oncina, C. A., "Emissions scenarios development: Scheduled 1990 and project 2015 subsonic, Mach 2.0 and Mach 2.4 aircraft, in *The Atmopheric Effects of Stratospheric Aircraft: a Third Program Report, NASA RF. Rubl.*," vol. 1313, pp. 89–131, Nov. 1993.

[16] Baumgardner, D., Jonsson, H., Dawson, W., O'Connor, D., and Newton, R., "Cloud, aerosol and precipitation spectrometer: A new instrument for cloud investigations," *Atmos. Res.*, vol. 59–60, pp. 251–264, 2001.

[17] Baumgardner, D. and Spowart, M., "Evaluation of the Foward Scattering Spectrometer Probe. part III: Time response and laser inhomogeneity limitations," *J. Atmos. Ocean. Tech.*, vol. 7, pp. 666–672, 1990.

[18] Beard, K. V. and Ochs, H. T. I., "Warm-rain initiation: an overview of microphysical mechanism.," *J. Appl. Meteorol.*, vol. 33, pp. 608–625, 1993.

[19] Beheng, K. D., "A parameterization of warm cloud microphysical conversion processes," *Atmos. Res.*, vol. 33, pp. 193–206, 1994.

[20] Beheng, K. D. and Doms, G., "A general formulation of collection rates of cloud and raindrops using the kinetic equation and comparison with parameterizations," *Beitr. Phys. Atmos*, vol. 59, pp. 66–84, 1986.

[21] Benkovitz, C. M., Scholtz, M. T., Pacyna, J., Tarrason, L., Dignon, J., Voldner, E. C., Spiro, P. A., Logan, J. A., and Graedel, T. E., "Global gridded inventories of anthropogenic emissions of sulfur and nitrogen," *J. Geophys. Res.*, vol. 101, pp. 29239–29253, 1996.

[22] Berry, E. X., "Cloud droplet growth by coalescence," *J. Atmos. Sci.*, vol. 24, pp. 688–701, 1967.

[23] Berry, E. X. and Reinhardt, R. L., "An analysis of cloud drop growth by collection. Part I. Double distributions," *J. Atmos. Sci.*, vol. 31, pp. 1814–1824, 1974.

[24] Bleck, R., "A fast approximative method for integrating the stochastic coalescence equation," *J. Geophys. Res.*, vol. 75, pp. 5165–5171, 1970.

[25] Borys, R.D., D. L. S. C. and Brown, W., "Mountaintop and radar measurements of anthropogenic aerosol effects on snow growth and snow rate," *Geophys. Res. Lett.*, vol. 30(10), pp. 1538,doi:10.1029/2002GL016855, 2003, 2003.

[26] Borys, R. D., Lowenthal, D. H., and Mitchel, D. L., "The relationship among cloud physics, chemistry and precipitation rate in cold mountain clouds," *Atmos. Environ.*, vol. 34, p. 25932602, 2000.

[27] Bott, A., "A flux method for the numerical solution of the stochastic collection equation," *J. Atmos. Sci.*, vol. 55, pp. 2284–2293, 1998.

[28] Bott, A., Sievers, U., and Zdunkowski, W., "A radiation fog model with a detailed treatment of the interaction between radiative transfer and fog microphysics," *J. Atmos. Sci.*, vol. 47, pp. 2153–2166, 1990.

[29] Boucher, O. and Lohmann, U., "The sulfate-ccn-cloud albedo effect: A sensitivity study with 2 general-circulation models," *Tellus*, vol. 47, pp. 281–300, 1995.

[30] Braham, R. R. *Bull. Am. Met. Soc*, vol. 49, p. 343, 1968.

[31] Brenguier, J.-L., Bourrianne, T., Coelho, A., Isbert, J., Peytavi, R., Trevarin, D., and Weschler, P., "Improvements of droplet size distribution measurements with the fast-fssp (forward scattering spectrometer probe)," *J. Atmos. Ocean. Tech.*, vol. 15, pp. 1077–1090, 1998.

[32] Brenguier, J.-L. and Chaumat, L., "Droplet spectra broadening in cumulus clouds. Part I: broadening in adiabatic cores.," *J. Atmos. Sci.*, vol. 58, pp. 628–641, 2001.

[33] Bretherton, C. S., Macvean, M. K., Bechtold, P., Chlond, A., Cotton, W. R., Cuxart, J., Cuijpers, H., Khairoutdinov, M., Kosovic, B., Lewellen, D., Moeng, C. H., Siebesma, P., Stevens, B., Stevens, D. E., Skyes, I., and Wyant, M. C., "An intercomparison of radiatively driven entrainment and turbulence in a smoke cloud; as simulated by different numerical models.," *Quart. J. Roy. Meteor. Soc.*, vol. 125, pp. 391–423, 1999.

[34] Broekhuizen, K., Chang, R. Y. W., Leaitch, W. R., Li, S. M., and Abbatt, J. P. D., "Closure between measured and modeled cloud condensation nuclei (CCN) using size-resolved aerosol compositions in downtown toronto," *Atmos. Chem. Phys. Discuss.*, vol. 5, pp. 6263–6293, 2005.

[35] Burnet, F. and Brenguier, J.-L., "Comparison between standard and modified forward scattering spectrometer probes during the small cumulus microphysics study," *J. Atmos. Ocean. Tech.*, vol. 19, pp. 1516–1531, 2002.

[36] Celik, F. and Marwitz, J. D., "Droplet spectra broadening by ripening process. Part I: Roles of curvature and salinity of cloud droplets," *J. Atmos. Sci.*, vol. 56, pp. 3091–3105, 1999.

[37] Charlson, R. J., Schwartz, S. E., Hales, J. M., Cess, R. D., Coakley, J. A., Hansen, J. E., and Hofmann, D. J., "Climate forcing by anthropogenic aerosols," *Science*, vol. 255, no. 5043, pp. 423–430, 1992.

[38] Chaumat, L. and Brenguier, J.-L., "Droplet spectra broadening in cumulus clous. Part II: microscale droplet concentration heterogeneities," *J. Atmos. Sci.*, vol. 58, pp. 642–654, 2001.

[39] Chen, J.-P. and Lamb, D., "Simulation of cloud microphysical and chemical processes using a multicomponent framework. Part I: Description of the microphysical model," *J. Atmos. Sci.*, vol. 51, pp. 2613–2630, 1994.

[40] Chuang, C. C. and Penner, J. E., "Effects of anthropogenic sulfate on cloud drop nucleation and optical properties," *Tellus*, vol. 47, pp. 566–577, 1995.

[41] Chuang, C. C., Penner, J. E., Taylor, K. E., Grossmann, A. S., and Walton, J. J., "An assessment of the radiative effects of anthropogenic sulfate," *J. Geophys. Res.*, vol. 102, pp. 3761–3778, 1997.

[42] Chuang, P., "Measurement of the timescale of hygroscopic growth for atmospheric aerosols," *J. Geophys. Res.*, vol. 108, p. doi:10.1029/2002JD002757., 2003.

[43] Chuang, P. Y., Charlson, R. J., and Seinfeld, J. H., "Kinetic limitations on droplet formation in clouds," *Nature*, vol. 390, pp. 594–596, 1997.

[44] Coakley, J. A., Bernstein, R. L., and Durkee, P. A., "Effect of shipstack effluents on cloud reflectivity," *Science*, vol. 237, pp. 1020–1022, 1987.

[45] Cohard, J. and Pinty, J., "A comprehensive two-moment warm microphysical bulk scheme. I: Description and tests," *Q. J. R. Meteorol. Soc.*, vol. 126, pp. 1815–1842, 2000.

[46] Conant, W., Vanreken, T., Rissman, T., Varutbangkul, V., Jimenez, J., Delia, A., Bahreini, R., Roberts, G., Nenes, A., Jonsson, H., Flagan, R. C., and Seinfeld, J. H., "Aerosol-cloud drop concentration closure in warm cumulus," *J. Geophys. Res.*, vol. 109, pp. D13204, doi:10.1029/2003JD004324, 2004.

[47] Cooper, W. A. and Vali, G., "The origin of ice in mountain cap clouds," *J. Atmos. Sci.*, vol. 38, pp. 1244–1259, 1981.

[48] Del Genio, A. D., Yao, M.-S., Kovari, W., and Lo, K.-W., "A prognostic cloud water parameterization for Global Climate Models," *J. Climate*, vol. 9, pp. 270–304, 1996.

[49] Durkee, P. A., Noone, K. J., and Bluth, R. T., "The Monterey area ship track experiment," *J. Atmos. Sci.*, vol. 57, pp. 2523–2541, 2000.

[50] Durkee, P. A., Noone, K. J., Ferek, R. J., Johnson, D. W., Taylor, J. P., Garrett, T. J., Hobbs, P. V., Hudson, J. G., Bretherton, C. S., Innis, G., Frick, G. M., Hoppel, W. A., O'Dowd, C. D., Russell, L. M., Gasparovic, R., Nielsen, K. E., Tessmer, S. A., Ostrom, E., Osborne, S. R., Flagan, R. C., Seinfeld, J. H., and Rand, H., "The impact of ship-produced aerosols on the microstructure and albedo of warm marine stratocumulus clouds: A test of MAST hypotheses 1i and 1ii," *J. Atmos. Sci.*, vol. 57, pp. 2554–2569, 2000.

[51] Dye, J. E. and Baumgardner, D., "Evaluation of the forward scattering spectrometer probe. Part i: Electronic and optical studies," *J. Atmos. Ocean. Tech.*, vol. 1, pp. 329–344, 1984.

[52] Erlick, C., Khain, A., Pinsky, M., and Segal, Y., "The effect of wind velocity fluctuations on drop spectrum broadening in stratocumulus clouds," *Atmos. Res.*, vol. 75, pp. 15–45, 2005.

[53] Facchini, M., Mircea, M., Fuzzi, S., and Charlson, R., "Cloud albedo enhancement by surface-active organic solutes in growing droplets," *Nature*, vol. 401, pp. 257–259, 1999.

[54] Feingold, G. and Chuang, P. Y., "Analysis of the influence of film forming compounds on droplet growth: Implications for cloud microphysical processes and climate," *J. Atmos. Sci.*, vol. 59, pp. 2006–2018, 2002.

[55] Feingold, G. and Heymsfield, A., "Parameterizations of condensational growth of droplets for use in general circulation models," *J. Atmos. Sci.*, vol. 49, pp. 2325–2342, 1992.

[56] Ferek, R. J., Garrett, T., Hobbs, P. V., Strader, S., Johnson, D., Taylor, J. P., Nielsen, K., Ackerman, A. S., Kogan, Y., Liu, Q. F., Albrecht, B. A., and Babb, D., "Drizzle suppression in ship tracks," *JATS*, vol. 57, pp. 2707–2728, 2000.

[57] Ferek, R., Hegg, D., and Hobbs, P., "Measurements of ship-induced tracks in clouds off the washington coast," *J. Geophys. Res.*, vol. 103, p. 2319923206, 1998.

[58] Fountoukis, C. and Nenes, A., "Continued development of a cloud droplet formation parameterization for global climate models," *J. Geophys. Res.*, vol. 110, p. doi:10.1029/2004JD005591, 2005.

[59] Fountoukis, C. and Nenes, A., "ISORROPIA II: A computationally efficient aerosol thermodynamic equilibrium model for K^+, Ca^{2+}, Mg^{2+}, NH_4^+, Na^+, SO_4^{2-}, NO_3^-, Cl^-, H_2O aerosols," *Atmos. Chem. Phys.*, vol. 7, pp. 4639–4659, 2007.

[60] Fountoukis, C., Nenes, A., Meskhidze, N., Bahreini, R., Conant, W. C., Jonsson, H., Murphy, S., Sorooshian, A., Varutbangkul, V., Brechtel, F., Flagan, R. C., and Seinfeld, J. H., "Aerosol-cloud drop concentration closure for clouds sampled during the international consortium for atmospheric research on transport and transformation 2004 campaign," *J. Geophys. Res.*, vol. 112, p. doi:10.1029/2006JD007272, 2007.

[61] Gerber, H., Jensen, J. B., Davis, A. B., Marshak, A., and Wiscombe, W. J., "Spectral density of cloud liquid water content at high frequencies," *J. Atmos. Sci.*, vol. 58, pp. 497–503, 2001.

[62] Ghan, S., Chuang, C., Easter, R., and Penner, J., "A parameterization of cloud droplet nucleation: 2. multiple aerosol types," *Atmos. Res.*, vol. 36, pp. 39–54, 1995.

[63] Ghan, S., Chuang, C., and Penner, J., "A parameterization of cloud droplet nucleation. Part I: Single aerosol species," *Atmos. Res.*, vol. 30, pp. 197–222, 1993.

[64] Ghan, S. J., Leung, L. R., Easter, R. C., and Abdul-Razzak, H., "Prediction of cloud droplet number in a general circulation model," *J. Geophys. Res.*, vol. 102, pp. 21777–21794, 1997.

[65] Guenther et al., "A global model of natural volatile organic compound emissions," *J. Geophys. Res.*, vol. 100, pp. 8873–8892, 1995.

[66] Hack, J. J., Caron, J. M., Yeager, S. G., Oleson, K. W., Holland, M. M., Truesdale, J. E., and Rasch, P. J., "Simulation of the global hydrological cycle in the CCSM Community Atmosphere Model Version 3 (CAM3): Mean features," *J. Climate*, vol. 19, pp. 2199–2221, 2006.

[67] Hall, W. D., "A detailed microphysical model within a two-dimentional dynamic framework - Model description and preliminary results," *J. Atmos. Sci.*, vol. 37, pp. 2486–2507, 1980.

[68] Hansen, J., Russell, G., Rind., D., Stone, P., Lacis, A., Lebedeff, S., Ruedy, R., and Travis, L., "Efficient three-dimensional global models for climate studies: Models I and II," *Mon. Wea. Rev.*, vol. 111, pp. 609–662, 1983.

[69] Haywood, J. and Boucher, O., "Estimates of the direct and indirect radiative forcing due to tropospheric aerosols: A review," *Rev. Geophys.*, vol. 38, no. 4, pp. 513–543, 2000.

[70] Hegg, D. A., Radke, L. F., and Hobbs, P. V. *J. Geophys. Res.*, vol. 96, p. 18727, 1991.

[71] Hobbs, P. V. and Rangno, A. L., "Ice-particle concentrations in clouds," *J. Atmos. Sci.*, vol. 42, pp. 2523–2549, 1985.

[72] Hsieh, W. C., Jonsson, H., Buzorius, G., Flagan, R. C., Seinfeld, J. H., and Nenes, A., "Parameterization of cloud droplet size distributions: comparison with parcel models and observations," *J. Geophys. Res.*, in review.

[73] Hsieh, W. C., Jonsson, H., Buzorius, G., Wang, L. P., Flagan, R. C., Seinfeld, J. H., and Nenes, A., "On the representation of droplet coalescence and autoconversion: Evaluation using ambient cloud droplet size distributions," *J. Geophys. Res.*, in press.

[74] Iacobellis, S. F. and Somerville, R. C. J., "Evaluating parameterizations of the autoconversion process using a single-column model and atmospheric radiation measurement program measurements," *J. Geophys. Res.*, vol. 111, no. D02203, p. doi:10.1029/2005JD006296, 2006.

[75] Intergovernmental Panel on Climate Change (IPCC), *Climate Change 2007: The Physical Science Basis*. UK: Cambridge University Press, 2007.

[76] J., W., "The microstructure of cumulus cloue: Part 4: The effect on the droplet spectrum of mixing between cloud and environmen," *J. Atmos. Sci.*, vol. 30, pp. 256–261, 1973.

[77] Jaenicke, R. and Hanusch, T., "Simulation of the optical-particle counter forward scattering spectrometer probe-100 (FSSP-100)-Consequences for size distribution measurements," *Aerosol Sci. Technol.*, vol. 18, pp. 309–322, 1993.

[78] Jayne, J. T., Leard, D. C., Zhang, X., Davidovits, P., Smith, K. A., Kolb, C. E., and Worsnop, D., "Development of an aerosol mass spectrometer for size and composition analysis of submicron particles," *Aerosol Sci. Technol.*, vol. 33, pp. 49–70, 2000.

[79] Jensen, J. and Charlson, R., "On the efficiency of nucleation scavenging," *Tellus*, vol. 36, pp. 367–375, 1984.

[80] Jones, A., Roberts, D. L., and Woodage, M. J., "Indirect sulphate aerosol forcing in a climatic model with an interactive sulphur cycle," *J. Geophys. Res.*, vol. 106, pp. 20293–30310, 2001.

[81] Kanakidou, M., Seinfeld, J. H., Pandis, S. N., Barnes, I., Dentener, F. J., Facchini, M. C., Van Dingenen, R., Ervens, B., Nenes, A., Nielsen, C. J., Swietlicki, E., Putaud, J. P., Balkanski, Y., Fuzzi, S., Horth, J., Moortgat, G. K., Winterhalter, R., Myhre, C. E. L., Tsigaridis, K., Vignati, E., Stephanou, E. G., and Wilson, J., "Organic aerosol and global climate modelling: a review," *Atmos. Chem. Phys.*, vol. 5, pp. 1053–1123, 2005.

[82] Kaufman, Y. J., Koren, I., Remer, L. A., Rosenfeld, D., and Rudich, Y., "The effect of smoke, dust, and pollution aerosol on shallow cloud development over the atlantic ocean," *Proc. Nat. Acad. Sci.*, vol. 102, pp. 11207–11212, 2005.

[83] Kerkweg, A., Wurzler, S., Reisin, T., and Bott, A., "On the cloud processing of aerosol particles: an entraining air-parcel model with two dimensional spectral cloud microphysics and a new formulation of the collection kernel," *Quart. J. Roy. Meteor. Soc.*, vol. 129, pp. 1–18, 2003.

[84] Kessler, E., "On the distribution and continuity of water substance in atmospheric circulation," Tech. Rep. 32, Meteor. Monogr., Amer. Meteor. Soc., 1969.

[85] Kettle et al., "A global database of sea surface dimethylsulfide (DMS) measurements and a procedure to predict sea surface DMS as a function of latitude longitude and month," *Global Biogeochem. Cycles*, vol. 13, pp. 394–444, 1999.

[86] Khain, A., Ovtchinnikov, M., Pinsky, M., Pokrovsky, A., and Krugliak, H., "Notes on the state-of-the-art numerical modeling of cloud microphysics," *Atmos. Res.*, vol. 55, pp. 159–224, 2000.

[87] Khairoutdinov, M. and Kogan, Y., "A new cloud physics parameterization in a large-eddy simulation model of marine stratocumulus," *Mon. Wea. Rev.*, vol. 128, pp. 229–243, 2000.

[88] Khvorostyanov, V. and Curry, J., "Toward the theory of stochastic condensation in clouds. Part II: Analytical solutions of the gamma-distribution type.," *J. Aerosol Sci.*, vol. 56, pp. 3997–4013, 1999.

[89] Koch, D., Jacob, D., Tegen, I., Rind, D., and Chin, M., "Tropospheric sulfur simulation and sulfate direct radiative forcing in the Goddard Insititude for Space Studies general circulation model," *J. Geophys. Res.*, vol. 104, pp. 23799–23822, 1999.

[90] Korolev, A. V., Isaac, G. A., Cober, S. G., Strapp, J. W., and Hallett, J., "Microphysical characterization of mixed-phase clouds," *Quart. J. Roy. Meteor. Soc.*, vol. 129, pp. 39–65, 2003.

[91] Kovetz, A. and Olund, B., "The effect of coalescence and condensation on rain formation in a cloud of finite vertical extent," *J. Atmos. Sci.*, vol. 26, pp. 1060–1065, 1969.

[92] Laaksonen, A., Vesala, T., Kulmala, M., Winkler, P. M., and Wagner, P. E., "On cloud modelling and the mass accommodation coefficient of water," *Atmos. Chem. Phys. Discuss.*, vol. 4, pp. 7281–7290, 2004.

[93] Lacis, A. and Hansen, J. E., "Parameterization for the absorption of solar radiation in the Earth's atmosphere," *J. Atmos. Sci.*, vol. 31, pp. 118–133, 1974.

[94] Lacis, A. and Oinas, V., "A description of the correlated k-distribution method for modeling non-gray gaseous absorption, thermal emission, and multiple scattering in vertically inhomogeneous atmospheres," *J. Geophys. Res.*, vol. 96, pp. 9027–9064, 1991.

[95] Lance, S., Nenes, A., and Rissman, T., "Chemical and dynamical effects on cloud droplet number: Implications for estimates of the aerosol indirect effect," *J. Geophys. Res.*, vol. 109, p. doi:10.1029/2004JD004596, 2004.

[96] Lappen, C. L. and Randall, D. A., "Toward a unified parameterization of the boundary layer and moist convection. Part III: Simulations of clear and cloudy convection," *J. Atmos. Sci.*, vol. 58, pp. 2052–2072, 2001.

[97] Lasher-Trapp, S. G., Knight, C., and Straka, J. M., "Ultragiant aerosol growth by collection within a warm continental cumulus.," *AMS Conference on Cloud Physics 17-21 August, Everett, Washington*, pp. 494–497, 1998.

[98] Latham, J. *Quart. J. Roy. Meteor. Soc.*, vol. 95, p. 349, 1969.

[99] Leroy, D., Monier, M., Wobrock, W., and Flossmann, A. I., "A numerical study of the effects of the aerosol particle spectrum on the development of the ice phase and precipitation formation," *Atmos. Res.*, vol. 80(1), pp. 14–45, 2006.

[100] Liss, P. S. and Merlivat, L., "Air-sea gas exchange rates: Introduction and sythesis, in *The Role of Air-Sea Exchange in Geochemical Cycling*," vol. D. Reidel, Norwell, Mass., 1986.

[101] Liu, Y. and Daum, P. H., "Spectral dispersion of cloud droplet size distributions and the parameterization of cloud droplet effective radius," *Geophys. Res. Lett.*, vol. 27 (13), pp. 1903–1906, 2000.

[102] Liu, Y. and Daum, P. H., "Indirect warming effect from dispersion forcing," *Nature*, vol. 419, pp. 580–581, 2002.

[103] Liu, Y. and Daum, P. H., "Parameterization of the autoconversion process. Part I : Analytical formulation of the Kessler-type parameterizations," *J. Atmos. Sci.*, vol. 61, pp. 1539–1548, 2004.

[104] Liu, Y. and Daum, P. H., "Reply," *J. Atmos. Sci.*, vol. 62, pp. 3007–3008, 2005.

[105] Liu, Y., Daum, P. H., McGraw, R., and Miller, M., "Generalized threshold function accounting for effect of relative dispersion on threshold behavior of autoconversion process," *Geophys. Res. Lett.*, vol. 33, p. doi:10.1029/2005GL025500, 2006.

[106] Lohmann, U. and Feichter, J., "Impact of sulfate aerosols on albedo and lifetime of clouds: A sensitivity study with the ECHAM4 GCM," *J. Geophys. Res.*, vol. 102, pp. 13685–13700, 1997.

[107] Lohmann, U. and Feichter, J., "Impact of sulfate aerosols on albedo and lifetime of clouds: A sensitivity study with the ECHAM4 GCM," *J. Geophys. Res.*, vol. 102, pp. 13685–13700, 1997.

[108] Lohmann, U. and Feichter, J., "Global indirect aerosol effects: a review," *Atmos. Chem. Phys.*, vol. 5, pp. 715–737, 2005.

[109] Lohmann, U., Feichter, J., Chuang, C. C., and Penner, J. E., "Prediction of the number of cloud droplets in the ECHAM GCM," *J. Geophys. Res.*, vol. 104, pp. 9169–9198, 1999.

[110] Long, A. B., "Solutions to droplet collection equation for polynomial kernels," *J. Atmos. Sci.*, vol. 31, pp. 1040–1052, 1974.

[111] MacPherson, J. I. and Isaac, G. A., "Turbulence characteristics of some Canadian cumulus clouds," *J. Appl. Meteor.*, vol. 16, pp. 81–90, 1977.

[112] Manson, B. J., *The Physics of Clouds*. Clarendon Press, Oxford, 1971, 671 pp.

[113] Manton, M. J. and Cotton, W. R., *Formulation of approximate equations for modeling moist deep convection on the mesoscale*. PhD thesis, Colorado State University, 1977.

[114] Martin, G. M., Johnson, D. W., and Spice, A., "The measurement and parameterization of effective radius of droplets in warm stratocumulus clouds," *J. Atmos. Sci.*, vol. 51, pp. 1823–1842, 1994.

[115] Medina, J., Nenes, A., Sotiropoulou, R.-E. P., Cottrell, L. D., Ziemba, L. D., Beckman, P. J., and Griffin, R. J., "Cloud condensation nuclei closure during the International Consortium for Atmospheric Research on Transport and Transformation 2004 campaign: Effects of size-resolved composition," *J. Geophys. Res.*, vol. 112, p. doi:10.1029/2006JD007588, 2007.

[116] Menon, S., Brenguier, J. L., Boucher, O., Davison, P., Genio, A. D. D., Feichter, J., Ghan, S., Guibert, S., Liu, X. H., Lohmann, U., Pawlowska, H., Penner, J. E., Quaas, J., Roberts, D. L., Schuller, L., and Snider, J., "Evaluating aerosol/cloud/radiation process parameterizations with single-column models and Second Aerosol Characterization Experiment (ACE-2) cloudy column observations," *J. Geophys. Res.*, vol. 108(D24), p. Art. No. 4762, 2003.

[117] Menon, S., Del Genio, A. D., Koch, D., and Tselioudis, G., "GCM simulations of the aerosol indirect effect: Sensitivity to cloud parameterization and aerosol burden," *J. Atmos. Sci.*, vol. 59, pp. 692–713, 2002.

[118] Meskhidze, N., Nenes, A., Conant, W. C., and Seinfeld, J. H., "Evaluation of a new cloud droplet activation parameterization with in situ data from CRYSTAL-FACE and CSTRIPE," *J. Geophys. Res.*, vol. 110, p. 10, 2005.

[119] Nenes, A., Charlson, R. J., Facchini, M. C., Kulmala, M., Laaksonen, A., and Seinfeld, J. H., "Can chemical effects on cloud droplet number rival the first indirect effect ?," *Geophys. Res. Lett.*, vol. 29, p. 1848, 2002.

[120] Nenes, A., Conant, W. C., and Seinfeld, J. H., "Black carbon radiative heating effects on cloud microphysics and implications for the aerosol indirect effect 2. Cloud microphysics," *J. Geophys. Res.*, vol. 107, p. doi:10.1029/2002JD002101, 2002.

[121] Nenes, A., Ghan, S., Abdul-Razzak, H., Chuang, P., and Seinfeld, J., "Kinetic limitations on cloud droplet formation and impact on cloud albedo," *Tellus*, vol. 53, pp. 133–149, 2001.

[122] Nenes, A. and Seinfeld, J. H., "Parameterization of cloud droplet formation in global climate models," *J. Geophys. Res.*, vol. 108, p. doi:10.1029/2002JD002911, 2003.

[123] P., M., "Large-eddy simulation of the convective atmospheric boundary-layer," *J. Atmos. Sci.*, vol. 46, pp. 1492–1516, 1989.

[124] Peng, Y. and Lohmann, U., "Sensitivity study of the spectral dispersion of the cloud droplet size distribution on the indirect aerosol effect," *Geophys. Res. Lett.*, vol. 30, p. doi:10.1029/2003GL017192, 2003.

[125] Peng, Y., Lohmann, U., and Leaitch, R., "Importance of vertical velocity variations in the cloud droplet nucleation process of marine stratus clouds," *J. Geophys. Res.*, vol. 110, p. doi:10.1029/2004JD004922, 2005.

[126] Peng, Y., Lohmann, U., Leaitch, R., and Kulmala, M., "An investigation into the aerosol dispersion effect through the activation process in marine stratus clouds," *J. Geophys. Res.*, vol. 112, p. doi:10.1029/2006JD007401, 2007.

[127] Penner, J. E., Quaas, J., Storelvmo, T., Takemura, T., Boucher, O., Guo, H., Kirkevag, A., Kristjansson, J. E., and Seland, O., "Model intercomparison of indirect aerosol effects," *Atmos. Chem. Phys.*, vol. 6, pp. 3391–3405, 2006.

[128] Petters, M. D. and Kreidenweis, S. M., "A single parameter representation of hygroscopic growth and cloud condensation nucleus activity," *Atmos. Chem. Phys.*, vol. 7, pp. 1961–1971, 2007.

[129] Pinsky, M., Khain, A., and Shapiro, M., "Collisons of small drops in a turbulent flow. Part I: Colliisons effiencies: problem formulation and preliminary results," *J. Atmos. Sci.*, vol. 56, pp. 2585–2600, 1999.

[130] Pinsky, M. and Khain, A. P., "Formation of inmohogeneity on drop concentration induced by drop inertia and their contribution to the drop spectrum broadening," *Quart. J. Roy. Meteor. Soc.*, vol. 123, pp. 1517–1542, 1997.

[131] Pruppacher, H. R., "A new look at homogeneous ice nucleation in supercooled water drops," *J. Atmos. Sci.*, vol. 52, pp. 1924–1933, 1995.

[132] Pruppacher, H. R. and Klett, J. D., *Microphysics of Clouds and Precipitation*. Norwell, Mass.: Kluwer Acad., 1997.

[133] Radke, L., Jr., J. C., and King, M., "Direct and remote sensing observations of the effects of ship tracks on clouds," vol. 246, pp. 1146–1149, 1989.

[134] Ramanathan, V., Crutzen, P. J., Kiehl, J. T., and Rosenfeld, D., "Atmosphere - aerosols, climate, and the hydrological cycle," *Science*, vol. 294, no. 5549, pp. 2119–2124, 2001.

[135] Randall, D., Khairoutdinov, M., Arakawa, A., and Grabowski, W., "Breaking the cloud parameterization deadlock," *Bull. Am. Met. Soc*, vol. 84, p. 1547, 2003.

[136] Riemer, N. and Wexler, A. S., "Droplets to drops by turbulent coagulation," *J. Atmos. Sci.*, vol. 62, pp. 1962–1975, 2005.

[137] Riemer, N., Wexler, A. S., and Diehl, K., "Droplet growth by gravitational coagulation enhanced by turbulence: Comparison of theory and measurements," *J. Geophys. Res.*, vol. 112, p. 7, 2007.

[138] Rissman, T. A., Nenes, A., and Seinfeld, J. H., "Chemical amplification (or damping) of the Twomey effect: Conditions derived from droplet activation theory," *J. Atmos. Sci.*, vol. 61, pp. 919–930, 2004.

[139] Rogers, R. R. and Yau, M. K., *A Short Course in Cloud Physics*. Burlington, MA: Butterworth-Heinemann, 1989, 290pp.

[140] Rotstayn, L. and Liu, Y., "Sensitivity of the first indirect aerosol effect to an increase of cloud droplet spectral dispersion with droplet number concentration," *J. Climate*, vol. 16, pp. 3476–3481, 2003.

[141] Rotstayn, L. D., "A physically based scheme for the treatment of stratiform clouds and precipitation in large-scale models: I: Description and evaluation of the microphysical processes," *Q. J. R. Meteorol. Soc.*, vol. 123, pp. 1227–1282, 1997.

[142] Rotstayn, L. D. and Liu, Y. G., "A smaller global estimate of the second indirect aerosol effect," *Geophys. Res. Lett.*, vol. 32, p. 4, 2005.

[143] Ruehl, C. R., Nenes, A., and Chuang, P. Y., "How quickly do cloud droplets form on atmospheric particles?," *Atmos. Chem. Phys. Discuss.*, vol. 7, pp. 14233–14264, 2007.

[144] Schlamp, R. J. and et al. *J. Atmos. Sci.*, vol. 33, p. 1747, 1976.

[145] Schlamp, R. J. and et al. *J. Atmos. Sci.*, vol. 36, p. 339, 1979.

[146] Schreier, M., Kokhanovsky, A. A., Eyring, V., Bugliaro, L., Mannstein, H., Mayer, B., Bovensmann, H., and Burrows, J. P., "Impact of ship emissions on the microphysical, optical and radiative properties of marine stratus: a case study," *ACP*, vol. 6, pp. 4925–4942, 2006.

[147] Seifert, A. and Beheng, K. D., "A double-moment parameterization for simulating autoconversion, accretion and selfcollection," *Atmos. Res.*, vol. 59-60, pp. 265–281, 2001.

[148] Seinfeld, J. and Pandis, S., *Atmospheric chemistry and physics: from air pollution to climate change*. New York: John Wiley, 1998.

[149] Shaw, R. A. and Lamb, D., "Experimental determination of the thermal accommodation and condensation coefficients of water," *J. Chem. Phys.*, vol. 111, pp. 10659–10663, 1999.

[150] Shaw, R. A., Reade, W. C., Collins, L. R., and Verlinde, J., "Preferential concentration of cloud drops by turbulence: Effects on the early evolution of cumulus cloud droplet spectra," *J. Atmos. Sci.*, vol. 55, pp. 1965–1976, 1998.

[151] Shulman, M. L., Jacobson, M. C., Charlson, R. J., Synovec, R. E., and Young, T. E., "Dissolution behavior and surface tension effects of organic compounds in nucleating cloud droplets," *Geophys. Res. Lett.*, vol. 23, pp. 277–280, 1996.

[152] Snider, J. R., Guibert, S., Brenguier, J.-L., and Putaud, J.-P., "Aerosol activation in marine stratocumulus clouds: 2. Köhler and parcel theory closure studies," *J. Geophys. Res.*, vol. 108, p. doi:10.1029/2002JD002692, 2003.

[153] Sorooshian, A., Brechtel, F. J., Ma, Y., Weber, R. J., Corless, A., Flagan, R. C., and Seinfeld, J. H., "Modeling and characterization of a particleinto-liquid sampler (PILS)," *Aerosol Sci. Technol.*, vol. 40, pp. 396–409, 2006.

[154] Sotiropoulou, R., Nenes, A., Adams, P. J., and Seinfeld, J. H., "Cloud condensation nuclei prediction error from application of Köhler theory: Importance for the aerosol indirect effect," *J. Geophys. Res.*, vol. 112, no. D12202, p. doi:10.1029/2006JD007834, 2007.

[155] Spiro, P. A., Jacob, D. J., and Logan, J. A., "Global inventory of sulfur emission with $1^0 \times 1^0$ resolution," *J. Geophys. Res.*, vol. 97, pp. 6023–6036, 1992.

[156] Stevens, B., Ackerman, A. S., B. A. Albrecht, A. R. Brown, A. C., Cuxart, J., Duynkerke, P. G., Lewellen, D. C., Macvean, M. K., Negers, R. A. J., Sanchez, E., Siebesma, A. P., and Stevens, D. E., "Simulations of trade wind cumuli under a strong inversion," *J. Atmos. Sci.*, vol. 58, pp. 1870–1891, 2001.

[157] Stevens, B., Bell, J. B., Almgren, A. S., Beckner, V. E., and Rendleman, C. A., "Small-scale processes and entrainment in a stratocumulus marine boundary layer," *J. Atmos. Sci.*, vol. 57, pp. 567–581, 2000.

[158] Stevens, B., Feingold, G., Cotton, W. R., and Walko, R. L., "Elements of the microphysical structure of numerically simulated nonprecipitating stratocumulus," *J. Atmos. Sci.*, vol. 53, pp. 980–1006, 1996.

[159] Sundqvist, H., Berge, E., and Kristjansson, J. E., "Condensation and cloud parameterization studies with a mesoscale numerical weather prediction model," *Mon. Wea. Rev.*, vol. 117, pp. 1641–1657, 1989.

[160] Tao, W.-K., Li, X., Khain, A., Matsui, T., Lang, S., and Simpson, J., "Role of atmospheric aerosol concentration on deep convective precipitation: Cloud-resolving model simulations," *J. Geophys. Res.*, vol. 112, pp. doi:10.1029/2007JD008728, 2007, 2007.

[161] Telford, J. W., "A new aspect of coalescence theory," *J. Meteorol.*, vol. 12, pp. 436–444, 1955.

[162] Teller, A. and Levin, Z., "The effects of aerosols on precipitation and dimensions of subtropical clouds; a sensitivity study using a numerical cloud model," *Atmos. Chem. Phys.*, vol. 6, pp. 67–80, 2006.

[163] Turner, D. D., Vogelmann, A. M., Austin, R. T., Barnard, J. C., Cady-Pereira, K., Chiu, J. C., Clough, S. A., Flynn, C., Khaiyer, M. M., Liljegren, J., Johnson, K., Lin, B., Long, C., Marshak, A., Matrosov, S. Y., Mcfarlane, S. A., M. Miller, Q. Min, P. M., Ohirok, W., Wang, Z., and Wiscombe, W., "Thin liquid water clouds: Their importance and our challenge," *Bull. Am. Met. Soc*, vol. 178, pp. 177–190, 2007.

[164] Twomey, S., "The nuclei of natural cloud formation. II. The supersaturation in natural clouds and the variation of cloud droplet concentration," *Geofisica Pura Appl.*, vol. 43, pp. 243–249, 1959.

[165] Twomey, S. *J. Atmos. Sci.*, vol. 21, p. 553, 1964.

[166] Twomey, S., "The influence of pollution on the shortwave albedo of clouds," *J. Atmos. Sci.*, vol. 34, pp. 1149–1152, 1977.

[167] VanReken, T. M., Rissman, T. A., Roberts, G. C., Varutbangkul, V., Jonsson, H. H., Flagan, R. C., and Seinfeld, J. H., "Toward

aerosol/cloud condensation nuclei (CCN) closure during CRYSTAL-FACE," *J. Geophys. Res.*, vol. 108, no. D20, p. doi:10.1029/2003JD003582, 2003.

[168] Vohl, O., Mitra, S. K., and Pruppacher, H. R., "A wind tunnel investigation of the effects of turbulence on the collision growth of cloud drops," *WMO Intern. Confer. On Clouds and Precipitation.*

[169] Vohl, O., Mitra, S. K., Wurzler, S. C., and Pruppacher, H. R., "A wind tunnel study of the effects of turbulence on the growth of cloud drops by collision and coalescence," *J. Atmos. Sci.*, vol. 56, pp. 4088–4099, 2000.

[170] Wang, L. P., Ayala, O., Xue, Y., and Grabowski, W. W., "Comments on "Droplets to drops by turbulent coagulation"," *J. Atmos. Sci.*, vol. 63, pp. 2397–2401, 2006.

[171] Wendisch, M., Keil, A., and Korolev, A. V., "FSSP characterization with monodisperse water droplets," *J. Atmos. Ocean. Tech.*, vol. 13, pp. 1152–1165, 1996.

[172] Wood, R., "Drizzle in stratiform boundary layer clouds. Part II: Microphysical aspects," *J. Atmos. Sci.*, vol. 62, pp. 3034–3050, 2005.

[173] Wood, R. and Blossey, P. N., "Comments on "Parameterization of the autoconversion process. Part I: Analytical formulation of the Kessler-type parameterizations"," *J. Atmos. Sci.*, vol. 62, pp. 3003–3006, 2005.

[174] Wood, R., Irons, S., and Jonas, P. R., "How important is the spectral ripening effect in stratiform boundary layer clouds? Studes using simple trajectory analysis," *J. Atmos. Sci.*, vol. 59, pp. 2681–2693, 2002.

[175] Wyang, M. C., Bretherton, C. S., Rand, H. A., and Stevens, D. E., "Numerical simulations and a conceptual model of the stratocumulus to trade cumulus trasition," *J. Atmos. Sci.*, vol. 54, pp. 168–192, 1997.

[176] Xie, P. and Arkin, P. A., "Global precipitation: A 17-year monthly analysis based on gauge observations, satellite estimates, and numerical model outputs," *Bull. Amer. Meteor. Soc.*, vol. 78, pp. 2539–2558, 1997.

[177] Xue, Y., Wang, L.-P., and Grabowski, W. W., "Growth of cloud droplets by turbulent collisioncoalescence," *J. Atmos. Sci.*, vol. 65, pp. 331–356, 2008.

[178] Yin, Y., Levin, Z., Reisin, T., and Tzivion, S., "The effect of giant cloud condensational nuclei on the development of precipitation in convective clouds: a numerical study.," *Atmos. Res.*, vol. 53, pp. 91–116, 2000.

[179] Yum, S. S. and Hudson, J. G., "Adiabatic predictions and observations of cloud droplet spectral broadness," *Atmos. Res.*, vol. 73, pp. 203–223, 2005.

[180] Zhou, Y., Wexler, A. S., and Wang, L.-P., "Modelling turbulent collision of bidisperse inertial particles," *J. Fluid Mech.*, vol. 433, pp. 77–104, 2001.